2021

Absolute Number Density Measurements of Atomic Species in Air and Nitrogen Plasmas

Jeffrey C. Schindler
University of Vermont

Absolute Number Density Measurements of Atomic Species in Air and Nitrogen Plasmas

A Thesis Presented

by

Jeffrey Schindler

to

The Faculty of the Graduate College

of

The University of Vermont

In Partial Fulfillment of the Requirements
for the Degree of Master of Science
Specializing in Mechanical Engineering

October, 2021

Defense Date: September 3^{rd}, 2021
Thesis Examination Committee:

Douglas Fletcher, Ph.D., Advisor
Tian Xia, Ph.D., Chairperson
Yves Dubief, Ph.D.
Jason Meyers, Ph.D.
Cynthia J. Forehand, Ph.D., Dean of the Graduate College

Abstract

A vehicle reentering Earth's atmosphere at hypersonic velocities violently compresses the air in front of it, creating a shell of plasma at the surface. This plasma imparts energy onto the vehicle's surface via convective, radiative, and chemical heating. Currently, large uncertainties in measurements of surface reaction rates lead to over-designed thermal protection systems. Improvements in the precision of these measurements could substantially decrease the weight of the heat shield, freeing up space for additional fuel or human/scientific payload. This work aims to improve current methods for measurements of atomic number densities in plasmas, so that they may be applied to future measurements of surface reaction rates.

In this work, relative number densities are measured by probing atomic species in an inductively coupled plasma with two-photon absorption laser induced fluorescence. The use of a room temperature flow reactor as a reference source allows for absolute calibration of relative number density measurements while removing many constants, and their uncertainties, from the calculation. Temperature and number density measurements in the free stream of air and nitrogen plasmas suggest near equilibrium populations of both oxygen and nitrogen atoms.

Improvements in methods for fluorescence lifetime measurements, allow for resolution of the lifetimes between 1.5 and 4 ns which are seen in the plasma. Evidence of collision-induced upper state transfer in the plasma is presented. Off line center excitation of N, O, and NO show evidence of higher quenching than is seen at the line-center. Further work is needed to determine if this is a physical phenomenon, or instrumental error.

Acknowledgements

Thank you to Doug Fletcher for your guidance in the lab, and for teaching me to always look at my results with a critical eye.

Thank you to Jason Meyers for introducing me both to the lab, and to spectroscopy in general. For your help and guidance with experiments, and for your friendship over the past few years.

Thank you to Brandon Voll for lending your time and perspective, it has been an enormous help in all my experiments. Its been a pleasure.

Thank you to Roland Herrmann-Stanzel, and Precious Jagun, for teaching me how to run the lab.

Thank you everyone else in the lab for your help with experiments. And to those of you still completing your work, I wish you quick torch start ups, stable laser energy, and long lasting quartz tubes.

Lastly I would like to thank my family and Cynthia for all your support during my time here. Main support for this effort was funded by the following:

"Combined Computational and Experimental Study of UHTCs for Thermal Protection of Hypersonic Vehicles." Office of Naval Research, Award #: N00014-18-1-2531, Dr. Eric Marineau Technical Monitor and Dr. Eric Wichita, Technical Monitor

"Critical Gas Surface Interaction Problems for Atmospheric Entry", NASA ESPCoR, Award #: 80NSSC18M0031, Michael Wright and Scott Splinter, Technical Monitors

Additional hardware and material support was supplied by:

"SiC Fabric Catalysis Assessment in an Inductively Coupled Plasma Facility," NASA Langley Unsolicited, Award #: 80NSSC20K1835, Neil Cheatwood, Technical Monitor

Table of Contents

List of Figures

List of Tables

Chapter 1

Introduction

1.1 Motivation

Spacecraft returning to Earth from Mars and beyond will likely experience re-entry velocities of 13 km/s or greater [7]. In these conditions, the air in front of the reentry craft is violently compressed forming a detached bow shock (Figure 1.1). The thermal energy that is released during the compression of the atmosphere is enough to partially dissociate and ionize the molecular oxygen and nitrogen present in the air, forming a glowing plasma. The job of the thermal protection system (TPS) is to slow the flow of heat to the craft from the reactive plasma which impinges on its surface.

Figure 1.2 shows the mass fraction of past thermal protection systems. Typically, The thickness of a TPS is chosen based on the integrated heat load it will face during reentry. However, these heat loads have large uncertainties, so heat shields must be designed for the worst case scenario. This leads to heat shields that are heavier than they need to be. Depending on their trajectory, many of these craft devote between 10 and 20% of their mass to the TPS, [2] so reducing the uncertainty in these heating

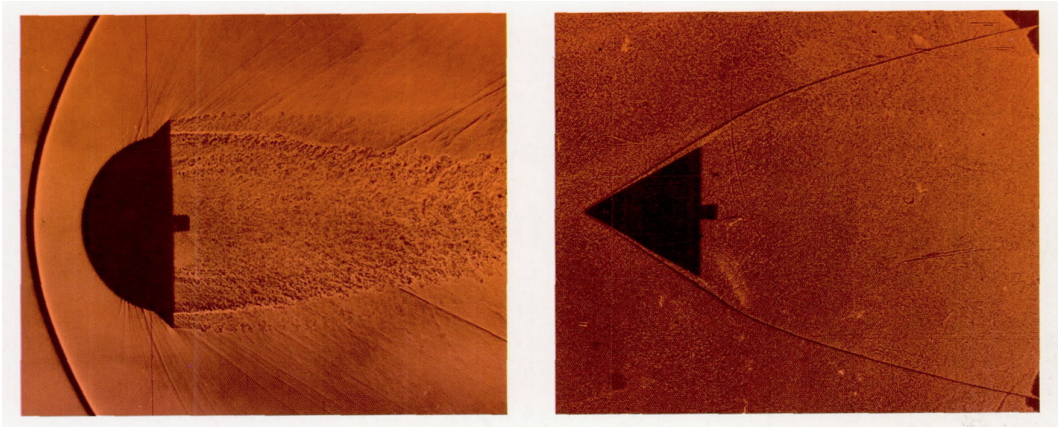

Figure 1.1: The blunt body pushes the shock wave further from the leading edge, reducing the heat transferred to the vehicle. [1]

rates could significantly reduce the mass of the TPS, freeing up some much needed space for more fuel or cargo.

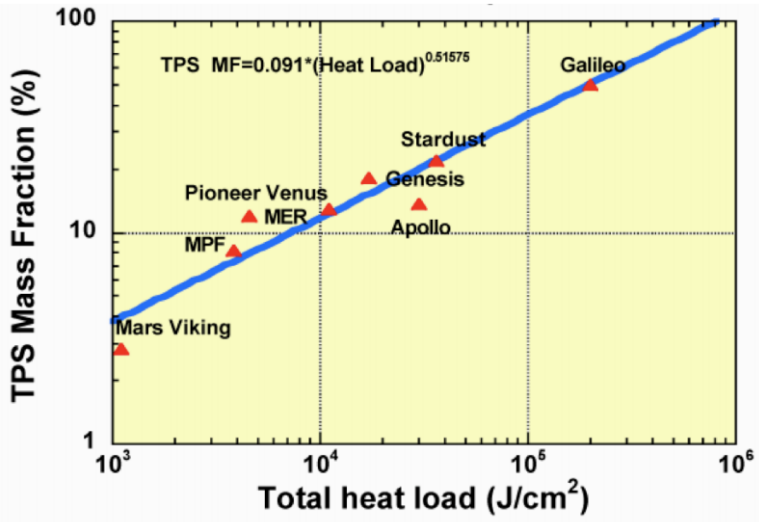

Figure 1.2: TPS Mass fraction of some past NASA missions [2]

During re-entry, heat flows into the craft primarily via 3 modes:

1. Thermal radiation from the shock layer

2. Convection of hot air over the surface

3. Chemical heating from surface reactions and recombination

Radiation and convection heating rates are generally well understood, however, heating rates from surface chemical reactions have larger uncertainties.

1.2 Surface Reaction Rates

Ablative cooling methods are commonly used in thermal protection systems for atmospheric reentry. These generally consist of a porous carbon structure which is filled with a phenolic resin. When heated, the resin vaporizes and pushes back against the impinging flow, creating a buffer zone between the plasma and the heat shield. As many current heat shield materials use carbon as a base, it is prudent to study the chemical reactions which a carbon surface may encounter during re-entry. In a nitrogen plasma, a carbon surface sees two main chemical reactions. These are surface-catalyzed nitrogen recombination (Equation 1.1) and carbon nitridation (Equation 1.2)

$$\mathrm{N} + \mathrm{N} + [\mathrm{s}] \longrightarrow \mathrm{N_2} + 9.8\,\mathrm{eV} \tag{1.1}$$

$$\mathrm{N} + \mathrm{C(s)} \longrightarrow \mathrm{CN} + 0.36\,\mathrm{eV} \tag{1.2}$$

In order to account for the heat generated by these reactions in the design and modeling of a TPS, it is necessary to know how often they occur. For this, the reaction efficiency (γ) is defined as the probability that the reaction will occur given the necessary reactants. In the case of carbon nitridation, the reaction efficiency is

defined as,

$$\gamma_{CN} = \frac{\Gamma_{CN}}{\Gamma_N} \tag{1.3}$$

Where Γ_{CN} represents the flux of CN leaving the surface, and Γ_N represents the flux of nitrogen atoms hitting the surface. Measurements of reaction efficiency are typically collected by monitoring the number density gradient of the various species at the surface. This method is explained further in Section 3.7.

Figure 1.3 shows that previous experimental values of nitridation efficiency for graphite samples span 3 orders of magnitude. There is still significant work to be done before a repeatable result can be reached.

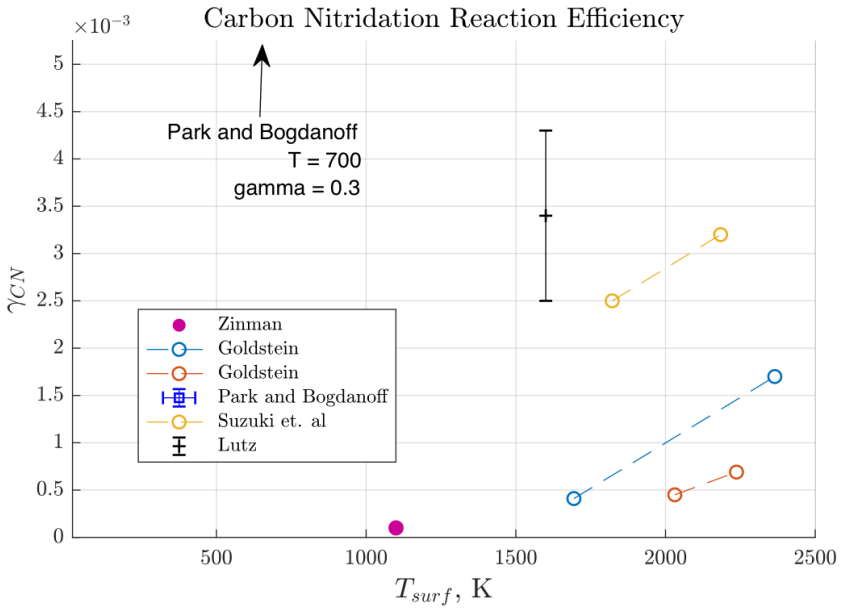

Figure 1.3: Reported values of carbon nitridation efficiency on graphite surfaces.

In 2006, when the Stardust capsule re-entered the Earth's atmosphere. The heat shield survived re-entry and allowed for a chance to compare chemical heating models to surface recession data from a true atmospheric reentry [8]. A model of nitrogen

recombination at a higher than accepted rate was able to simulate the measured TPS recession [9]. Previous experiments at SRI [10] had not found any evidence of nitrogen atoms recombining at the surface of a graphite sample between 1070-1370 K. Later, work by Lutz [11] on graphite samples at 1600 K did show signs of appreciable N-atom recombination. Suggesting that there may be some surface temperature below which nitrogen recombination is negligible.

So far, measurements of surface reaction and recombination rates in ground test facilities have led to inconsistent results, suggesting that improved methods are needed quantify these rates and how they are affected by changes in species temperature, and density. This thesis aims to improve current methods for probing the absolute number density of atomic species in the boundary layer. This in turn should allow for more accurate measurements of reaction efficiencies, as well as provide validation for numerical modelling of the UVM ICP facility.

Chapter 2

ICP Facility

2.1 Inductively Coupled Plasma Torch

UVM's inductively coupled plasma (ICP) torch is designed to emulate the subsonic conditions behind the shockwave of a hypersonic reentry craft for the purpose of studying gas-surface interactions (Figure 2.1). Often, arc-heated facilities are used to study high enthalpy flows, however copper contamination from the electrodes used to energize the flow alters the gas chemistry, adding uncertainty to measured reaction rates. In contrast to arc-heated facilities, the ICP torch provides contaminate free flow which can be sustained for longer test times and at a lower cost. Standard operating conditions for the ICP facility are shown in Table 2.1.

Table 2.1: UVM ICP Torch Operating Conditions

Species of Interest	Standard Condition
Gas [-]	Ar,Air,N_2,O_2,CO_2
Pressure [torr]	100-600
Temperature [K]	4000-7500

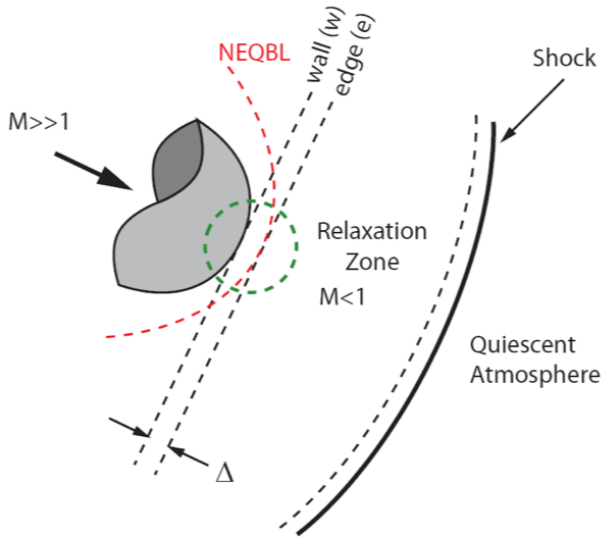

Figure 2.1: Diagram of hypersonic reentry. The green circle represents conditions simulated in UVM's ICP (image: Jason Meyers)

Table 2.2: Equivalent Reentry Altitude and Velocity for ICP Torch

Post Shock Total Pressure [torr]	100	100	600	600
Post Shock Static Temperature [K]	4000	7000	4000	7000
Post Shock Enthalpy [MJ/kg]	8.13	35.5	7.54	27.2
Altitude [km]	50	62	36	45
Mach no. [-]	12	27	12	22
Velocity [km/s]	4.0	8.4	3.8	7.3

Conditions in the ICP can be correlated to a flight condition by equating the static pressure in the ICP to the post shock total pressure, and the translational temperature in the ICP to the post shock static temperature. Table 2.2 shows the subset of flight conditions that the UVM ICP facility can emulate for an air plasma. The post shock enthalpy is calculated assuming chemical equilibrium via "Chemical Equilibrium with Applications" (CEA) [6]

As seen in Figure 2.2, Gas flows at a specified rate into a quartz tube where it is excited via electromagnetic radiation from the load coil. A Lepel Model T-30-3-

MC5-TLI-RF power supply provides single phase 2.5-5 MHz AC to the load coil at up to 30 kW. A brass insert inside the 36 mm ID quartz tube creates an annular flow which recirculates in the induction region. This recirculating plasma ball provides increased coupling between the load coil and the gas, and reaches temperatures on the order of 10,000 K.

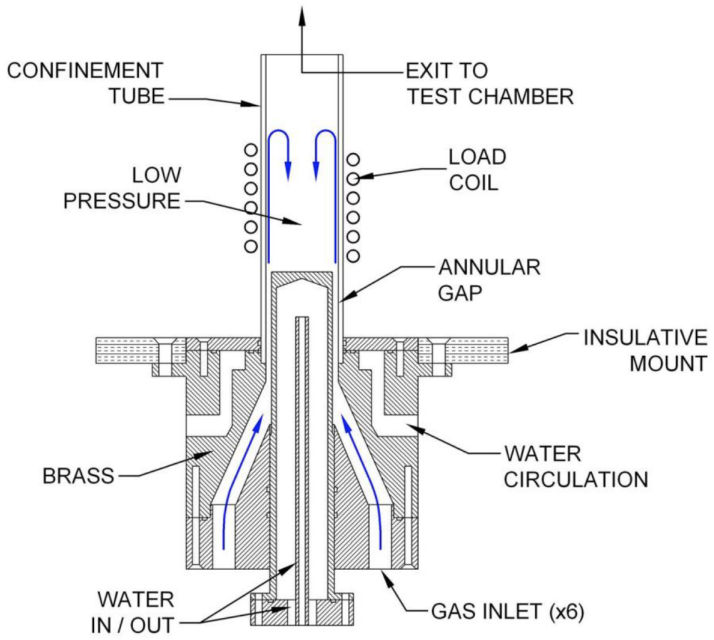

Figure 2.2: Diagram of ICP torch induction zone. (image: [3])

Once excited, the plasma flows out of the induction zone and enters the vacuum chamber as a free jet. Test samples and diagnostic equipment are generally used 90 mm above the jet orifice. Past the test section, heat exchangers remove energy from the flow so that it may be safely exhausted through a vacuum pump. A diagram of the ICP facility is provided in Figure 2.3, for more information on the ICP facility see [3, 12].

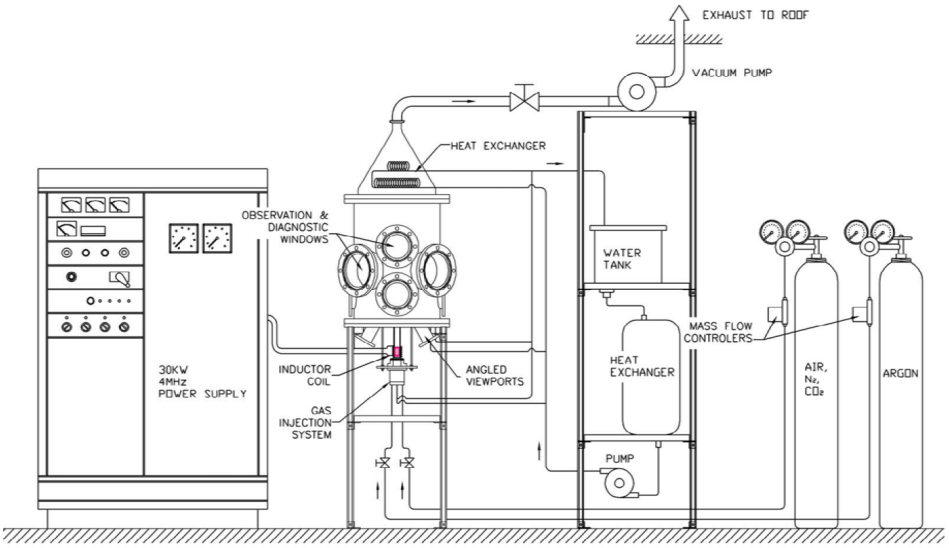

Figure 2.3: Schematic of the UVM Inductively Coupled Plasma Torch. (image: [3])

2.2 Microwave Discharge Flow Reactor

The microwave discharge flow reactor (MDFR or FR) serves multiple purposes in the lab. Its primary role is to provide laser line-width measurements, which are needed for temperature measurements in the ICP. The FR is also used as a calibration source for absolute number density measurements as is outlined in Section 3.4.2. More practically, the FR can be used prior to the experiment to tune the dye laser to the appropriate transition wavelength before the ICP torch is started.

2.2.1 Working Principles

N_2 gas flows into the FR at the inlet (**1**) seen in Figure 2.4. Microwave radiation is fed into the resonant cavity (**2**), where it partially dissociates the N_2 into a non-equilibrium mixture of atomic nitrogen and N_2 in both ground and excited states. As the flow travels towards the measurement location (**4**), the excited species decay, leaving a mixture of mainly ground state N and N_2. If atomic oxygen is desired, nitric oxide is injected into the flow through the mixing ball (**3**) where it reacts with atomic nitrogen to produce oxygen atoms. Regardless, the flow then enters the measurement area (**4**). Fused silica (FS) flats provide a window for the photo-multiplier tube (PMT), and laser light enters and exits the test section through the FS flats on either side (**5**). These flats are positioned at the Brewster angle to maximize the laser energy that enters the flow reactor. The flow then exits the test section, and flows out (**7**) through to the vacuum pump. Pressure measurements are taken downstream of the test section (**6**).

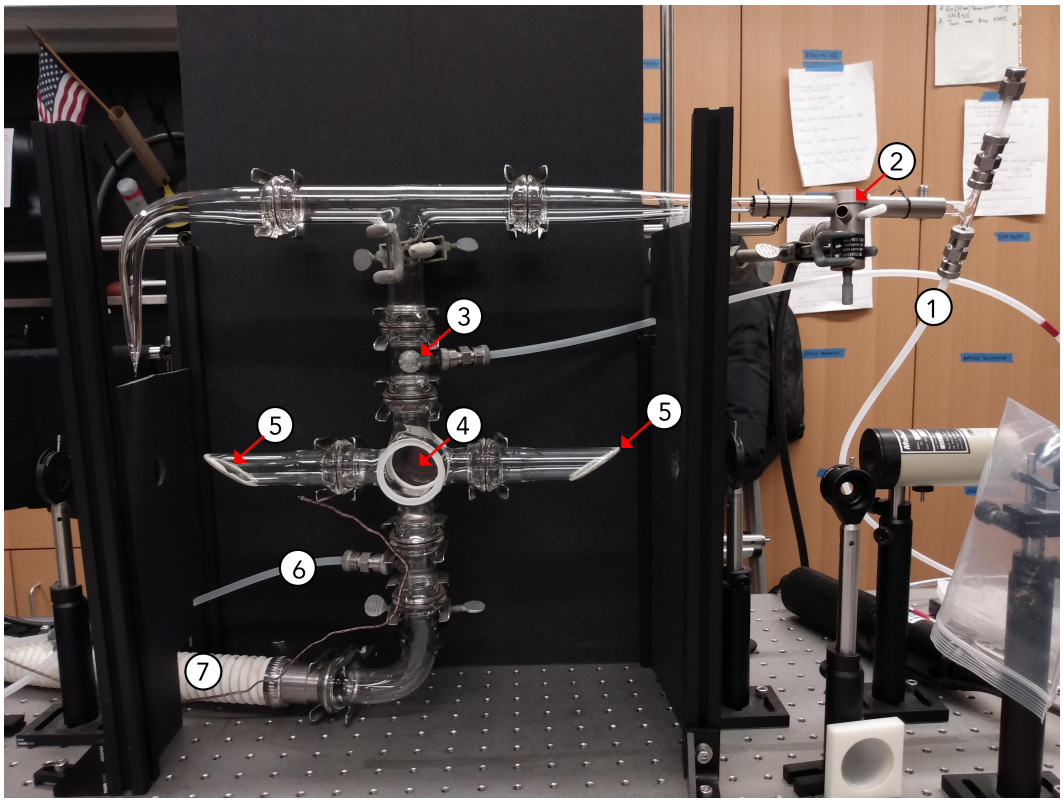

Figure 2.4: Image of the Microwave Discharge Flow Reactor

2.2.2 Flow Reactor Conditions

Table 2.3 gives standard flow reactor conditions. The exact values will vary test to test, but in general stay close to the following.

Table 2.3: MDFR Standard Conditions

Species of Interest	Atomic Nitrogen	Atomic Oxygen
Base Pressure [torr]	0.014	0.014
Working Pressure [torr]	0.25	0.26-0.28
Temperature [°C]	23	23
Microwave Power [W]	50	50
$\dot{V}[N_2]$ [sccm]	50.2	50.2
$\dot{V}$[NO-He] [sccm]	0	1-3

2.3 Laser System

Use of a sum frequency mixing (SFM) scheme to produce 226 nm laser light for probing the O-atom transition allows for quick transitions between measurements of atomic oxygen and nitrogen. Previous frequency tripling methods would require changing out the laser dye. This means temperature and density measurements would take significantly longer and would therefore be harder to compare. Implementation of the SFM scheme allows for measurements of atomic O and N in the same test. Due to its higher spectral resolution, SFM also allows for resolution of the hyperfine structure of the oxygen 226 nm transition.

2.3.1 Generation of 207 and 211 nm Laser Light for Probing Atomic Nitrogen

The 532 nm doubled output of a pulsed nanosecond Nd:YAG laser is used to pump a DCM dye laser. The dye laser outputs laser light at 621/633 nm and is then frequency tripled through a series of BBO crystals to the desired wavelengths at 207/211 nm. Unwanted harmonics are filtered out in a prism based separator, and the beam is then split for delivery to both the ICP torch and the flow reactor.

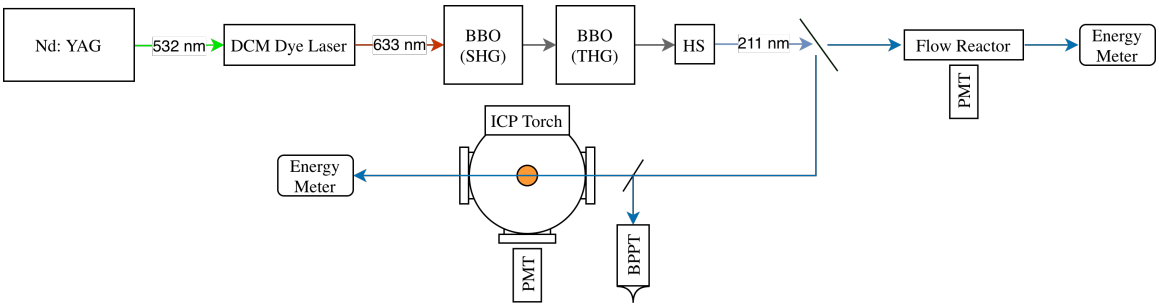

Figure 2.5: Generation of 207 and 211 nm laser light.

2.3.2 Generation of 226 nm Laser Light for Probing Atomic Oxygen

The frequency doubled 532 nm output of an Nd:YAG laser is used to pump a DCM dye laser. The dye laser is tuned to output a 620 nm beam. This beam is then combined with the tripled output of the YAG laser (355 nm) in a non-linear BBO crystal for sum frequency mixing (SFM). Care is taken to align the beams both spatially and temporally for optimal mixing. Through SFM a 226 nm beam is created, and the undesired wavelengths are then separated in a prism based separator. The 226 nm beam is then split for delivery to both the ICP torch and the flow reactor.

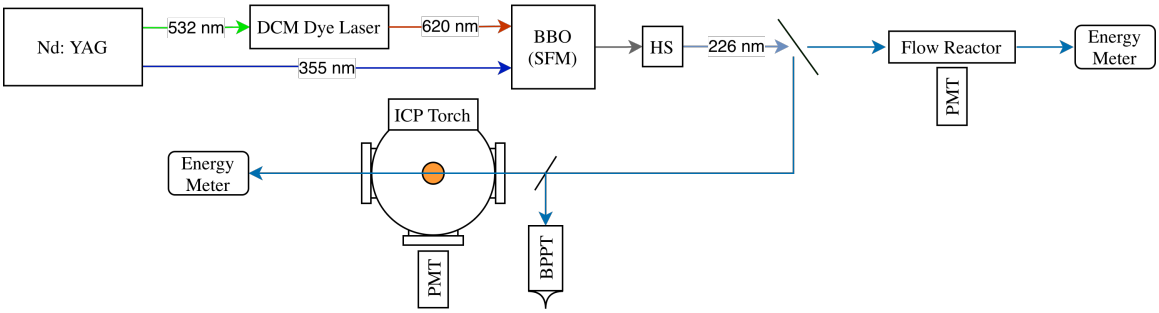

Figure 2.6: Generation of 226 nm laser light.

2.4 Photo-multiplier Tubes

Photo-Multiplier Tubes (PMTs) excel at detecting small amounts of light, even down to a single photon. As shown in Figure 2.7, each photon that collides with the photocathode creates a growing cascade of electrons which eventually reach the anode. Essentially, a PMT is a constant current source with its output controlled by the intensity of light incident on the photocathode.

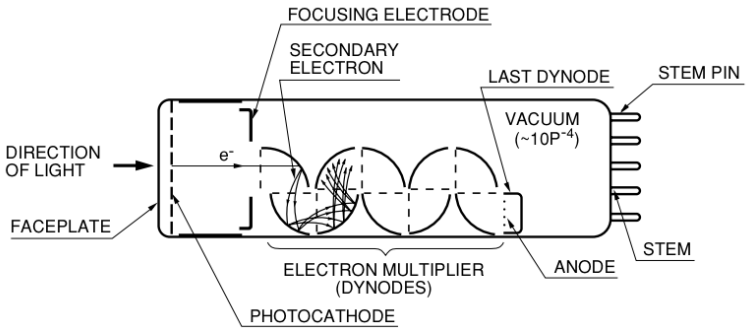

Figure 2.7: General structure of a PMT [4]

In this study, particularly in the measurement of quenched fluorescence lifetimes, a PMTs time response is important. Table 2.4 shows the relevant parameters of the optical collection devices used in this study.

Table 2.4: Instrument Response of Relevant Devices [4]

Device	Model	Spectral Range [nm]	Rise Time [ps]	Transit Time [ps]
Head-on PMT	R9880U-20	230 - 920	570	2700
Side-on PMT	R636-10	185 - 930	2000	20000
Bi-Planar Phototube	R1193u-02	185 - 650	270	n/a

The R9880 PMT is has superior time characteristics to the R636 PMT, and as such it is necessary for measurements of lifetimes on the order of 1-6 ns. However it also

comes with some significant drawbacks. The R636 is a gated PMT, this means that the voltage supplied to the photocathode is turned on just before the laser pulse, and it is turned off shortly after the fluorescence pulse has gone to zero. This prevents saturation of the photocathode and allows for more accurate measurements of the continuous background emission which is often present in LIF measurements. The R9880 on the other hand is not gated, and because of this it is almost impossible to tell during a test whether or not there is a continuous background signal.

In addition, the quantum efficiency of the R9880 drops off at a slightly lower wavelength than the R636, which results in significantly lower signal when using the 211 nm transition of atomic nitrogen.

Chapter 3

Laser Induced Fluorescence

Laser induced fluorescence (LIF) is advantageous to emission or absorption spectroscopic techniques for a number of reasons. Firstly, unlike emission/absorption spectroscopy, the measurement is essentially pointwise. As seen in Figure 3.1, the measurement is confined to the intersection of the laser beam with the solid angle of the PMT. This means the data does not need to be Abel inverted, which removes any error from assuming the jet is axi-symmetric. Secondly, LIF allows for direct probing of ground state atoms and molecules, which, in near-equilibrium mixtures, are the most populated states.

Atomic species seen in plasmas generally have large energy spacings between electronic levels. Probing these transitions with LIF would require lasers which operate deep in the ultraviolet region near 100 nm. One issue with this is that these lasers currently do not exist. To get around this, the atom is excited to the upper state by 2 photons, each with half of the total energy of the transition. This process is aptly named two photon absorption laser induced fluorescence (TALIF).

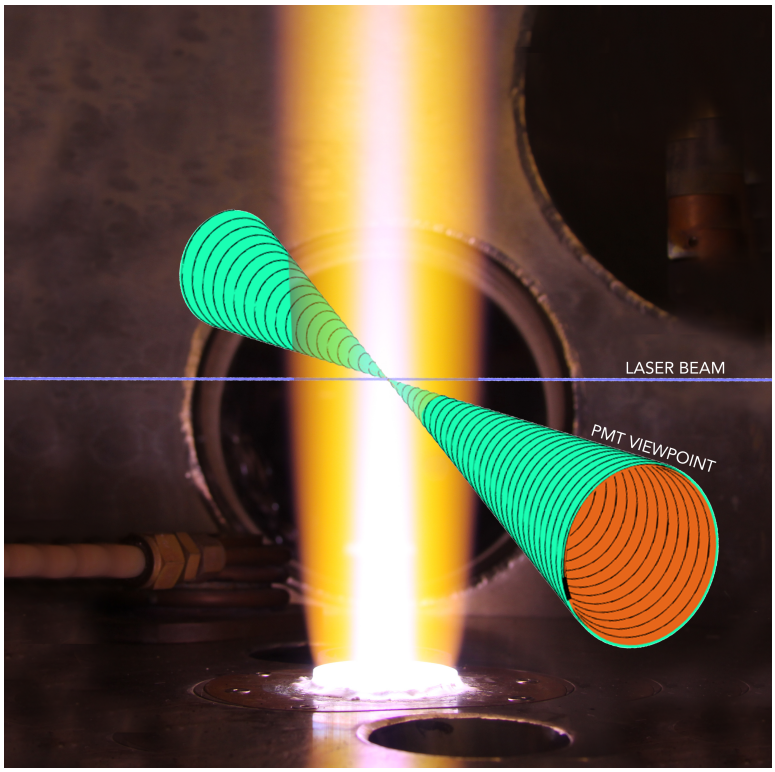

Figure 3.1: Diagram of spatially resolved LIF measurement.

3.1 Working Principles of TALIF

A diagram of the TALIF transitions used in this work is shown in Figure 3.2. The ground state atom is excited to the upper state by two photons from the laser. Once there, it either decays with the emission of a fluorescence photon to the third state, or collides with another particle which de-excites it without the emission of a photon (collisional quenching). If the fluence of the laser is too high, there will be a significant fraction of excited species which will be ionized by the absorption of further photons. This represents a third path for depopulation of the excited state.

Assuming the ground state does not become depleted, This leaves a series of rate

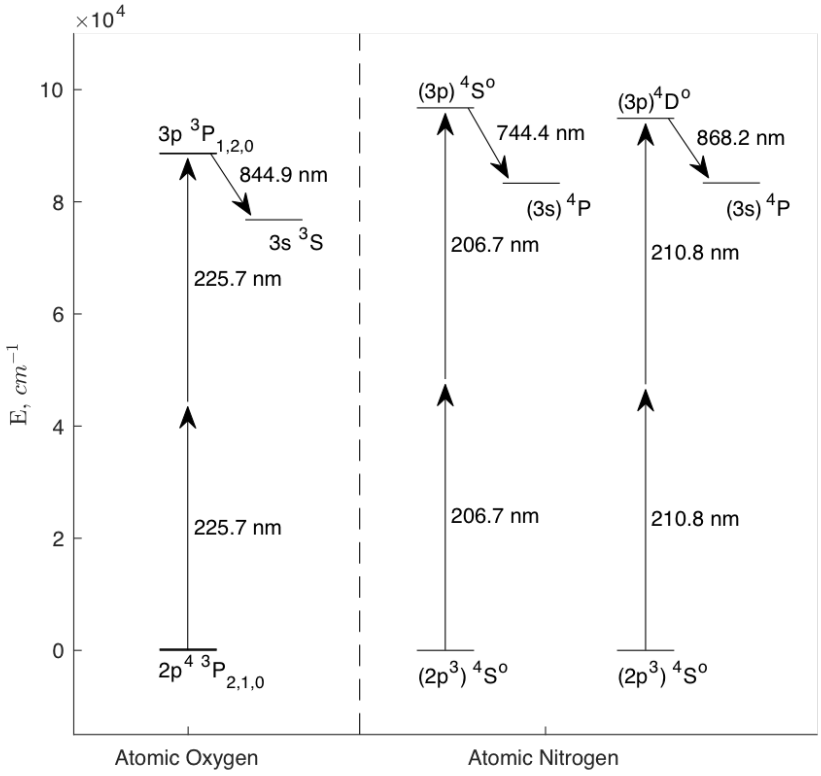

Figure 3.2: TALIF transitions used in this study.

equations as follows [13]. Subscripts 0, 2 and + refer to the ground, excited and ionized energy states respectively.

$$\frac{d\mathbf{N_0}(r,z,t)}{dt} = -\hat{\sigma}^{(2)}\Phi^2(r,z,t)\mathbf{N_0}(r,z,t) \tag{3.1}$$

$$\frac{d\mathbf{N_2}(r,z,t)}{dt} = \hat{\sigma}^{(2)}\Phi^2(r,z,t)\mathbf{N_0}(r,z,t) - (A+Q)\mathbf{N_2}(r,z,t) - \sigma_{pi}\Phi^a(r,z,t)\mathbf{N_2}(r,z,t) \tag{3.2}$$

$$\frac{d\mathbf{N}_+(r,z,t)}{dt} = \sigma_{pi}\Phi^a(r,z,t)\mathbf{N_2}(r,z,t) \tag{3.3}$$

Where a is the number of additional photons needed to ionize the excited atom.

Table 3.1: Symbols relevant to TALIF signal derivation

Symbol	Meaning
A_p	Laser beam cross-sectional area
C_a	Pre-amp capacitance
f_0	population fraction of the ground state.
$F(t)$	Laser pulse temporal profile
G_a	Pre-amp gain
G_p	Photomultiplier gain
$G^{(2)}$	Second order correlation function
$h\nu$	Photon energy
L	Effective length of light collection system
n_i	Absolute number density of species "i"
N_i	n_i per unit volume, per unit time
q_e	Electron charge
η_t	Transmission of filters/windows
η_ϕ	Photocathode quantum efficiency
σ_p	Temporal width of the laser pulse
σ_{pi}	Excited state photoionization cross-section
$\sigma_{12}^{(2)}$	2 photon transition cross-section
$\hat{\sigma}^{(2)}$	$\sigma_{12}^{(2)} G^{(2)}$
$\tau_r = 1/\mathrm{A}$	Radiative or natural lifetime
$\tau_{obs} = 1/(\mathrm{A}+\mathrm{Q})$	Observed lifetime
$\phi(\nu)$	lineshape function
Φ	Laser beam photon flux
Ω_0	Solid angle of collection lens
$\int \frac{S_{LIF}}{E_p^2}(\omega)d\omega$	Integrated, pulse energy normalized, LIF signal

Solving the above rate equations provides an equation for the TALIF signal from an arbitrary laser pulse $F(t)$ (Equation 3.4).

$$S(\nu) = \frac{\Omega}{4\pi} f_0(T)\phi(\nu)\eta_t q_e \eta_\phi G_p \frac{G_a}{C}\frac{L}{A_p}\frac{\hat{\sigma}^{(2)} N_0 E^2}{(h\nu)^2}\frac{A}{(A+Q)}\int_{-\infty}^{\infty} F^2(t)dt \tag{3.4}$$

Solving the rate equations with the assumption that the laser pulse is temporally Gaussian gives the following equation.

$$S(\nu) = \frac{\Omega}{4\pi} f_0(T)\phi(\nu)(\eta_t q_e \eta_\phi G_p \frac{G_a}{C})\frac{A\hat{\sigma}^{(2)} N_0 L E^2}{4\pi^{1/2}\sigma_p A_p (h\nu)^2}\exp\left[\frac{\sigma_p^2 (A+Q)^2}{4}\right]... \\ \int_{-\infty}^{\infty} e^{-(A+Q)t'}\left(1 + erf\left[\frac{t'}{\sigma_p} - \frac{(A+Q)\sigma_p}{2}\right]\right)dt' \tag{3.5}$$

The derivation of these equations can be found in Appendix A.

3.2 Temperature Measurements from TALIF

Temperatures can be measured from TALIF data by analyzing the spectral width of a transition (Figure 3.3). There are 2 main contributors to the width of the transition in the ICP torch. These are the linewidth of the laser, and Doppler broadening based on the temperature. Both of these broadening mechanisms are Gaussian in nature, so it is not necessary to use a Voigt fit.

As the laser beam passes through the gas, photons are blue or red shifted due to

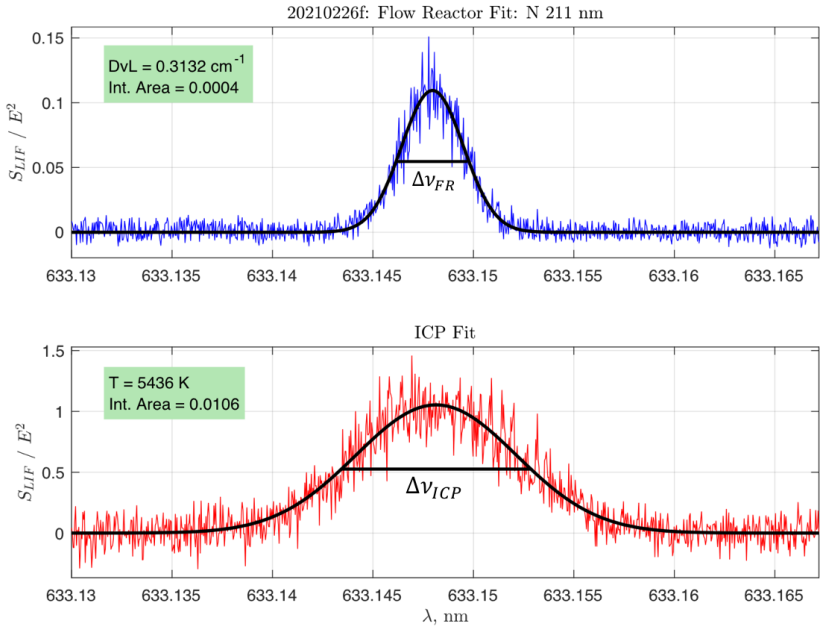

Figure 3.3: Total widths (FWHM) measured in the ICP and FR.

the thermal motion of the atoms. This broadening mechanism is Gaussian because the velocity distribution of the particles follows a Gaussian distribution. As the temperature rises, velocity distribution of the particles gets wider, spreading out the peak of the transition. This spreading of the peak caused by thermal motion is named Doppler broadening.

If the laser were truly a single frequency the Doppler width could simply be measured in a single scan. This, however, is not the case. The laser linewidth is the term used to describe the width of the laser pulse in frequency space. This can be measured by scanning across a transition at a known temperature, and subtracting out the calculated Doppler width ($\Delta\nu_{Doppler,FR}$).

$$\Delta\nu^2_{laser} = \frac{\Delta\nu^2_{Total,FR} - \Delta\nu^2_{Doppler,FR}}{\alpha} \tag{3.6}$$

Where α is the number of photons used to excite the atom to the upper state i.e. 2 for TALIF. This can then be subtracted from the total width measured in the ICP ($\Delta\nu_{Total,ICP}$).

$$\Delta\nu^2_{Doppler,ICP} = \Delta\nu^2_{Total,ICP} - \alpha\Delta\nu^2_{Laser} \tag{3.7}$$

The Doppler width of a transition is given as follows.

$$\Delta\nu_{Doppler} = 2\sqrt{\ln 2}\nu_0\frac{v_p}{c} \tag{3.8}$$

where ν_0 is the central wavenumber, v_p is the most probable molecular speed, and c is the speed of light. Substituting the definition of the most probable molecular speed gives.

$$\Delta\nu_{Doppler} = \frac{\nu_0}{c}\sqrt{\frac{8kT\ln 2}{m}} \tag{3.9}$$

Substituting the molar mass for the molecular weight gives.

$$\Delta\nu_{Doppler} = \sqrt{\frac{8kN_A\ln 2}{c^2}}\nu_0\sqrt{\frac{T}{M}} = 7.162(10)^{-7}\nu_0\sqrt{\frac{T}{M}} \tag{3.10}$$

Note that Equation 3.10 assumes frequency units of cm^{-1}. Combining equations 3.7, 3.6, and 3.10 gives a relation for the temperature of the plasma.

$$T = \frac{M}{(\nu_0 * 7.162(10)^{-7})^2}\left[\Delta\nu^2_{Total,ICP} - \alpha(\frac{\Delta\nu^2_{Total,FR} - \Delta\nu^2_{Doppler,FR}}{\alpha})\right] \tag{3.11}$$

3.2.1 Scan Rate Correction Factor

Due to the nature of the dye laser used in this work, A scan rate correction factor (SRCF) must be applied to the data before it is used for temperature or number density calculations. Figure 3.4a shows variation in the calculated laser linewidth for data collected at different dye laser scan rates. A SRCF was determined for each dye laser scan rate by aligning the hyperfine structure of the oxygen atom 226 nm transition with published values of the transition centers. Future work is needed to verify the linearity of the dye laser scan rate. In general, applying this correction results in a decrease of the measured temperature.

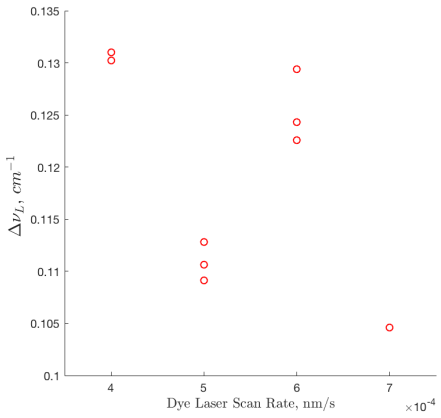

(a) Variation of calculated laser linewidth for different dye laser scan rates.

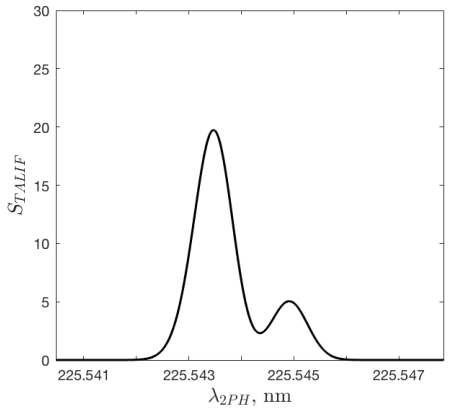

(b) Hyperfine structure of the oxygen 226 nm transition

Figure 3.4

3.3 Absolute Number Density From LIF

Integrating Equation 3.4 in wavenumber (ν) and solving for the ground state number density N_0 gives the following.

$$N_0 = \frac{4\pi C_a}{f_0(T)\Omega_0 q_e \eta_\phi G_a \eta_t L G_p} \frac{A+Q}{A} \frac{A_p}{\int_{-\infty}^{\infty} F_p^2(t)dt} \frac{(h\nu)^2}{G^{(2)}\sigma_{12}^{(2)}} \int \frac{S_{LIF}}{E_p^2}(\omega)d\omega \tag{3.12}$$

While the equation itself is quite simple, performing an experiment to measure each of the constants to a high degree of precision would be a lengthy process. and would potentially still lead to uncertainty values too large to be useful. To reduce the number of measurement needed, a calibration is generally used.

3.4 Calibration Techniques

3.4.1 Standard Methods

Absolute calibration of a TALIF signal can be achieved in a number of ways. In 1986, A paper by Bischel et al. describes a method of TALIF calibration utilizing Raman scattering in molecular hydrogen [14]. Hydrogen Raman cross-sections are well documented, so a measurement of Raman scattered light from a know density of H_2 allows for the extraction of a calibration constant defined by Equation 3.13.

$$D = L\Omega_0 \eta_t \eta_\phi q_e G_p G_a / C \tag{3.13}$$

This calibration constant can then be applied to Equation 3.12 to give the absolute number density of the species probed with TALIF.

In the early 2000's, Niemi et al. published a series of experiments utilizing a method of TALIF calibration via two-photon excitation of noble gases [5, 15]. By finding a TALIF transition of a well documented noble gas spectrally close to the transition of interest, (example shown for atomic oxygen measurements in Figure 3.5) the number density n_X can be calibrated as shown in Equation 3.14.

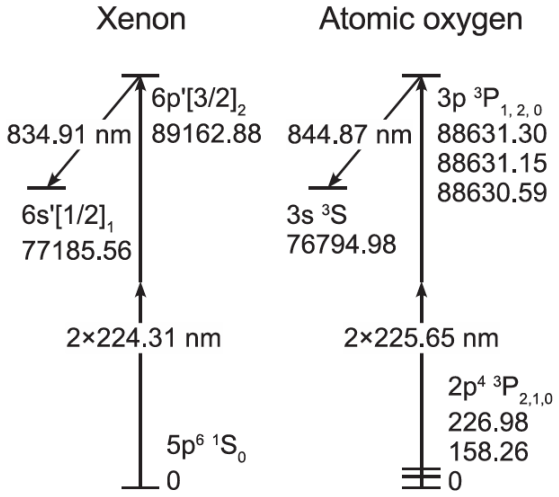

Figure 3.5: Suitable Xenon transition for calibration of atomic Oxygen 225 nm transition [5]

$$n_X = \frac{T_R}{T_X}\frac{\eta_R}{\eta_X}\frac{\sigma_R^{(2)}}{\sigma_X^{(2)}}\frac{a_R}{a_X}\left(\frac{h\nu_X}{h\nu_R}\right)^2\frac{S_X}{S_R}n_R \tag{3.14}$$

Where the subscript X denotes the species of interest and R denotes the reference gas. T represents the transmission of the collection optics, η is the quantum efficiency of the photodetector, a is the fluorescence quantum yield of each transition, and $\sigma^{(2)}$ is the two-photon excitation cross-section [5]. This method requires the assumption

that the excitation and emission wavelengths of the reference gas are sufficiently close to those of the species in question. [16]

3.4.2 Our Method

The full equation for the absolute number density of a species from TALIF is shown again in Equation 3.15.

$$n_{ICP} = \frac{4\pi C_a}{\Omega_0 q_e \eta_\phi G_a f_0(T) \eta_t L G_p} \frac{\tau_{rad}}{\tau_{obs}} \frac{A_p}{\int_{-\infty}^{\infty} F_p^2(t)dt} \frac{(h\nu)^2}{G^{(2)}\sigma_{12}^{(2)}} \int \frac{S_{LIF}}{E_p^2}(\omega)d\omega \tag{3.15}$$

By taking the ratio of the relative number densities in the ICP and FR (Equation 3.16), the constants in red can be removed from this equation. Multiplying this ratio by the absolute number density measured in the FR results in the absolute number density of the species in the ICP. In experiment, this is done by taking measurements at the ICP, then physically moving the PMT and collection optics to the flow reactor and taking measurements there.

$$n_{ICP} = \frac{n_{ICP}}{n_{FR}} n_{FR} \tag{3.16}$$

$$n_{ICP} = \frac{\left[\frac{A_p}{f_0(T)LG_p\tau_{obs}} \int \frac{S_{LIF}}{E_p^2} d\omega\right]_{ICP}}{\left[\frac{A_p}{f_0(T)LG_p\tau_{obs}} \int \frac{S_{LIF}}{E_p^2} d\omega\right]_{FR}} \quad n_{FR} \tag{3.17}$$

A few constants do remain in Equation 3.17. The beam area (A_p) varies between the collection area of the ICP and FR, so it can not be cancelled out. G_p and L vary because a higher gain, and/or larger aperture may be needed at the FR to achieve

Table 3.2: Parameters Involved in Absolute Number Density Measurements.

Symbol	Description
n	Absolute number density
L	Effective length of light collection system
Ω_0	Solid angle of collection lens
η_t	Transmission of filters/windows
q_e	Electron charge
η_ϕ	Photocathode quantum efficiency
G_p	Photomultiplier gain
G_a	Pre-amp gain
C_a	Pre-amp capacitance
τ_{rad}	Radiative lifetime
τ_{obs}	Observed lifetime
A_p	Laser beam cross-sectional area
$h\nu$	Photon energy
$F(t)$	Laser pulse temporal profile
$f_0(T)$	Ground state population fraction
$G^{(2)}$	second order correlation function
$\sigma_{12}^{(2)}$	2 photon transition cross-section
$\int \frac{S_{LIF}}{E_p^2}(\omega)d\omega$	Integrated, pulse energy normalized, LIF signal

good signal due to differences in the number density of the FR and ICP. In this work the PMT aperture was kept constant, and the PMT bias voltage was used to increase the signal intensity because the bias voltage can be set more precisely than the PMT aperture. Finally, n_{FR} is measured through titration.

Due to the nature of the data collection system used, there are a few additional factors which must be applied to the number density calculation. The gated boxcar averaging system, used to measure the TALIF signal, outputs the average signal seen while the gate is on. Because of this, S_{LIF} must be multiplied by the gate-width to return the integrated area. Also, the laser energy measurements must be calibrated by 2 factors. The first factor accounts for the difference in sensitivity of the energy meters at the FR and ICP. the second factor accounts for laser energy which is reflected and absorbed by the window as the beam leaves the ICP and FR.

The PMT window transmission efficiency η_t is left out of Equation 3.17 because measurements of this factor show that, so long as the ICP window is kept clean, the transmission of the ICP window is equal to that of the FR. Losing about 4% of the fluorescence intensity at each face of the window.

3.4.3 Ground State Degeneracy

When calculating the absolute number density of atomic oxygen, it is necessary to account for the degeneracy of the ground electronic state ($f_0(T)$). Changes in temperature alter the equilibrium population of each degenerate state. For the most populated state (J" = 2), the population fraction is given by

$$f_0(T) = \frac{5}{5 + 3e^{-228.75/T} + e^{-326.59/T}} \tag{3.18}$$

For measurements of atomic nitrogen, $f_0(T) = 1$ because the ground state is non-degenerate.

3.5 Fluorescence Polarization

As Discussed by Jeffries et al. [17], At low pressures, the fluorescence of atomic nitrogen excited at 211 nm is polarized. At the conditions of the FR, the fluorescence perpendicular to the laser polarization vector is measured to be 1.26 times greater than the fluorescence parallel to the laser polarization. Because this effect occurs at the FR, and not at the ICP, this must be taken into account in the number density measurement.

We find the equivalent isotropic fluorescence by assuming it is equal to the average polarized fluorescence.

$$I_{equiv} = (I_\perp + I_\parallel)/2 \tag{3.19}$$

$$I_{equiv} = (I_\perp + \frac{I_\perp}{x})/2 \tag{3.20}$$

Where x is is the ratio $I_\perp/I_\parallel$, in this case $x = 1.26$.

$$I_{equiv} = I_\perp \frac{1+x}{2x} \tag{3.21}$$

This results in a net increase in the measured number density at the ICP by ≈12%.

3.6 Beam Area - (A_p)

In the development of the number density from TALIF, the laser pulse was assumed to be spatially Gaussian. While this may be a close approximation in some cases, it is better to use an equivalent Gaussian beam width which would produce the same amount of 2-photon excitation as the true laser pulse. To do this, the laser beam is first assumed to be a Gaussian of the form:

$$G(x,y) = G_0 \exp\left[\frac{-2(x^2+y^2)}{w^2}\right] \tag{3.22}$$

The integral of this distribution is given by:

$$I_1 = \int_{-a}^{a}\int_{-a}^{a} G(x,y)dxdy \tag{3.23}$$

$$= G_0 \int_{-a}^{a} \exp\left[\frac{-2(x^2)}{w^2}\right]dx \int_{-a}^{a} exp\left[\frac{-2(y^2)}{w^2}\right]dy \tag{3.24}$$

$$= 4G_0 \int_{0}^{a} \exp\left[\frac{-2(x^2)}{w^2}\right]dx \int_{0}^{a} exp\left[\frac{-2(y^2)}{w^2}\right]dy \tag{3.25}$$

$$= 2G_0 w^2 \left[\int_0^{a\sqrt{2}/w} \exp(-u^2)du\right]^2 \tag{3.26}$$

$$= \frac{\pi w^2 G_0}{2}\left[erf\left(\frac{\sqrt{2}a}{w}\right)\right]^2 \tag{3.27}$$

Where $2a$ is the length of the sides of a square measurement area, G_0 is the amplitude of the Gaussian, and w is the $1/e^2$ width. The integral of the square of the Gaussian

distribution is given by:

$$I_2 = \int_{-a}^{a}\int_{-a}^{a} G(x,y)^2 dxdy \tag{3.28}$$

$$= G_0^2 \int_{-a}^{a} \exp\left[\frac{-4(x^2)}{w^2}\right]dx \int_{-a}^{a} exp\left[\frac{-4(y^2)}{w^2}\right]dy \tag{3.29}$$

$$= 4G_0^2 \int_{0}^{a} \exp\left[\frac{-4(x^2)}{w^2}\right]dx \int_{0}^{a} exp\left[\frac{-4(y^2)}{w^2}\right]dy \tag{3.30}$$

$$= G_0^2 w^2 \left[\int_0^{2a/w} \exp(-u^2)du\right]^2 \tag{3.31}$$

$$= \frac{\pi w^2 G_0^2}{4}\left[erf\left(\frac{2a}{w}\right)\right]^2 \tag{3.32}$$

Applying I_1 and I_2 to discrete data measured on a Spirocon camera (see Figure 3.6) gives the following approximation.

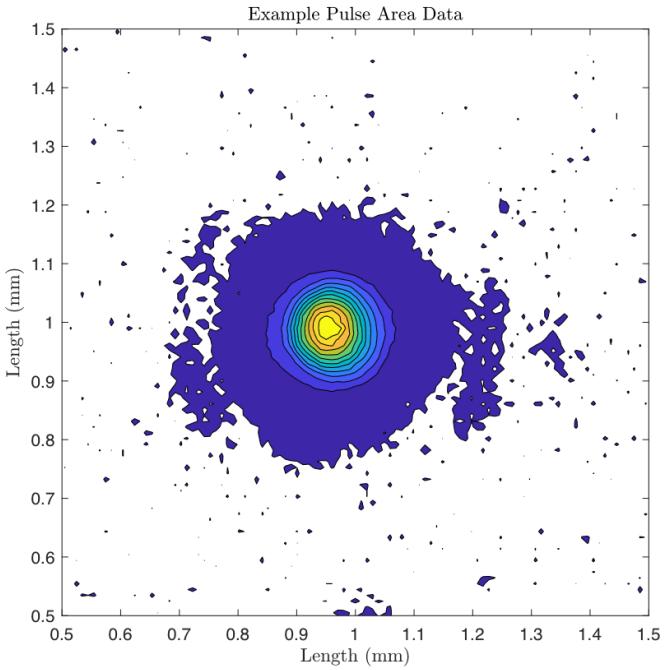

Figure 3.6: Beam profile as captured with Spirocon camera.

$$\tilde{I}_1 = \sum_i \sum_j (F_{ij} - bkg_{ij})(\Delta x \Delta y) \tag{3.33}$$

$$\tilde{I}_2 = \sum_i \sum_j (F_{ij} - bkg_{ij})^2(\Delta x \Delta y) \tag{3.34}$$

Where $(\Delta x \Delta y)$ is the square of the pixel spacing. Using equations 3.27 and 3.32 gives an equation for the beam width w.

$$w = \frac{\tilde{I}_1}{\sqrt{\pi \tilde{I}_2}} \frac{erf(2a/w)}{erf(\sqrt{2}a/w)} \tag{3.35}$$

As long as the detection area is a few times larger than the beam width w, the error function terms are equal to 1 [18].

3.7 Reaction Rates and Efficiencies

3.7.1 Total Reaction Rate and Efficiency

In the boundary layer of a carbon sample, atomic nitrogen is removed by both N_2 recombination and carbon nitridation. From the concentration gradient of atomic nitrogen at the wall, the combined reaction rate can be determined. The approach for calculating the reaction rate is outlined in previous work from our lab [19], and begins with Goulard's expression for the flux of atoms of species i due to diffusion [20].

$$j_{iw} = \rho_w D_{iw} \frac{\partial C_i}{\partial y}\bigg|_w \tag{3.36}$$

Where the subscript w represents the value at the wall (sample surface), D is the diffusion coefficient, ρ is the density, and C_i is the mass fraction of species i. For steady flow this flux is set equal to the flux of the reaction products leaving the surface.

$$k_w C_i \rho_w = \rho_w D_{iw} \frac{\partial C_i}{\partial y}\bigg|_w \tag{3.37}$$

Where k_w is the reaction rate. Due to the nature of LIF measurements, It is easier to use the mole fraction χ and the number density n rather than the mass fraction and density, so, Equation 3.37 is rewritten as,

$$k_w \chi_{iw} n_w = n_w D_{iw} \frac{\partial \chi_i}{\partial y}\bigg|_w \tag{3.38}$$

Solving for the reaction rate gives

$$k_w = \frac{D_{iw}}{\chi_{iw}} \frac{\partial \chi_i}{\partial y}\bigg|_w \tag{3.39}$$

Through LIF it is fairly simple to measure a species "i" relative number density $n_{i,rel}$.

$$n_{i,rel} = c \cdot n_{i,abs} = \frac{A_p}{\tau_{obs} G_p} \int \frac{S_{TALIF}(\lambda)}{E^2(\lambda)} d\lambda \tag{3.40}$$

Using a model of the temperature distribution below the sample, and the static pressure. The total number density can be determined as a function of y,

$$n_{total}(y) = \frac{p}{kT_{fit}(y)} \tag{3.41}$$

Taking the ratio of the relative number density to the total number density gives a value proportional to the mole fraction χ^*

$$\chi_i^*(y) = \frac{n_{i,rel}(y)}{n_{total}(y)} = \frac{c \cdot n_{i,abs}(y)}{n_{total}(y)} = c \cdot \chi(y) \tag{3.42}$$

Plugging (χ_i^*/c) into Equation 3.39 in place of χ_i, gives,

$$k_w = c \frac{D_{iw}}{\chi_{iw}^*} \left(\frac{1}{c} \frac{\partial(\chi_i^*)}{\partial y}\bigg|_w + \chi_i^* \frac{\partial(c^{-1})}{\partial y}\bigg|_w \right) \tag{3.43}$$

Which, as long as c is not a function of y, reduces to the following.

$$\boxed{k_w = \frac{D_{iw}}{\chi_{iw}^*} \frac{\partial(\chi_i^*)}{\partial y}\bigg|_w} \tag{3.44}$$

From this result, a reaction rate k_w can be calculated from a boundary layer scan which tracks static pressure, temperature and relative number density. This can then be converted to a total atomic nitrogen removal efficiency γ_N using the following equation from Goulard [20].

$$\boxed{\gamma_N = k_w \sqrt{\frac{kT}{2\pi m_a}}} \tag{3.45}$$

3.7.2 Carbon Nitridation Rate and Efficiency

The carbon nitridation efficiency γ_{CN} is given by,

$$\gamma_{CN} = \frac{\Gamma_{CN}}{\Gamma_N} \tag{3.46}$$

where Γ_{CN} is the flux of CN molecules leaving the surface, and Γ_N is the flux of nitrogen atoms hitting the surface. Assuming carbon nitridation is the only significant carbon removal mechanism, Γ_{CN} can be calculated from the mass loss of the carbon sample. [11]

$$\Gamma_{CN} = \frac{\Delta m_{sample}}{m_C \Delta t A} \tag{3.47}$$

where A is the area of the sample face, and m_C is the mass of a carbon atom. Γ_N can be calculated from statistical mechanics assuming a Maxwellian velocity distribution [21],

$$\Gamma_N = \frac{n_N}{4} \sqrt{\frac{8kT}{\pi m_N}} \tag{3.48}$$

Where n_N is the absolute number density of nitrogen atoms at the wall, and m_N is the mass of a nitrogen atom. Plugging 3.47 and 3.48 into equation 3.46 gives,

$$\gamma_{CN} = \frac{4}{n_N} \frac{\Delta m_{sample}}{m_C \Delta t A} \sqrt{\frac{\pi m_N}{8kT}} \tag{3.49}$$

Unlike the total reaction efficiency, the absolute number density of nitrogen atoms is needed to calculate carbon nitridation efficiency. If desired k_{CN} may be calculated via Equation 3.45.

3.7.3 Nitrogen Recombination Rate

Assuming there are no other significant pathways for removal of nitrogen atoms from the boundary layer, the nitrogen recombination rate can be calculated from the total reaction rate (k_w) and the nitridation rate (k_{CN}).

$$k_{N_2} = k_w - k_{CN} \tag{3.50}$$

$$\gamma_{N_2} = \gamma_w - \gamma_{CN} \tag{3.51}$$

Chapter 4

Fluorescence Lifetimes

If a population in an upper electronic state has no mode of de-excitation other than spontaneous emission of a fluorescence photon, it will decay as a single exponential as given below.

$$S = e^{A_{21}t} = e^{t/\tau_r} \tag{4.1}$$

where A_{21} is the Einstein coefficient and $\tau_r = \frac{1}{A_{21}}$ is the radiative lifetime.

However, in reality there are various possible modes of de-population of the upper state. Two de-population modes of interest in this work are multi-photon ionization and collisional quenching.

Multi-photon ionization happens when an excited atom absorbs additional photons which have enough energy to eject an electron, moving the atom into a higher ionized energy state. In the derivation of S_{TALIF} in Appendix A, we assumed that multi-photon ionization would not occur. Luckily we can verify this claim. The signal from an n-photon process will be proportional to incident laser intensity raised to the nth power [22]. So, if $S_{TALIF} = CE^2$ then the dominant process at play is a two

photon process. Tests of the energy scaling of TALIF signal in both the FR and ICP gave scaling exponents between 1.9 and 2.2. This as well as the fact that temperature measurements did not seem to be sensitive to changes in laser fluence suggest that significant multi-photon ionization is not occurring for the fluence levels used in these experiments.

Collisional quenching on the other hand cannot be avoided. This will be discussed in the following section.

4.1 Collisional Quenching of Fluorescence

Collisions between particles provide a path for de-excitation of the upper state without the emission of a fluorescence photon. As the rate of collisions increases, it becomes more likely that the excited atom will have a collision before it spontaneously emits a photon.

We can say that the quenching from species B on the excited species A is proportional to the rate of AB collisions θ_{AB}. Which, in an equilibrium mixture, is given by [21]:

$$\theta_{AB} = \sqrt{2}\pi\left(\frac{d_A + d_B}{2}\right)^2 \bar{C}_A n_B \tag{4.2}$$

where d_A and d_B represent the collision cross sections of the two species, $\bar{C}$ is the mean molecular speed, and n_B is the number density of species B. From the ideal gas

equation of state

$$n_B = \frac{p_B}{kT} \tag{4.3}$$

The mean molecular speed from a Maxwellian distribution is given by: [21]

$$\bar{C} = \sqrt{\frac{8kT}{\pi m}} \tag{4.4}$$

Plugging these into Equation 4.2

$$\theta_{AB} = \sqrt{2}\pi\left(\frac{d_A + d_B}{2}\right)^2 \sqrt{\frac{8kT}{\pi m}} \frac{p_B}{kT} \tag{4.5}$$

Simplifying this equation suggests that the quenching rate in an equilibrium mixture, from collisions with species B is proportional to the partial pressure of that species over the square root of temperature.

$$Q_B = \frac{c_q p_B}{\sqrt{T}} \tag{4.6}$$

This corresponds to the values of observed lifetime shown in Figure 4.1

Because quenching rates are generally measured at room temperature, the $\sqrt{T}$ term is often grouped in with the constant making the equation

$$Q_B = k_q p_B \tag{4.7}$$

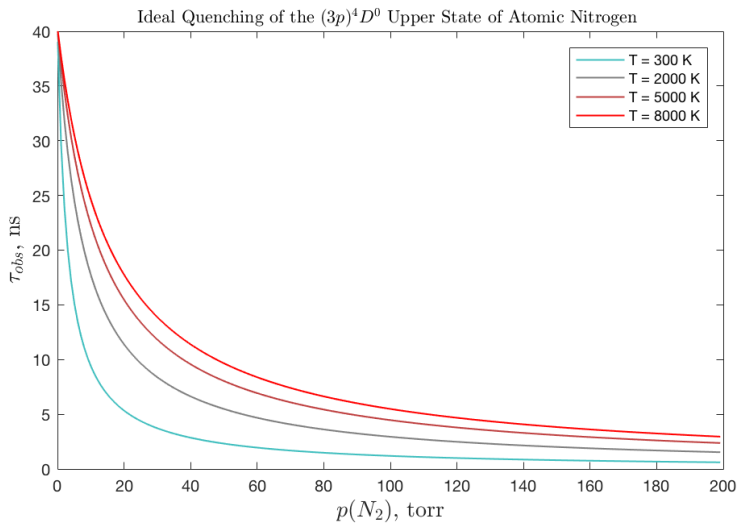

Figure 4.1: Model of Collisional Quenching as defined by Equation 4.6

4.1.1 A Note on Units

Quenching rates k_q are often reported in units of either [torr^{-1} s^{-1}] or [cm^3 s^{-1}] These represent the rate of change of the decay constants as a function of the partial pressure of the quencher (Equation 4.8), and the number density (Equation 4.9) of the quencher (i) respectively.

$$\frac{dQ}{dp_i} = [\text{torr}^{-1}\text{s}^{-1}] \tag{4.8}$$

To find the conversion factor, the derivative is expanded via the chain rule as shown below.

$$\frac{dQ}{dn_i} = [\text{cm}^3\text{s}^{-1}] = \frac{dQ}{dp_i}\left(\frac{dp}{dn}\right)_T \tag{4.9}$$

From the ideal gas equation of state $p = nk_bT$,

$$\left(\frac{dp}{dn}\right)_T = k_b T \tag{4.10}$$

Where $k_b = 1.03557(10)^{-19}$ $[torr\ cm^3\ K^{-1}]$ is Boltzmann's constant. Plugging this result back into Equation 4.9 gives the conversion factor.

$$[\mathrm{cm^3 s^{-1}}] = \frac{dQ}{dp_i} k_b T = [\mathrm{torr^{-1} s^{-1}}] k_b T \tag{4.11}$$

4.2 Fluorescence Modeling and Fitting

For cases when the lifetime is significantly longer than the laser pulse, a single exponential, fit to the section of the fluorescence after the laser pulse has passed, is sufficient for an accurate lifetime measurement.

$$\text{Exponential Fit} = Ae^{-Bt} \tag{4.12}$$

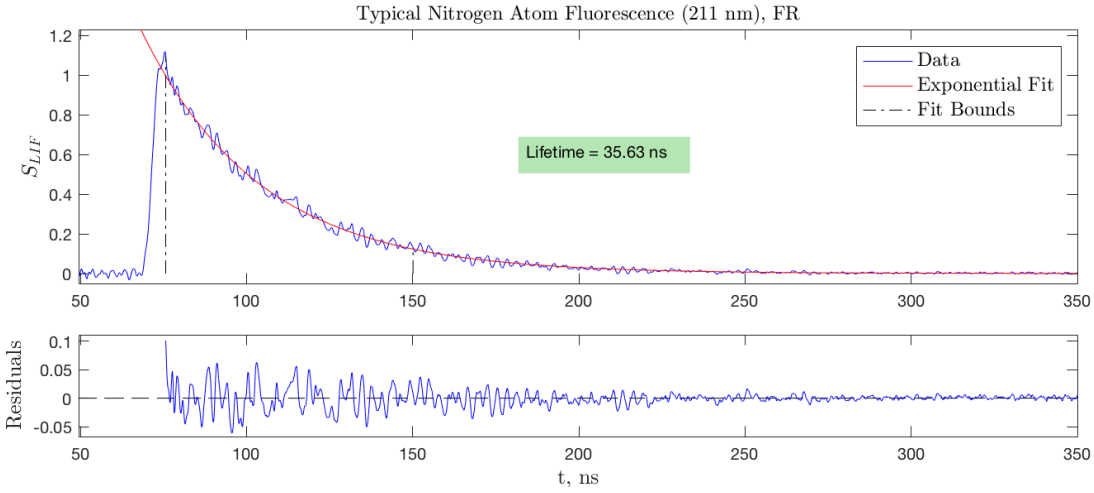

Figure 4.2: Single exponential decay fit applied to N atom fluorescence.

As collisions shorten the observed lifetime, the bulk of the decay happens while the laser pulse is still exciting particles in the probe volume. This means a single exponential is no longer a valid fit for the fluorescence signal. To avoid this issue, the line-shape of the fluorescence is modeled as a Gaussian laser pulse convolved with an exponential decay function. This can be derived from the rate equations governing TALIF. The number of fluorescence photons per unit volume is given by [13]

$$N_{h\nu} = \frac{A\hat{\sigma}^{(2)} N_0 U^2(r,z)}{(h\nu)^2} \int_{-\infty}^{\infty} e^{-(A+Q)t'} \int_{-\infty}^{t'} F^2(t'') e^{(A+Q)t''} dt'' dt' \tag{4.13}$$

The fluorescence line-shape is given by the segment inside the integral. This can be simplified by assuming a temporally Gaussian laser pulse of the form:

$$F(t) = \frac{e^{-(t^2/2\sigma^2)}}{\sigma\sqrt{2\pi}} \tag{4.14}$$

Plugging this into Equation 4.13, and computing the running integral gives the Gaussian-exponential convolution (GEC) fit function with 3 parameters (A, B, σ).

$$\text{GEC Fit} = Ae^{-Bt}\left[1 + erf\left(\frac{t}{\sigma} - \frac{(B)\sigma}{2}\right)\right] \tag{4.15}$$

Where σ is the standard deviation of the laser pulse.

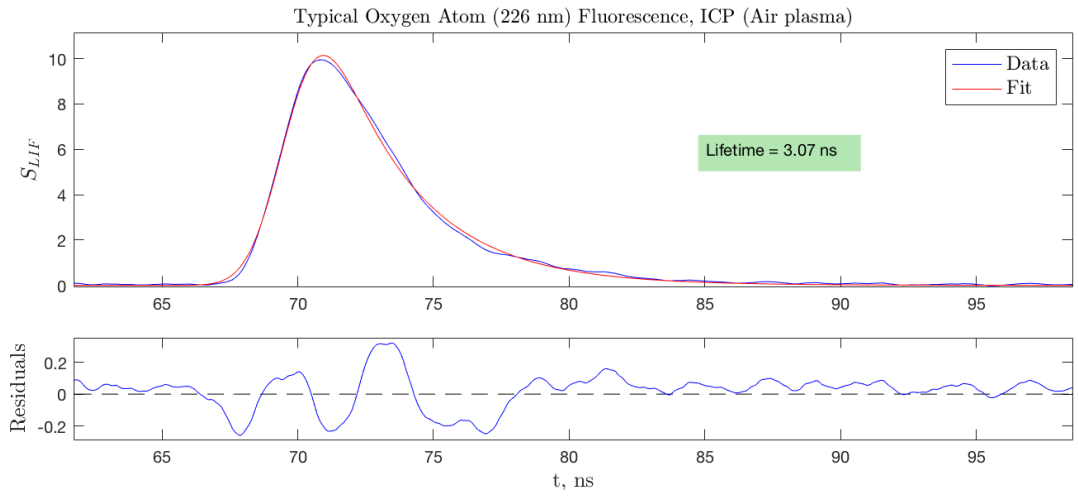

Figure 4.3: GEC fit applied to oxygen atom fluorescence.

This does seem to be a good fit. However, even with the R9880, it may be necessary to take into account the time response of the PMT. When the lifetimes

measured are very short, the measured signal may be dominated by the transit time spread (TTS) of the PMT instead of the true decay of the fluorescence.

In Section 3.4.3 of his work, [23] Adams models the time response (Ω) of a PMT as:

$$\Omega(t) = \frac{1}{\delta} e^{-t/\delta} \tag{4.16}$$

δ is calculated by fitting a numerical convolution of the laser pulse and the instrument time response function Ω, to the same laser pulse measured with the PMT in question. The laser pulse shape can be measured with a bi-planar phototube as the time response of the BPPT (ps) is orders of magnitude greater than the width of the laser pulse (ns). Convolving Ω with the fluorescence lineshape assuming a Gaussian laser pulse gives

$$\Phi(t) = A\Big[\Big(erf\Big(\frac{x}{\sigma}\Big) + 1\Big)e^{(\delta^{-1}-\tau^{-1})x} - e^{\frac{\sigma^2}{4}(\delta^{-1}-\tau^{-1})^2} erf\Big(\frac{x}{\sigma} - \frac{\sigma}{2\delta} + \frac{\sigma}{2\tau}\Big)\Big]_{-\infty}^{t'} \tag{4.17}$$

Where x is the variable of integration, and $t' = t - \sigma^2/2\tau$. For cases where $\tau > \delta$ this converges nicely to

$$\Phi(t) = A\Big[e^{\sigma^2/4\tau^2}\Big[erf\Big(\frac{t}{\sigma} - \frac{\sigma}{2\tau}\Big) + 1\Big]e^{-t/\tau} - e^{\sigma^2/4\delta^2}\Big[erf\Big(\frac{t}{\sigma} - \frac{\sigma}{2\delta}\Big) + 1\Big]e^{-t/\delta}\Big] \tag{4.18}$$

The GEC-PMT fit $\Phi(t)$ is shown below for the same data used in Figure 4.3. Notice that this improved fit shows what appears to be a reflection of the fluorescence trace

in the residuals.

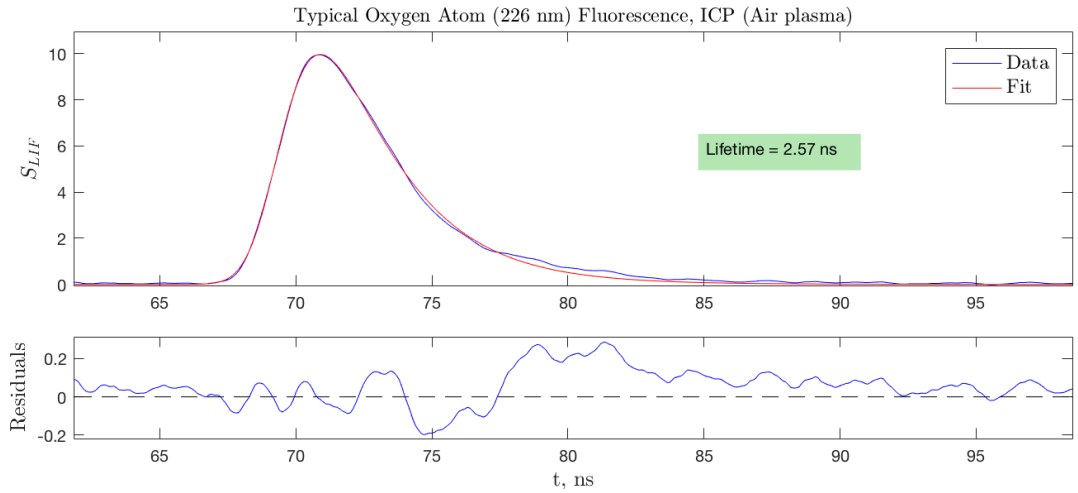

Figure 4.4: GEC-PMT fit applied to oxygen atom fluorescence.

For cases when $\tau < \delta$, the expression in Equation 4.17 becomes indeterminate. Due to collisional quenching, lifetimes in the ICP torch are shortened to ≈ 1 ns which means $\tau < \delta$ for our typical "side-on" PMT ($\delta \approx 5$ for R636.) So instead a faster "head-on" PMT is used which is able to resolve the short torch lifetimes. See section 2.4 for information on the PMTs used in this study.

Figure 4.5 shows the effect of PMT time response on a quenched oxygen atom fluorescence.

In measurements of absolute number density using the R9880 PMT, an exponential fit was used to extract lifetimes in the flow reactor, and a GEC-PMT fit was used to calculate lifetimes in the plasma. A numerical study of the various lifetime fitting techniques is included in Appendix D.

For cases when the observed lifetime is far greater than the width of the laser pulse, such as in lifetime measurements of nitric oxide in the FR, the lineshape of

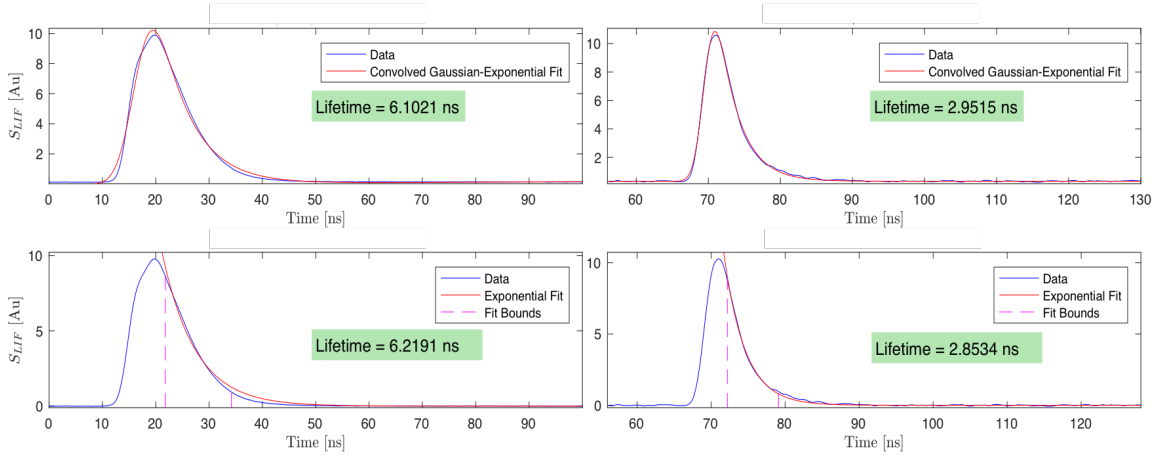

Figure 4.5: Left: "Slow" R636 PMT. Right: "Fast" R9880u-20 PMT. Oxygen atom fluorescence at approximately the same condition.

the fluorescence essentially becomes $H(t-t_0)C\exp(-(t-t_0)/\tau)$. Where $H(t)$ is the Heaviside function, and C is a scaling factor. In this case the lifetime may be extracted from the integrated area of the fluorescence in a method similar to the calculation of beam widths in Section 3.6. To start, take the integral of the fluorescence signal I_1, as well as the integral of the squared fluorescence signal I_2.

$$I_1 = \int_0^\infty Ce^{-t/\tau}dt = C\tau \tag{4.19}$$

$$I_2 = \int_0^\infty \left(Ce^{-t/\tau}\right)^2 dt = \frac{C^2}{2}\tau \tag{4.20}$$

Using these two results, τ can be found from the following equation.

$$\tau = \frac{1}{2}\left(\frac{I_1}{\sqrt{I_2}}\right)^2 \tag{4.21}$$

This method is not particularly useful for lifetime measurements in the ICP, but with significant mathematical effort, and a high confidence measurement of the temporal

laser width, it may be possible to create a similar method which uses a more complex fluorescence lineshape such as in Equation 4.15 or 4.18

Chapter 5

Results & Discussion

5.1 Beam Area A_p

Example beam profiles recorded at 226 nm are shown in Figure 5.1 and 5.2. When the beam delivery aperture is fairly small (1-2 mm) the beam can be well approximated as Gaussian. However, as the beam delivery aperture becomes larger this assumption fails as there are many peaks and troughs throughout. For either case an equivalent Gaussian width can be calculated as outlined in section 3.6. The results of these fits are shown in Figures 5.3 through 5.6. The beam profiles in the ICP include the trend of beam area with delivery aperture. Using an aperture before the laser is sent into the ICP allows for better spatial resolution in boundary layer scans. There is no beam delivery aperture at the FR because the spatial resolution in the FR is not important to measurements of temperature or number density.

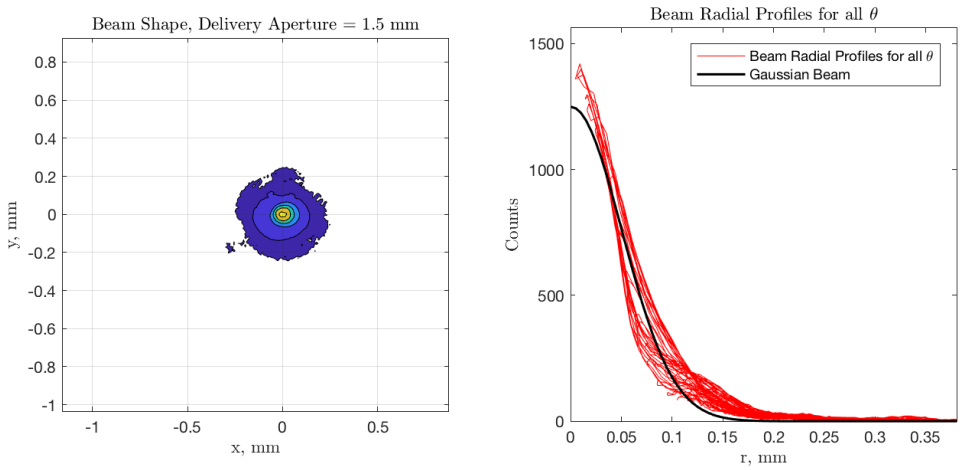

Figure 5.1: Example beam profile with a small delivery aperture resulting in a nearly Gaussian beam.

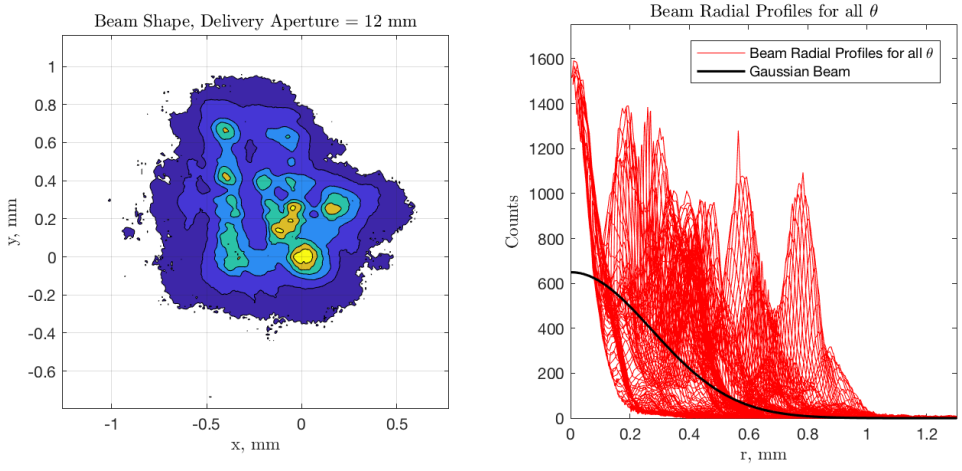

Figure 5.2: Example beam profile with a fully open delivery aperture shows many peaks and troughs.(Delivery translation stage at 15.28mm)

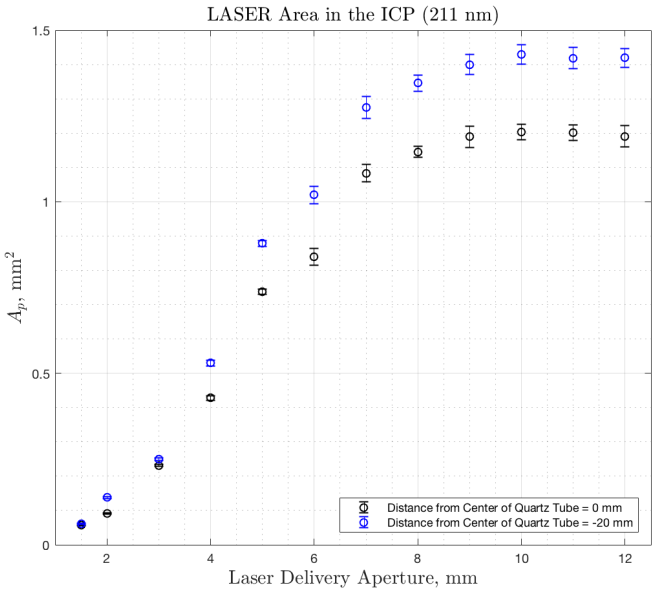

Figure 5.3: Beam area trend with delivery aperture in the ICP for $\lambda = 211$ nm.(Delivery translation stage at 15.28mm)

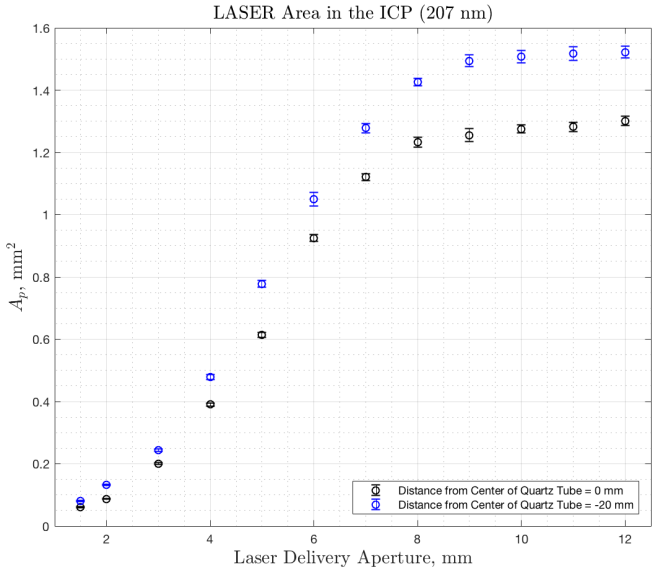

Figure 5.4: Beam area trend with delivery aperture in the ICP for $\lambda = 207$ nm.

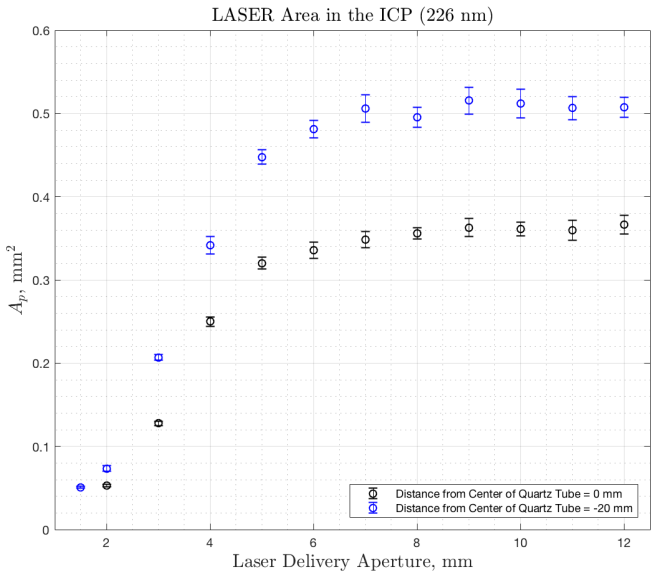

Figure 5.5: Beam area trend with delivery aperture in the ICP for $\lambda = 226$ nm.

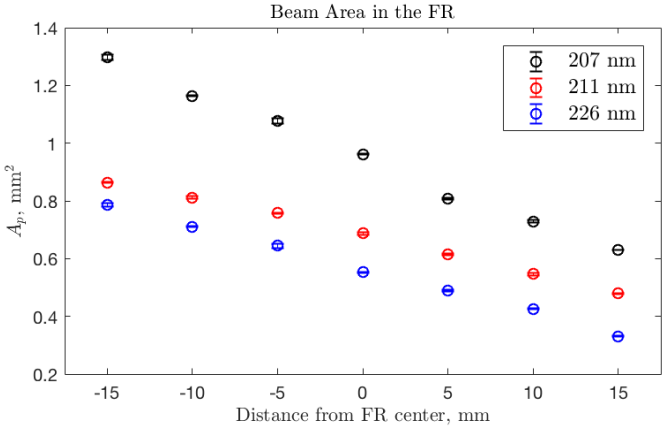

Figure 5.6: Beam area trend with probe location in the FR for all λ.

5.2 Collisional Quenching

In order to build confidence in measurements of fluorescence lifetime, collisional quenching rates were measured and compared to published values for nitrogen atoms excited at both 211 nm and 207 nm. Figure 5.7 compares measurements of collisional quenching of the $(3p)^4D^0$ upper state of atomic nitrogen by N_2 gas molecules. The radiative lifetime and quenching rate measured in the FR agree within the error of the measurements with the values given by Adams and Miller [24].

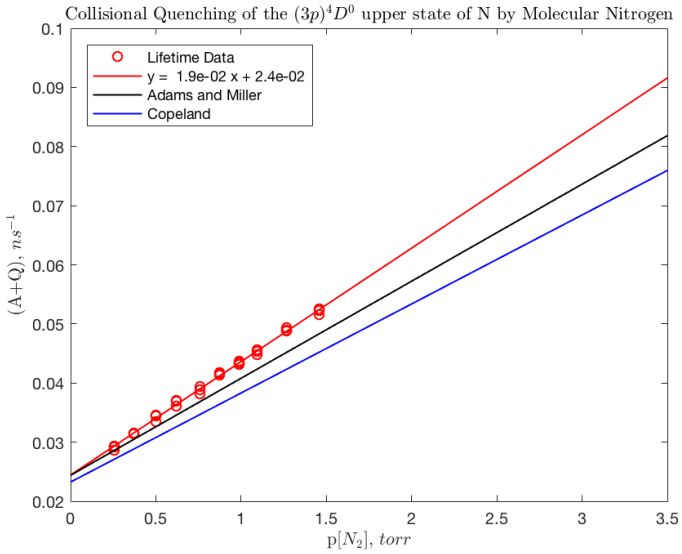

Figure 5.7: Comparison of quenching rate measurements for ground state atomic nitrogen excited by a 211 nm laser.

Table 5.1: N_2 Quenching rates of the $(3p)^4D^0$ upper state of atomic Nitrogen (211 nm excitation)

Author	k_q [10^{-10} cm^3 s^{-1}]	τ_r [ns]
Ours	5.9 ± 0.3	41 ± 2
Adams and Miller [24]	5.1 ± 0.5	41 ± 5
Bischel [25]	2.4 ± 0.6	27 ± 3
Copeland [26]	4.6 ± 0.6	43 ± 3

N_2 quenching rate measurements of the $(3p)^4S^0$ upper state of atomic nitrogen, (Figure 5.8), also agree within the bounds of error with the values given by Adams and Miller.

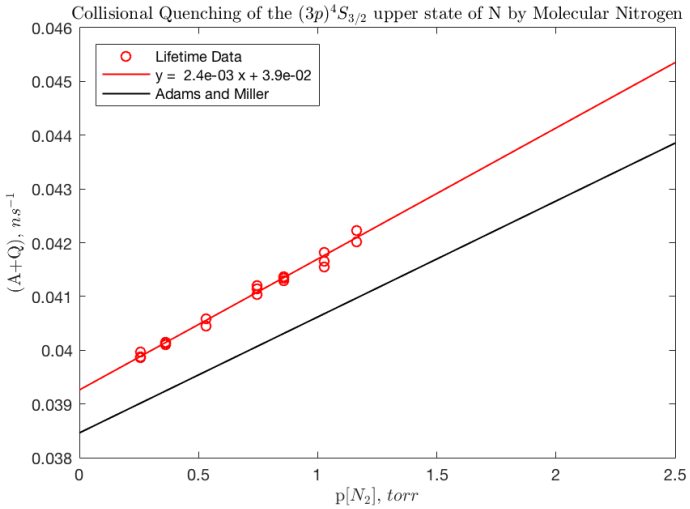

Figure 5.8: Comparison of quenching rate measurements for ground state atomic nitrogen excited by a 207 nm laser.

Table 5.2: N_2 Quenching rate of the $(3p)^4S^0_{3/2}$ upper state of atomic Nitrogen (207 nm excitation)

Author	k_q [10^{-11} cm^3 s^{-1}]	τ_r [ns]
Ours	7.4 ± 0.7	25.5 ± 2
Adams and Miller [24]	6.7 ± 0.9	26 ± 2

These tests, like many studies of collisional quenching, were performed at room temperature and at pressures between 0-2 torr. However, for the purpose of absolute number density measurements in the ICP, lifetimes will need to be measured at 160 torr and between 5000 K and 7500 K. Figure 5.9 compares the observed lifetime of the $(3p)^4D^0$ upper state in various plasma conditions to the ideal pressure and temperature scaling of quenching developed in Section 4.1. N_2 partial pressures for each temperature and pressure were determined assuming equilibrium chemistry. Excluding the leftmost data point (which is in a predominantly argon plasma) the lifetime trend matches well with the expected values, especially for data points corresponding to low argon flow rates (see Table 5.3). It should be noted that the ideal quenching values are calculated for quenching by N_2 only, any quenching by argon, or self quenching by atomic nitrogen is ignored here.

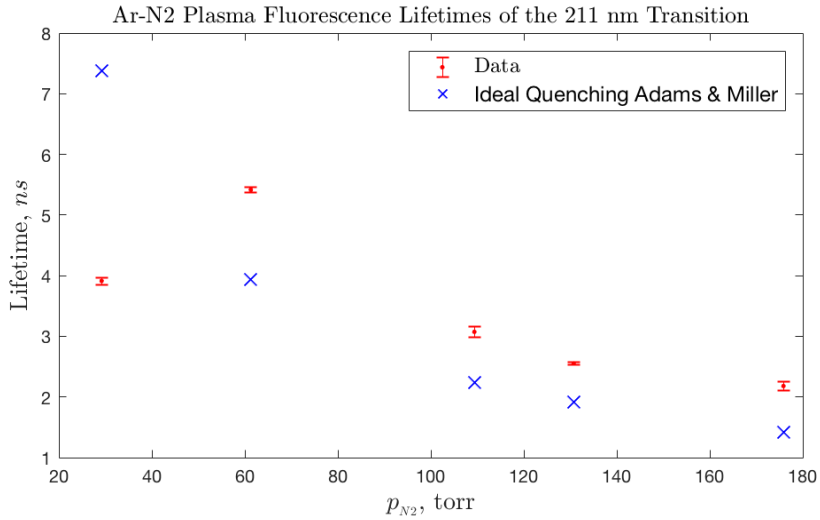

Figure 5.9: Observed lifetimes of the $(3p)^4D^0$ upper state at high temperature and moderate pressure. (211 nm excitation)

Table 5.3: ICP facility conditions for Figure 5.9. Partial pressures calculated using CEA [6] at the measured temperature and pressure.

$p(N_2)$ [torr]	Ar [LpM]	N_2 [LpM]	p [torr]	T [K]	τ_{obs} [ns]
29	28.5	8.5	160	5421	3.9
61	18.2	18.1	160	5583	5.4
109	7.8	27.6	160	5266	3.1
130	0.9	36.1	160	5415	2.6
176	0.9	36.1	200	5211	2.2

Two-photon excitation of atomic nitrogen at 207 nm is often tauted as superior to its 211 nm counterpart due to its comparatively low quenching rate. At low pressures this does seem to be reasonable. Extrapolating this quenching rate to conditions seen in the ICP predicts an observed lifetime of around 9 ns. However, unlike the measurements of the $(3p)^4D^0$ upper state (Figure 5.9), measurements of the $(3p)^4S^0_{3/2}$ upper state do not agree with this prediction. Instead, measured lifetimes are around 2.1 ns.

5.3 Collisional Upper-State Transfer

The high temperature, moderate pressure conditions in the torch seem to unlock a new pathway for de-population of the $(3p)^4S^0_{3/2}$ upper state. N-atoms excited by 207 nm light can be seen fluorescing from both the $(3p)^4S^0_{3/2}$ and $(3p)^4D^0$ upper states, suggesting that other upper states are being populated via collisional energy transfer.

Figures 5.11 and 5.12 show evidence of this phenomena in the ICP. Spectrally resolved fluorescence from the TALIF probe volume in a nitrogen plasma show emission from both the $(3p)^4S^0_{3/2}$ and the $(3p)^4D^0$ upper states of atomic nitrogen for laser excitation at both 207 nm and 211 nm.

Test Details:

- N_2 plasma, 160 Torr, 5500-6000 K
- Spectrometer: Isoplane SCT 320
- Camera: PIMAX4:512EM
- Grating: 600 g/mm, 500 nm blaze
- emiCCD gain = 10000
- On CCD accumulations = 1
- Gate Settings: Delay $\approx$ 1140 ns, width = 40 ns
- 500 averages per Spectra
- Slit width: 10 μm for 207 nm excitation, 500 μm for 211 nm excitation

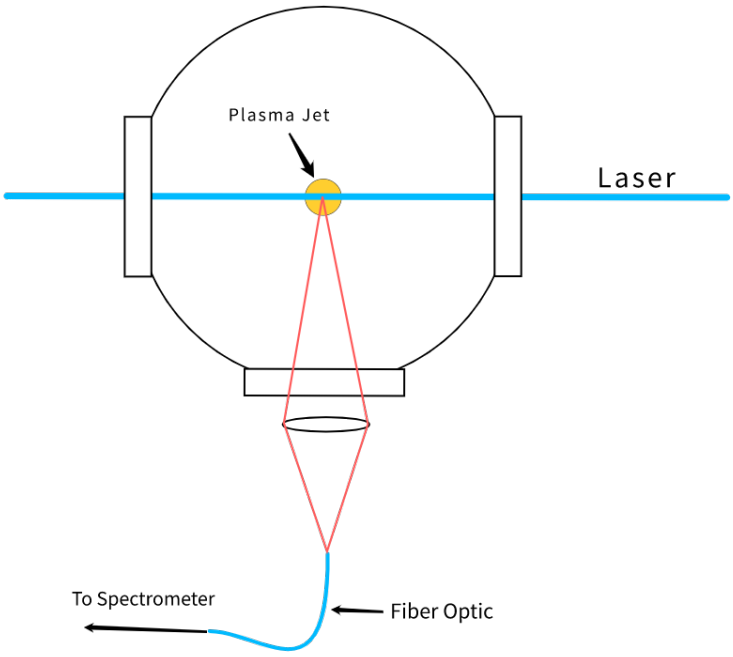

Figure 5.10: Diagram of experimental set-up for test of collisional upper-state transfer.

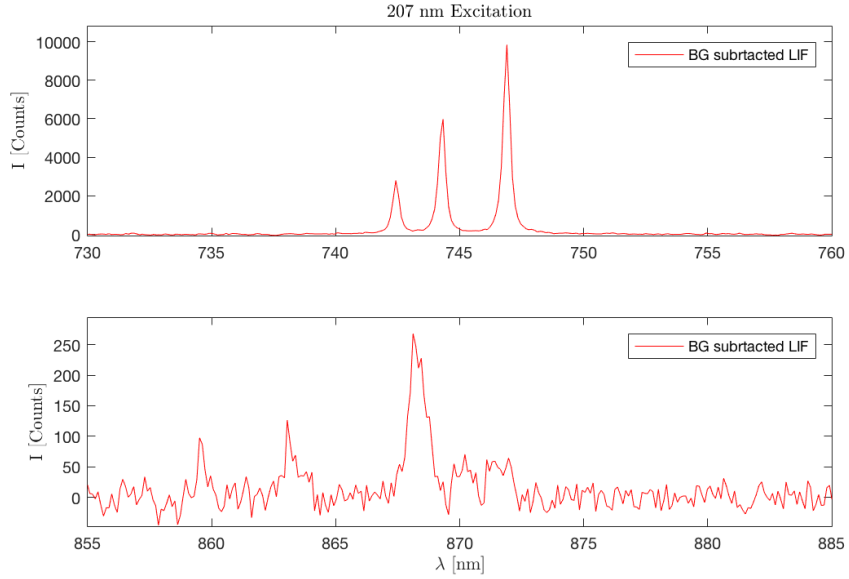

Figure 5.11: 2-photon excitation at 207 nm causes emission at both 745 and 868 nm

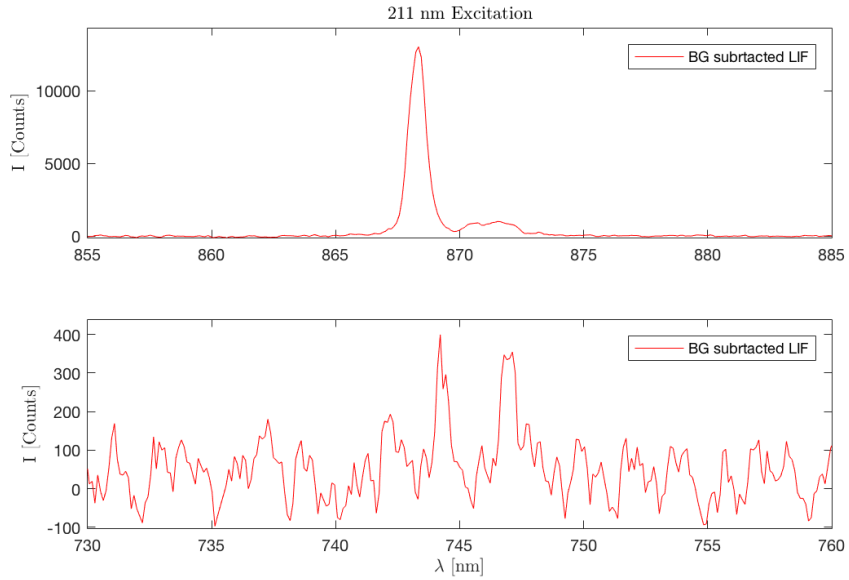

Figure 5.12: 2-photon excitation at 211 nm causes emission at both 745 and 868 nm

Work by Westblom et al. [27] had shown evidence of strong upper state transfer in atmospheric pressure flames. It seems reasonable that this effect is significantly

smaller in the modest pressures seen in the ICP facility as the particle collision rate is roughly proportional to the pressure. The results in Figures 5.11 and 5.12 have not been corrected for differences in collection efficiency at 745 nm vs 869 nm, and as such are meant to provide qualitative evidence of upper state transfer in the ICP torch.

Initial work in the FR also showed evidence of a small amount of collisional transfer. However these tests were performed with band-pass filters instead of a spectrometer, so additional work would be needed to definitively show which state the measured fluorescence is coming from.

Upper state collisional transfer represents a complication to modelling the quenching dynamics of species in the ICP. However, it should not affect measurements of absolute number density because this depopulation of the upper state is accounted for in the measurement of the observed lifetime.

5.4 Absolute Number Density

Number density measurements in both air and nitrogen plasmas are presented in the following section. TALIF scans and lifetimes will be presented for atomic nitrogen in an air plasma, the corresponding data for oxygen atoms in an air plasma and nitrogen atoms in a nitrogen plasma will be presented in Appendix B so as to avoid overwhelming the reader. Atomic nitrogen was probed using the 211 nm transition because the laser light for the alternative 207 nm transition is absorbed by recirculating nitric oxide, making it difficult to extract reliable results in air plasmas.

Figures 5.13 and 5.14 show the relative difference in TALIF signal between the

plasma jet and flow reactor which is the baseline for number density measurements.

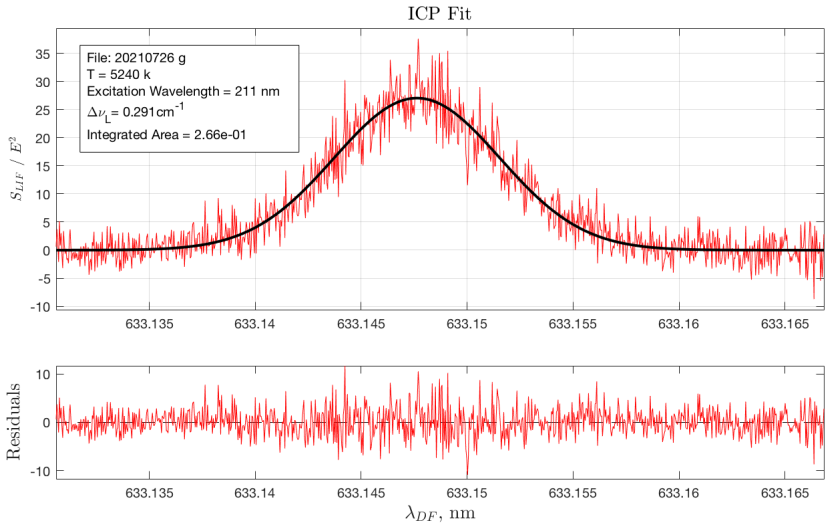

Figure 5.13: Fit of N (211 nm) TALIF scan in an air plasma.

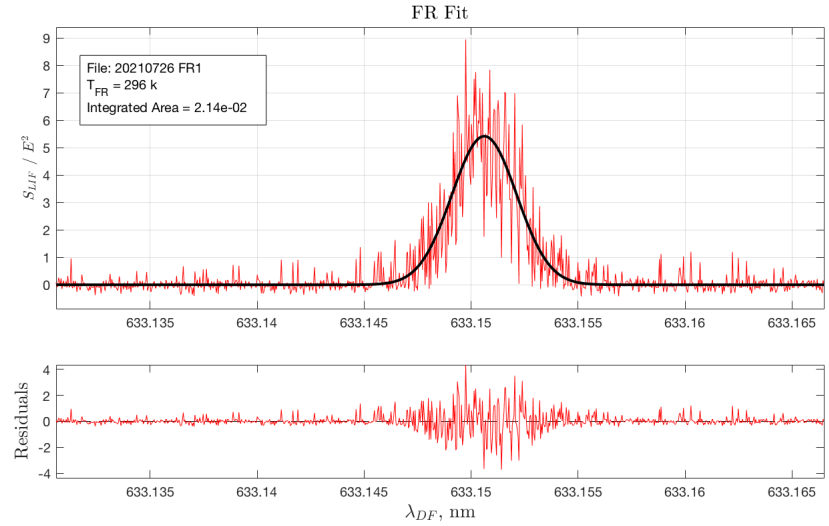

Figure 5.14: Calibration Scan of N (211 nm) in the Flow Reactor

Measurements of observed lifetime in the plasma (Figure 5.15) show that as expected there is far more collisional quenching in the ICP than in the FR. Given a

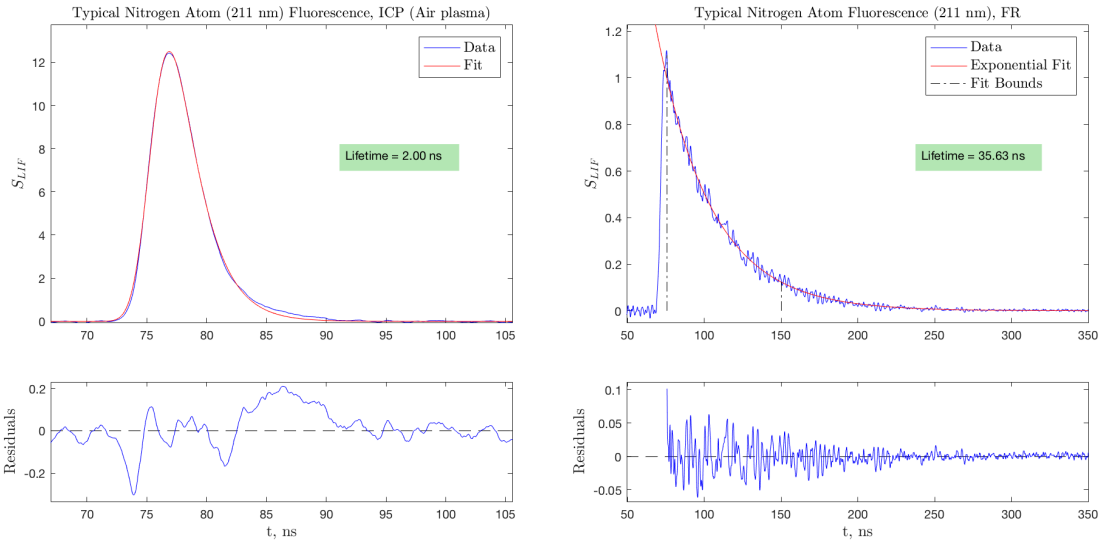

(a) Nitrogen atom fluorescence trace the ICP. *(b) Nitrogen atom fluorescence trace in the FR.*

Figure 5.15: Comparison of typical fluorescence lifetimes in the ICP and FR

radiative lifetime of 41 ns for the $(3p)^4D^0$ upper state of atomic nitrogen, [24], and the flourescence quantum yield given by τ_{obs}/τ_{rad}, the integrated TALIF signal seen in the flow reactor, corresponds to 86% of the initially excited nitrogen atoms. While the much larger TALIF signal seen in the ICP corresponds to only 5% of the initially excited nitrogen atoms present in the plasma.

Examining the residuals of the ICP fluorescence trace shows what appears to be a reflection of the fluorescence signal. This effect is seen to varying degrees in all lifetime measurements which are shorter than $\approx$ 3 ns. The cause for this has not been definitively proven. It is possible that the reflection is coming from an impedance mismatch between the PMT and the oscilloscope. Both are set to have a 50 Ω impedance, but the oscilloscope does get noticeably hot while in use which may be effecting its properties. Another possibility is that atomic species are being

collisionally transferred to a second upper state, and then back into the initial upper state. If the collision cross-sections are large enough, this would likely have the effect of extending the tail of the fluorescence.

Figure 5.16 shows the result of a nitric oxide titration in the flow reactor which provides a nitrogen atom number density of $6.3(10^{13})$ molecules/cm^3. Previous methods of performing the titration had resulted in hysteresis between the slope measured as the NO flowrate was increased and decreased. This was due predominately to the dye laser slowly shifting its output wavelength over the course of the 20-30 minute titration. To avoid this issue a full wavelength scan of the transition is performed at each NO flowrate, and the integrated area of each scan is used to determine the atomic nitrogen concentration.

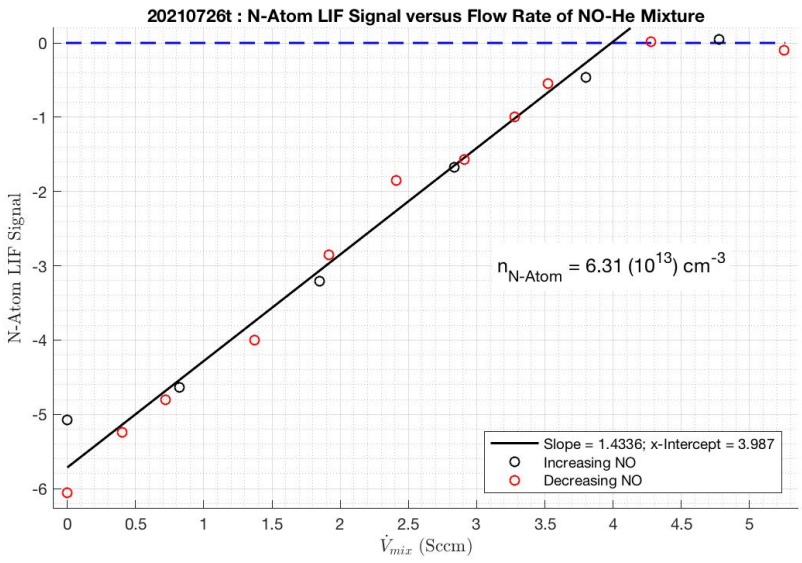

Figure 5.16: NO titration in the Flow Reactor

Applying the corrections for the photo-multiplier tube gain, beam area etc. as outlined in Section 3.4.2, gives the absolute number densities shown in Figures 5.17 and

5.18. These plots compare the measured values of temperature and species density to those calculated for an equilibrium air mixture at the same temperature and pressure. Equilibrium chemistry is determined using the program "Chemical Equilibrium with Applications" (CEA) [6]. Error bars in these plots represent a quantification of random error, and as such do not account for any systematic error which may still be present in the measurements.

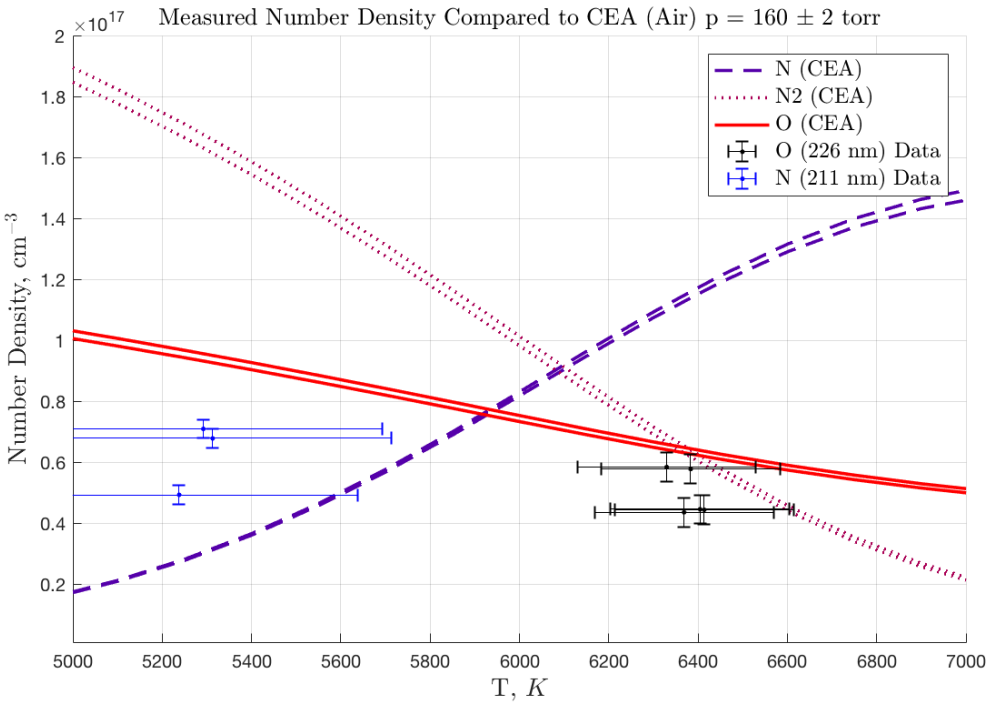

Figure 5.17: Comparison of number density measurements to CEA for an air plasma

The measured densities for both oxygen and nitrogen atoms suggest near equilibrium conditions for the plasma flow. However, the measurements were taken at nearly identical plasma conditions, so the 1000 K difference between the recorded temperatures is worth noting. This is an ongoing issue which should be resolved.

One possible mechanism for the differences in the measured temperatures is col-

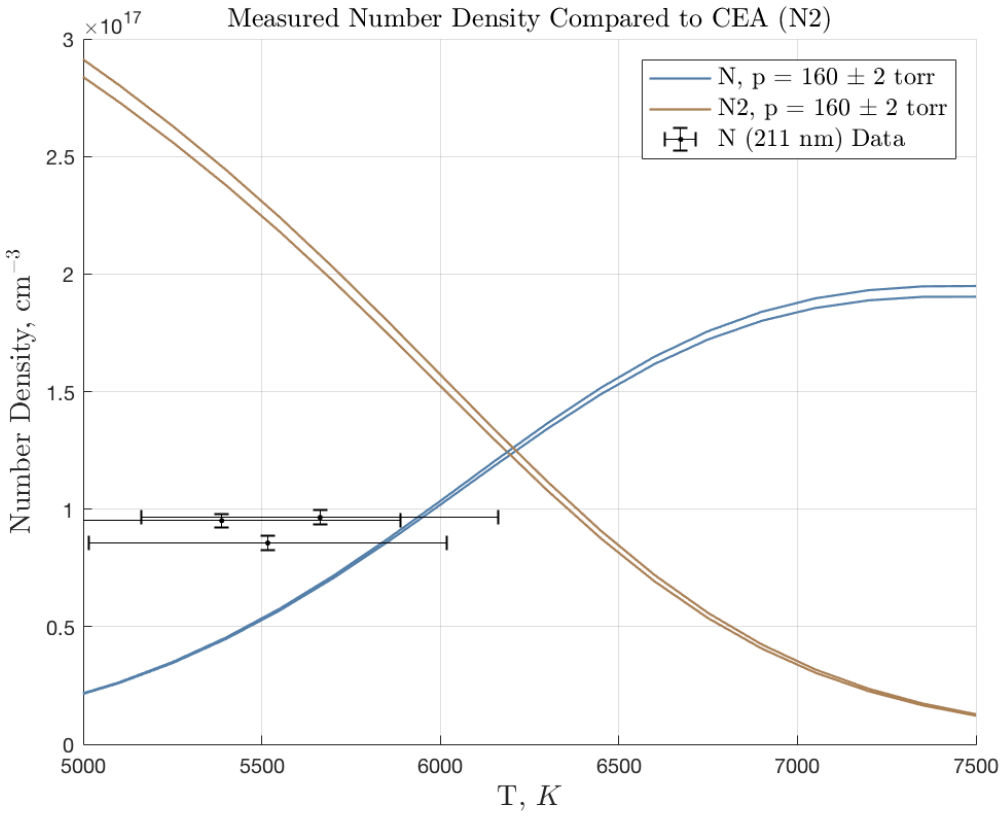

Figure 5.18: Comparison of number density measurements to CEA for a Nitrogen plasma

lisional broadening. As the collision rates are different for the two atomic species, it is likely that taking collisional broadening into effect would have a varied effect on the two temperature measurement techniques. Collisional broadening results in a Lorentzian distribution, so the net lineshape of combined collisional and Doppler broadening would be a Voigt lineshape. If collisional broadening were significant, there would likely be larger residuals in the wings of a Gaussian fit. Due to the relatively flat residuals seen in a Gaussian fit, collisional broadening has been considered negligible in the ICP conditions. A Doppler-free measurement of the transition widths in the ICP and FR could be useful to verify this assumption.

Another possible mechanism for differences in the temperature measurement is the apparent variation of the observed lifetime with excitation wavelength. Data collected in the ICP shows a decrease of about 20% in the lifetimes measured at the wings of the transition compared to the line-center. Work is still needed to determine if this is a physical phenomenon or an effect that arises from the significantly lower signal levels seen at the wing of the transition. Either way this may need to be accounted for in measurements of both temperature and number density. Work on this subject is presented in Appendix E.

Chapter 6

Conclusions

This thesis aimed to improve absolute number density measurements in UVM's inductively coupled plasma torch to provide a method for future work in the study of high temperature gas-surface interactions. Quantification of the laser beam width and PMT gain allowed for direct calibration of relative number densities using a flow tube reactor as a reference source for the species of interest. Improvements in lifetime fitting techniques as well as the use of a PMT with faster time response allowed for resolution of the highly quenched fluorescence lifetimes seen in the ICP torch. Number densities of nitrogen and oxygen atoms measured with these techniques suggest near equilibrium conditions in the free stream of air and nitrogen plasmas.

Applying this technique to measurements of surface reaction rates will likely require the use of both the R636 and R9880 PMTs. The former does not have the temporal resolution to measure the highly quenched lifetimes, and the latter does not handle the continuous blackbody emission from a sample well.

Future work is needed to determine the cause of an apparent discrepancy between

temperature measurements of atomic nitrogen and atomic oxygen. As well as to determine the cause of the unexpected variation of observed lifetime with excitation wavelength. In addition to these puzzles, the increased resolution of lifetime measurements will allow for studies of collisional quenching dynamics in the conditions seen in the ICP.

Bibliography

[1] Baals D. D. & Corliss W. R. *Wind tunnels of NASA.*

[2] Michael Wright, Ioana Cozmuta, Bernard Laub, Yih-Kanq Chen, and William H. Wilcoxson. *Defining Ablative Thermal Protection System Margins for Planetary Entry Vehicles.*

[3] Walt Owens, Juergen Uhl, Max Dougherty, Andrew Lutz, Douglas Fletcher, and Jason Meyers. *Development of a 30kW Inductively Coupled Plasma Torch for Aerospace Material Testing.*

[4] Hakamata et al. *Photomultiplier Tubes: Basics and applications, Third Edition.* Hamamatsu, 2007.

[5] K Niemi, V Schulz von der Gathen, and H F DÄśbele. Absolute atomic oxygen density measurements by two-photon absorption laser-induced fluorescence spectroscopy in an RF-excited atmospheric pressure plasma jet. *Plasma Sources Science and Technology*, 14(2):375–386, apr 2005.

[6] S. Gordon and B. J. McBride. "computer program for calculation of complex chemical equilibrium compositions and applications". NASA Reference Publication 1311, 1996.

[7] M. Adler et al. Entry, descent and landing roadmap - technology area 09.

[8] Prasun Desai, Robert Mitcheltree, F. Cheatwood, Prasun Desai, Robert Mitcheltree, and F. Cheatwood. *Entry dispersion analysis for the Stardust comet sample return capsule.*

[9] David Driver and Matthew MacLean. Improved predictions of pica recession in arc jet shear tests. 01 2011.

[10] Luning Zhang, D. Pejaković, J. Marschall, M. Dougherty, and D. Fletcher. Laboratory investigation of the active nitridation of graphite by atomic nitrogen. *Journal of Thermophysics and Heat Transfer*, 26:10–21, 2012.

[11] Andrew Lutz. *Experimental Investigation And Analysis Of High-Enthalpy Nitrogen Flow Over Graphite*. PhD thesis, University of Vermont, 2015.

[12] Walt Owens. Development of a 30 kw inductively-coupled plasma torch for high temperature aerospace material testing at uvm. Master's thesis, University of Vermont, 2010.

[13] Douglas J. Bamford, Leonard E. Jusinski, and William K. Bischel. Absolute two-photon absorption and three-photon ionization cross sections for atomic oxygen. *Phys. Rev. A*, 34:185–198, Jul 1986.

[14] William K. Bischel, Douglas J. Bamford, and Leonard E. Jusinski. Absolute calibration of a fluorescence collection system by raman scattering in h2. *Appl. Opt.*, 25(7):1215–1221, Apr 1986.

[15] K Niemi, V Schulz von der Gathen, and H F DĂśbele. Absolute calibration of atomic density measurements by laser-induced fluorescence spectroscopy with two-photon excitation. *Journal of Physics D: Applied Physics*, 34(15):2330–2335, jul 2001.

[16] H F DĂśbele, T Mosbach, K Niemi, and V Schulz von der Gathen. Laser-induced fluorescence measurements of absolute atomic densities: concepts and limitations. *Plasma Sources Science and Technology*, 14(2):S31–S41, may 2005.

[17] Jay B. Jeffries, Richard A. Copeland, and David R. Crosley. Intramultiplet energy transfer in the collisions of 3pâ4d0 nitrogen atoms with nitrogen molecules. *The Journal of Chemical Physics*, 91(4):2200–2205, 1989.

[18] J. Marschall. Calculating an equivalent gaussian beam waist from spirocon data, personal communication, sri international, June 2000.

[19] D. G. Fletcher and J. M. Meyers. Surface catalyzed reaction efficiencies in oxygen plasmas from laser-induced fluorescence measurements. *Journal of Thermophysics and Heat Transfer*, 31(2):410–420, 2017.

[20] R. GOULARD. On catalytic recombination rates in hypersonic stagnation heat transfer. *Journal of Jet Propulsion*, 28(11):737–745, 1958.

[21] W.G. Vincenti and C.H. Kruger. *Introduction to Physical Gas Dynamics*. Wiley, 1965.

[22] B R Marx, J Simons, and L Allen. The effect of laser linewidth on two-photon absorption rates. *Journal of Physics B: Atomic and Molecular Physics*, 11(8):L273–L277, apr 1978.

[23] Steven F. Adams. Studies of atomic nitrogen in low pressure discharges by two-photon laser induced fluorescence. 1999.

[24] Steven F. Adams and Terry A. Miller. Two-photon absorption laser-induced fluorescence of atomic nitrogen by an alternative excitation scheme. *Chemical Physics Letters*, 295(4):305–311, 1998.

[25] William K. Bischel, Bryce E. Perry, and David R. Crosley. Two-photon laser-induced fluorescence in oxygen and nitrogen atoms. *Chemical Physics Letters*, 82(1):85–88, 1981.

[26] Copeland R. A. Radiative lifetime and quenching of the $3p^4d^0$ state of atomic nitrogen. *J. Chem. Phys.*, 86:4876, 1987.

[27] Ulf Westblom, Sara Agrup, Marcus Aldén, and Per Cederbalk. Detection of nitrogen atoms in flames using two-photon laser-induced fluorescence and investigations of photochemical effects. *Appl. Opt.*, 30(21):2990–3002, Jul 1991.

Appendix A
TALIF Signal Derivation

Assuming the ground state does not become depleted, The rate equations describing a 3 state TALIF system are as follows [13]. Subscripts 0, 2 and + refer to the ground, excited and ionized energy states respectively.

$$\frac{d\mathbf{N_0}(r,z,t)}{dt} = -\hat{\sigma}^{(2)}\Phi^2(r,z,t)\mathbf{N_0}(r,z,t) \tag{A.1}$$

$$\frac{d\mathbf{N_2}(r,z,t)}{dt} = \hat{\sigma}^{(2)}\Phi^2(r,z,t)\mathbf{N_0}(r,z,t) - (A+Q)\mathbf{N_2}(r,z,t) - \sigma_{pi}\Phi^a(r,z,t)\mathbf{N_2}(r,z,t) \tag{A.2}$$

$$\frac{d\mathbf{N}_+(r,z,t)}{dt} = \sigma_{pi}\Phi^a(r,z,t)\mathbf{N_2}(r,z,t) \tag{A.3}$$

Where a is the number of additional photons needed to ionize the excited atom. Solving these rate equations gives a relation for the number density of upper state atoms $N_2(r,z,t')$

$$N_2(r,z,t') = e^{-[(A+Q)t+\sigma_{pi}\theta(r,z,t')]}\hat{\sigma}^{(2)}N_0\int_{-\infty}^{t'}\Phi^2(r,z,t'')e^{[(A+Q)t''+\sigma_{pi}\theta(t'')-\hat{\sigma}^{(2)}\Omega(t'')]}dt'' \tag{A.4}$$

The total number of fluorescence photons emitted from the upper state is given by

$$N_{h\nu} = \int_{-\infty}^{\infty} AN_2(r,z,t')dt' \tag{A.5}$$

Where A is the spontaneous emission rate of the of the upper state. Plugging Equation A.4 into this gives:

$$N_{h\nu} = A\hat{\sigma}^{(2)}N_0\int_{-\infty}^{\infty}e^{-[(A+Q)t'+\sigma_{pi}\theta]}\int_{-\infty}^{t'}\Phi^2 e^{[(A+Q)t''+\sigma_{pi}\theta-\hat{\sigma}^{(2)}\Omega]}dt''dt' \tag{A.6}$$

In the low laser intensity limit, the ground and upper state are not significantly depleted by the laser radiation. In this case

$$\sigma_{pi} << (A+Q)t \tag{A.7}$$

$$e^{-\hat{\sigma}^{(2)}\Omega} \approx 1 \tag{A.8}$$

Applying these expressions to equation A.6 gives a simplified form.

$$N_{h\nu} = A\hat{\sigma}^{(2)} N_0 \int_{-\infty}^{\infty} e^{-(A+Q)t'} \int_{-\infty}^{t'} \Phi^2 e^{(A+Q)t''} dt'' dt' \tag{A.9}$$

$\Phi(r, z, t)$ represents the photon flux of the laser beam. It is defined in equation A.10.

$$\Phi = \frac{U(r,z)F(t)}{h\nu} \tag{A.10}$$

Where $U(r, z)$ and $F(t)$ are, respectively, the spatial and temporal energy distributions of the laser. They are normalized such that

$$\int_0^{\infty} 2\pi r U(r,z) dr = E(z) \tag{A.11}$$

$$\int_{-\infty}^{\infty} F(t) dt = 1 \tag{A.12}$$

Plugging this definition of Φ into equation A.9 allows for further manipulation of the equation.

$$N_{h\nu} = \frac{A\hat{\sigma}^{(2)} N_0 U^2(r,z)}{(h\nu)^2} \int_{-\infty}^{\infty} e^{-(A+Q)t'} \int_{-\infty}^{t'} F^2(t'') e^{(A+Q)t''} dt'' dt' \tag{A.13}$$

$$N_{h\nu} = \chi \int_{-\infty}^{\infty} e^{-(A+Q)t'} \int_{-\infty}^{t'} F^2(t'') e^{(A+Q)t''} dt'' dt' \tag{A.14}$$

Where χ is used temporarily as a placeholder for the constant term. Assuming that F(t) is a Gaussian of the form

$$F(t) = \frac{1}{\sqrt{2\pi}\sigma_p} e^{-t^2/2\sigma_p^2} \tag{A.15}$$

$$F^2(t) = \frac{1}{2\pi\sigma_p^2} e^{-t^2/\sigma_p^2} \tag{A.16}$$

Plugging equation A.16 into equation A.14 gives

$$N_{h\nu} = \frac{\chi}{2\pi\sigma_p^2} \int_{-\infty}^{\infty} e^{-(A+Q)t'} \int_{-\infty}^{t'} e^{(A+Q)t'' - \frac{t^2}{\sigma_p^2}} dt'' dt' \tag{A.17}$$

For simplicity, temporarily call the inner integral β as shown below.

$$N_{h\nu} = \frac{\chi}{2\pi\sigma_p^2} \int_{-\infty}^{\infty} e^{-(A+Q)t'} \beta dt' \tag{A.18}$$

$$\beta = \int_{-\infty}^{t'} \exp\Big[(A+Q)t'' - \frac{t^2}{\sigma_p^2}\Big] dt'' \tag{A.19}$$

Completing the square in the exponent gives

$$\beta = \int_{-\infty}^{t'} \exp\Big[- \big(\frac{t''}{\sigma_p} - \frac{(A+Q)\sigma_p}{2}\big)^2 + \frac{\sigma_p^2(A+Q)^2}{4}\Big] dt'' \tag{A.20}$$

Using the change of variable $u = \left(\frac{t''}{\sigma_p} - \frac{(A+Q)\sigma_p}{2}\right)$ beta becomes

$$\beta = \sigma_p \exp\Big[\frac{\sigma_p^2(A+Q)^2}{4}\Big] \int_{-\infty}^{(\frac{t''}{\sigma_p} - \frac{(A+Q)\sigma_p}{2})} e^{-u^2} du \tag{A.21}$$

Recognizing the integral term as similar to the error function gives

$$\beta = \sigma_p \exp\Big[\frac{\sigma_p^2(A+Q)^2}{4}\Big] \Big(- \int_0^{-\infty} e^{-u^2} du + \int_0^{(\frac{t''}{\sigma_p} - \frac{(A+Q)\sigma_p}{2})} e^{-u^2} du \Big) \tag{A.22}$$

$$\beta = \sigma_p \frac{\pi^{1/2}}{2} \exp\Big[\frac{\sigma_p^2(A+Q)^2}{4}\Big] \Big(1 + erf\Big[\frac{t''}{\sigma_p} - \frac{(A+Q)\sigma_p}{2}\Big]\Big) \tag{A.23}$$

plugging this back in to equation A.18 gives.

$$N_{h\nu} = \frac{\chi}{2\pi\sigma_p} \frac{\pi^{1/2}}{2} \exp\Big[\frac{\sigma_p^2(A+Q)^2}{4}\Big] \int_{-\infty}^{\infty} e^{-(A+Q)t'} \Big(1 + erf\Big[\frac{t''}{\sigma_p} - \frac{(A+Q)\sigma_p}{2}\Big]\Big) dt' \tag{A.24}$$

$$N_{h\nu} = \frac{A\hat{\sigma}^{(2)} N_0 U^2(r,z)\pi^{1/2}}{4\pi\sigma_p (h\nu)^2} \exp\Big[\frac{\sigma_p^2(A+Q)^2}{4}\Big] \int_{-\infty}^{\infty} e^{-(A+Q)t'} \Big(1 + erf\Big[\frac{t''}{\sigma_p} - \frac{(A+Q)\sigma_p}{2}\Big]\Big) dt' \tag{A.25}$$

Integration over r,z gives an equation for $n_{h\nu}$ the total number of fluorescence

photons emitted.

$$n_{h\nu} = \frac{A\hat{\sigma}^{(2)} N_0 L E^2}{4\pi^{1/2}\sigma_p A_p (h\nu)^2} \exp\left[\frac{\sigma_p^2 (A+Q)^2}{4}\right] \int_{-\infty}^{\infty} e^{-(A+Q)t'} \left(1 + erf\left[\frac{t'}{\sigma_p} - \frac{(A+Q)\sigma_p}{2}\right]\right) dt' \tag{A.26}$$

The measured TALIF signal will be proportional to the number of fluorescence photons emitted.

$$S(\nu) = \frac{\Omega}{4\pi} f_0(T)\phi(\nu) n_{h\nu} (\eta_t q_e \eta_\phi G_p \frac{G_a}{C}) \tag{A.27}$$

Where Ω is the solid angle of the optical collection system, $f_0(T)$ is the equilibrium population fraction of the ground state, and $\phi(\nu)$ is the lineshape in frequency which is determined by various broadening mechanisms. Plugging equation A.26 into this expression gives the full equation for the time integrated TALIF signal $S(\nu)$ assuming that the temporal lineshape of the laser pulse is a Gaussian.

$$S(\nu) = \frac{\Omega}{4\pi} f_0(T)\phi(\nu)(\eta_t q_e \eta_\phi G_p \frac{G_a}{C}) \frac{A\hat{\sigma}^{(2)} N_0 L E^2}{4\pi^{1/2}\sigma_p A_p (h\nu)^2} \exp\left[\frac{\sigma_p^2 (A+Q)^2}{4}\right] ... \\ ... \int_{-\infty}^{\infty} e^{-(A+Q)t'} \left(1 + erf\left[\frac{t'}{\sigma_p} - \frac{(A+Q)\sigma_p}{2}\right]\right) dt' \tag{A.28}$$

If the TALIF signal from general laser pulse shape is desired, Equation A.14 is plugged in to A.27.

$$S(\nu) = \frac{\Omega}{4\pi} f_0(T)\phi(\nu)(\eta_t q_e \eta_\phi G_p \frac{G_a}{C}) \frac{A\hat{\sigma}^{(2)} N_0 L E^2}{A_p (h\nu)^2} \int_{-\infty}^{\infty} e^{-(A+Q)t'} \int_{-\infty}^{t'} F^2(t'') e^{(A+Q)t''} dt'' dt'$$

$$S(\nu) = f(\nu) \int_{-\infty}^{\infty} e^{-(A+Q)t'} \int_{-\infty}^{t'} F^2(t'') e^{(A+Q)t''} dt'' dt' \tag{A.29}$$

Where $f(\nu)$ represents all the terms outside the integral. Because $e^{-(A+Q)t'}$ is not a function of t", it can be moved inside the integral.

$$S(\nu) = f(\nu) \int_{-\infty}^{\infty} \int_{-\infty}^{t'} F^2(t'') e^{-(A+Q)(t'-t'')} dt'' dt' \tag{A.30}$$

This integral represents the signal from fluorescence photons emitted by time t'. t' may be set to infinity for measurements of temperature and number density as only the total signal is needed.

$$S(\nu) = f(\nu) \int_{-\infty}^{\infty} \int_{-\infty}^{\infty} F^2(t'') e^{-(A+Q)(t'-t'')} dt'' dt' \tag{A.31}$$

In this form it is clear that the term inside the integral represents a convolution between the squared laser pulse and the fluorescence response.

$$S(\nu) = f(\nu) \int_{-\infty}^{\infty} F^2(t') * e^{-(A+Q)t'} dt' \tag{A.32}$$

Applying the following property of convolutions.

$$\int_{-\infty}^{\infty} f(t) * g(t) dt = \int_{-\infty}^{\infty} f(t) dt \int_{-\infty}^{\infty} g(t) dt \tag{A.33}$$

Note that this property implies that the integrated area of the fluorescence signal is not dependent on the laser pulse being much shorter than the decay lifetime. Applying this relation to equation A.32

$$\begin{aligned} S(\nu) &= f(\nu) \int_{-\infty}^{\infty} F^2(t) dt \int_{-\infty}^{\infty} H(t) e^{-(A+Q)t} dt \\ S(\nu) &= f(\nu) \frac{1}{(A+Q)} \int_{-\infty}^{\infty} F^2(t) dt \end{aligned} \tag{A.34}$$

Where H(t) denotes the step function, and is included due to the fact that the decay equation represents a response to stimulus. Expanding $f(\nu)$ yields an equation for the time integrated TALIF signal given an arbitrary laser pulse.

$$\boxed{S(\nu) = \frac{\Omega}{4\pi} f_0(T) \phi(\nu) \eta_t q_e \eta_\phi G_p \frac{G_a}{C} \frac{L}{A_p} \frac{\hat{\sigma}^{(2)} N_0 E^2}{(h\nu)^2} \frac{A}{(A+Q)} \int_{-\infty}^{\infty} F^2(t) dt} \tag{A.35}$$

Appendix B

Absolute Number Density Scans and Lifetimes

B.1 Atomic Nitrogen (211 nm) in an Air Plasma

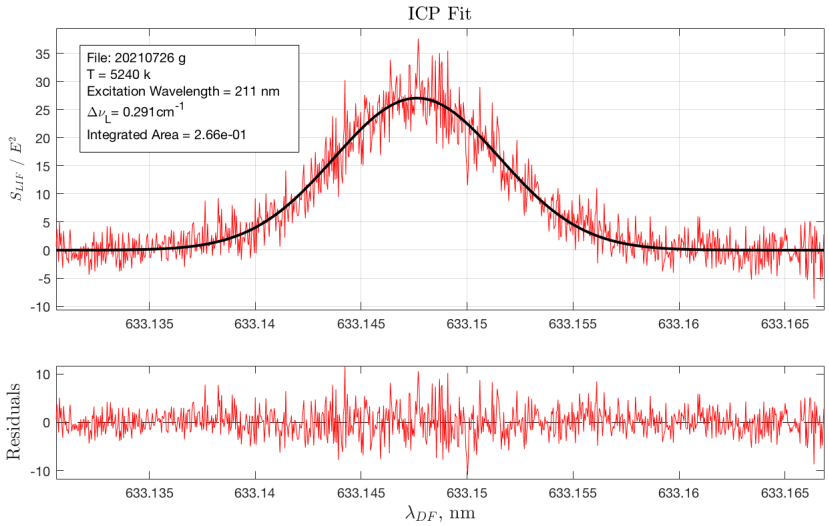

Figure B.1: Fit of N (211 nm) TALIF scan in an air plasma.

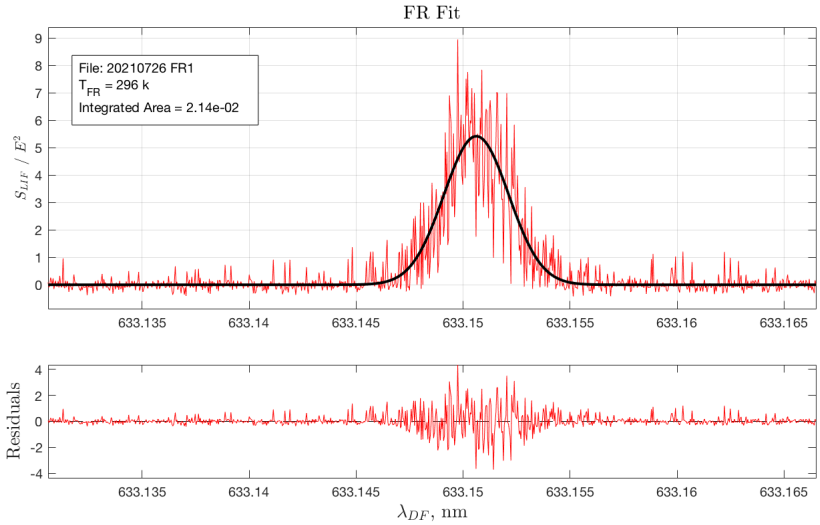

Figure B.2: Calibration Scan of N (211 nm) in the Flow Reactor

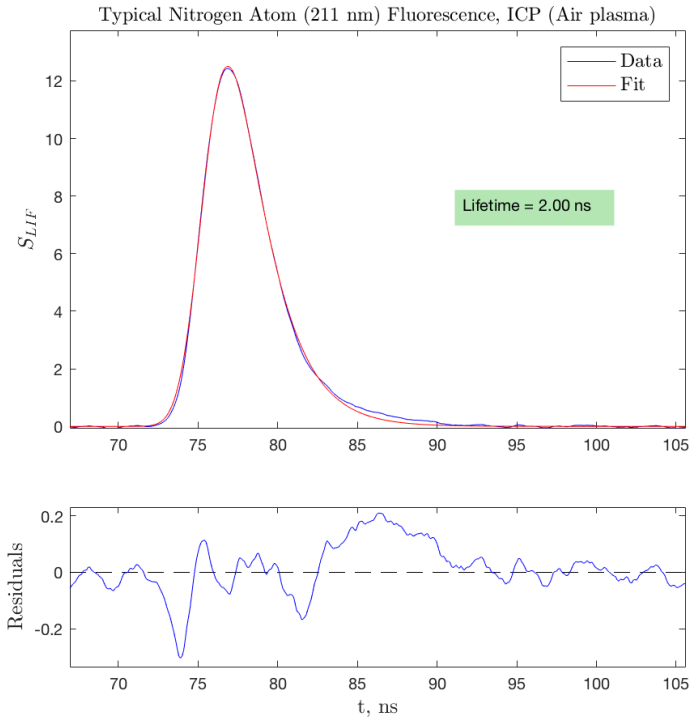

Figure B.3: Example fluorescence trace of atomic nitrogen in the ICP.

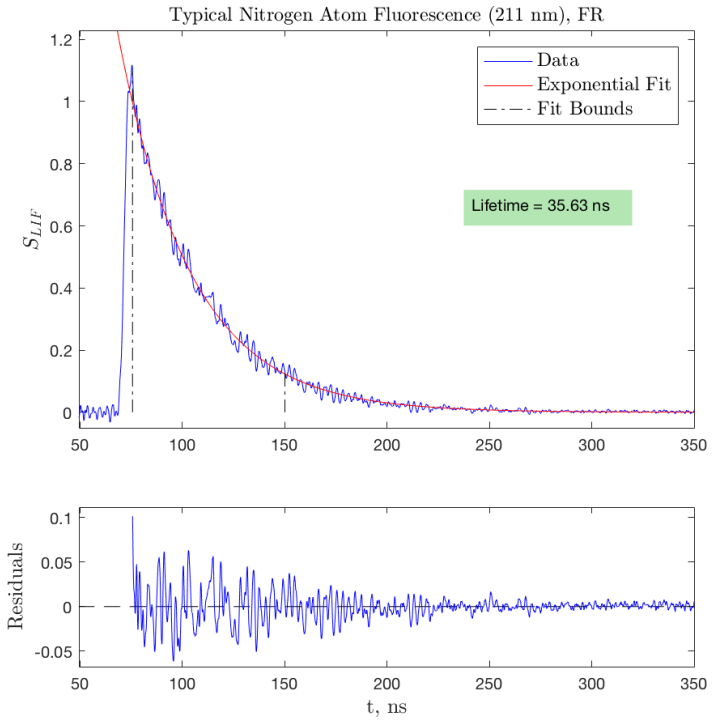

Figure B.4: Example fluorescence trace of atomic nitrogen in the FR.

B.2 Atomic Oxygen (226 nm) in an Air Plasma

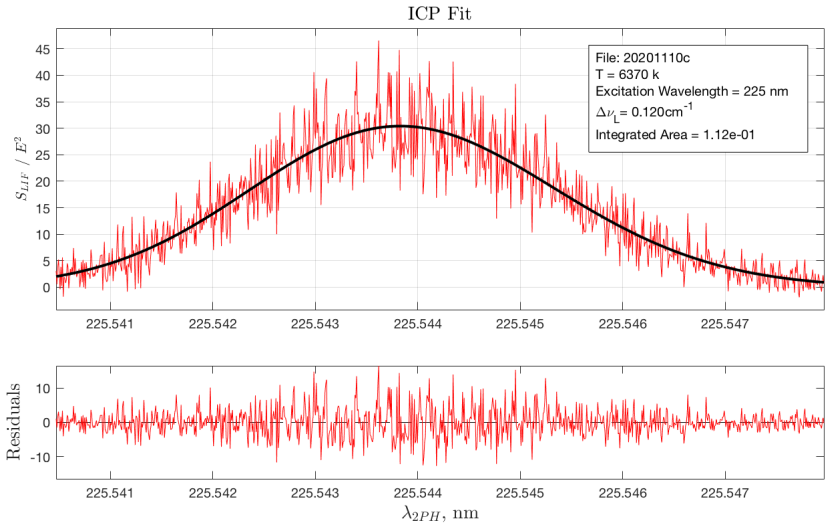

Figure B.5: Fit of atomic oxygen (226 nm) TALIF scan in an air plasma.

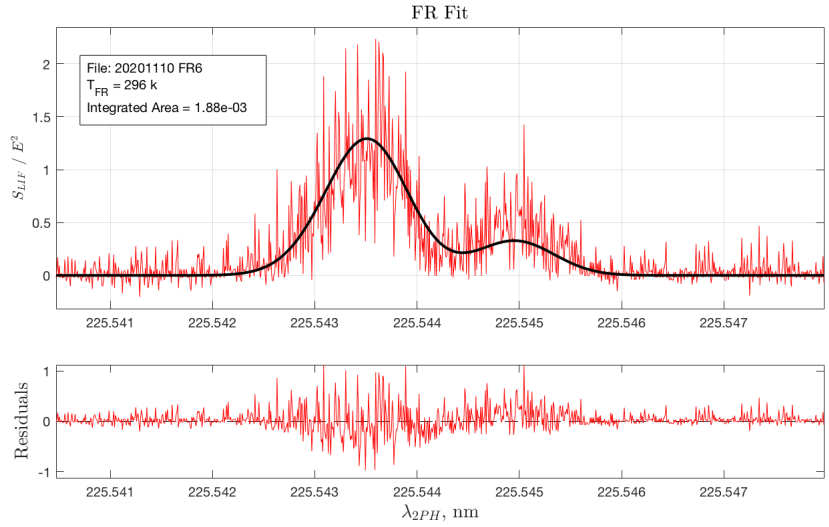

Figure B.6: Calibration scan of atomic oxygen (226 nm) in the flow reactor.

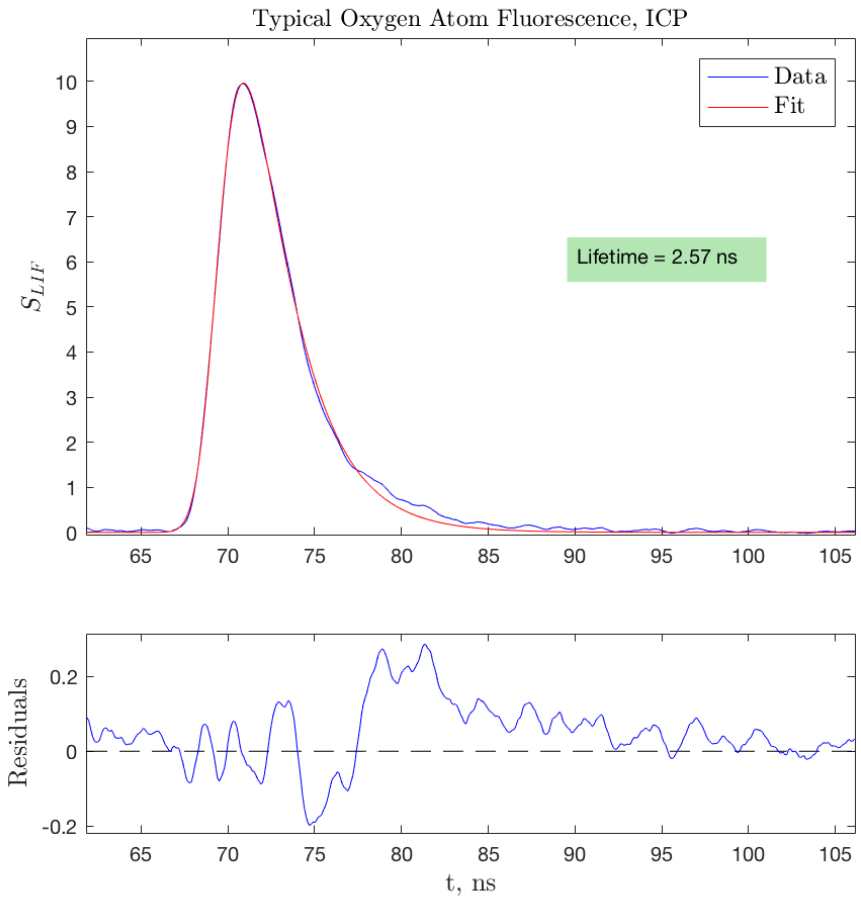

Figure B.7: Example fluorescence trace of atomic oxygen in the ICP.

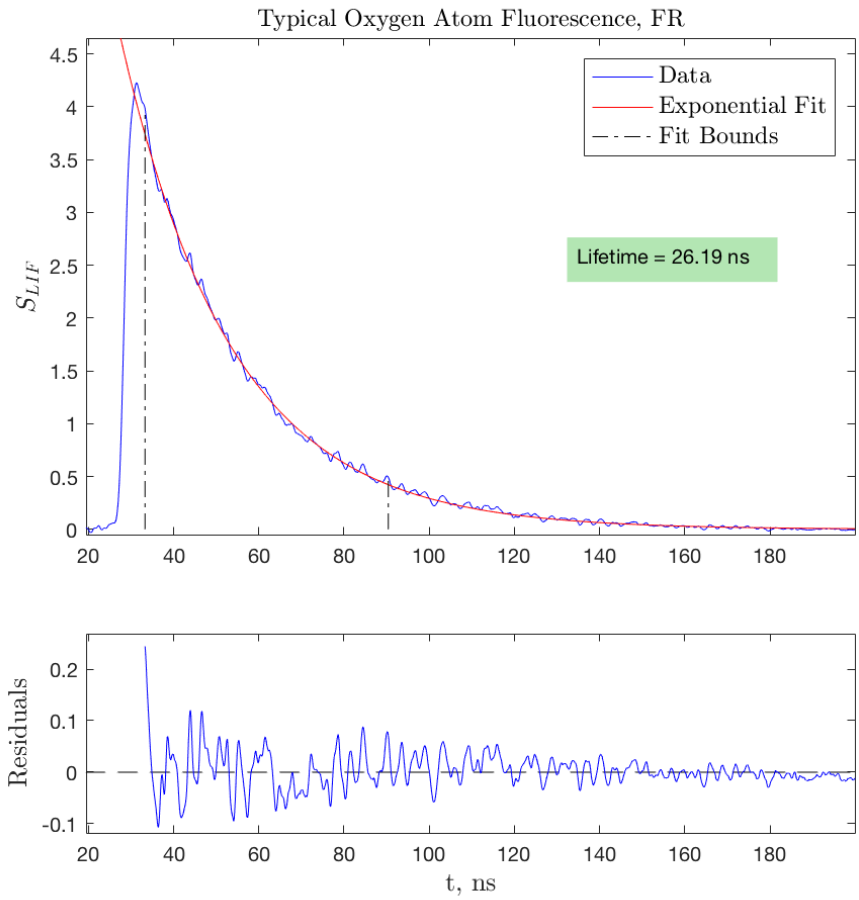

Figure B.8: Example fluorescence trace of atomic oxygen in the ICP.

B.3 Atomic Nitrogen (211 nm) in a Nitrogen Plasma

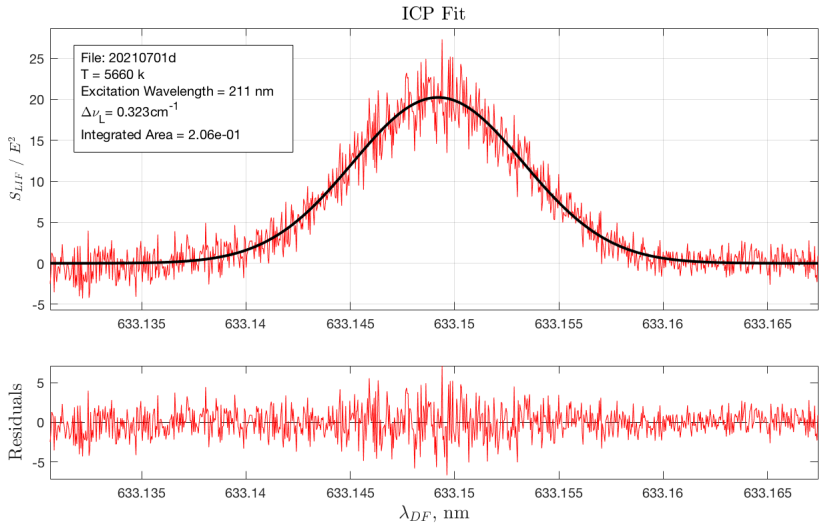

Figure B.9: Fit of N (211 nm) TALIF scan in a nitrogen plasma.

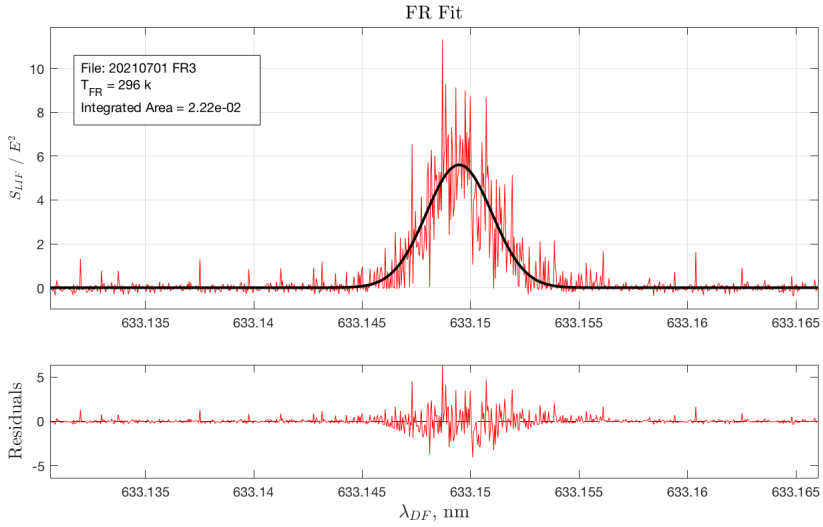

Figure B.10: Calibration Scan of N (211 nm) in the Flow Reactor

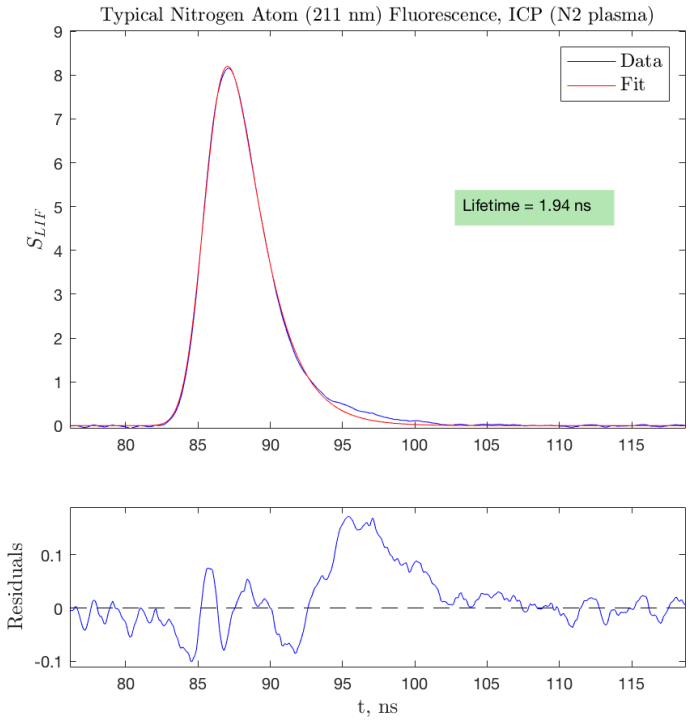

Figure B.11: Example fluorescence trace of atomic nitrogen in the ICP.

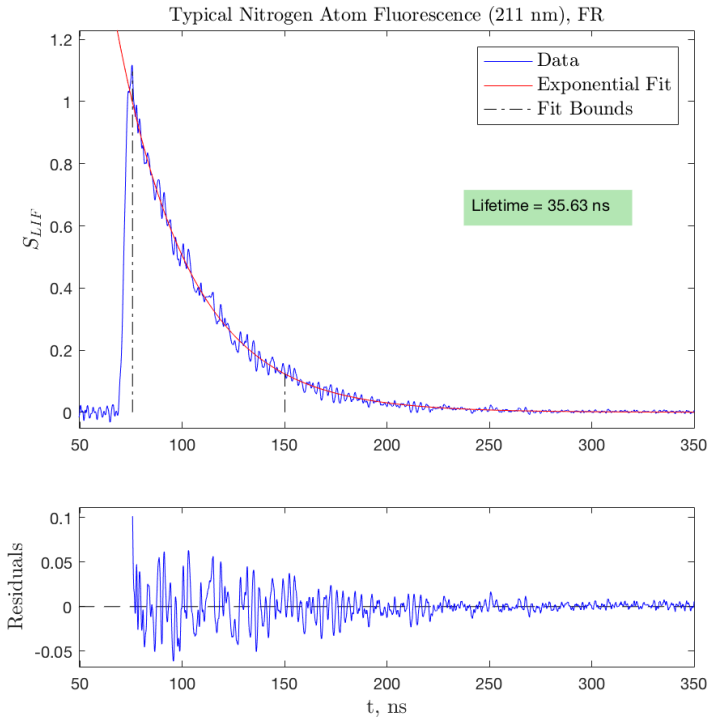

Figure B.12: Example fluorescence trace of atomic nitrogen in the FR.

Appendix C
Photomultiplier Tube Gain

The bulk of this work was done with the R9880 PMT. The bias voltage gain of this PMT is shown in Figure C.1. Figures C.2 and C.3 show the gain characteristics of the R636 PMT, these were used in preliminary work, but not in the final data shown in this thesis.

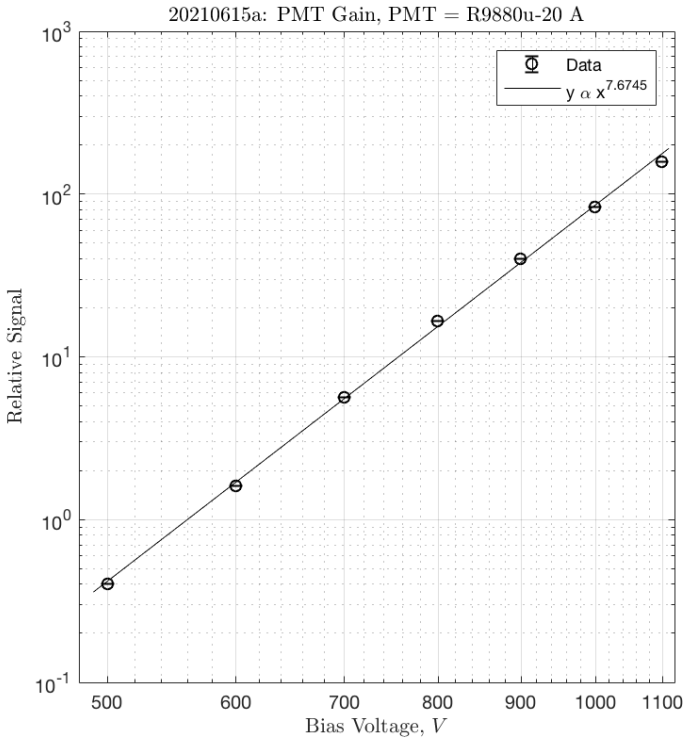

Figure C.1: Curve Fit relating R9880u-20 "A" PMT Bias Voltage to Output Signal

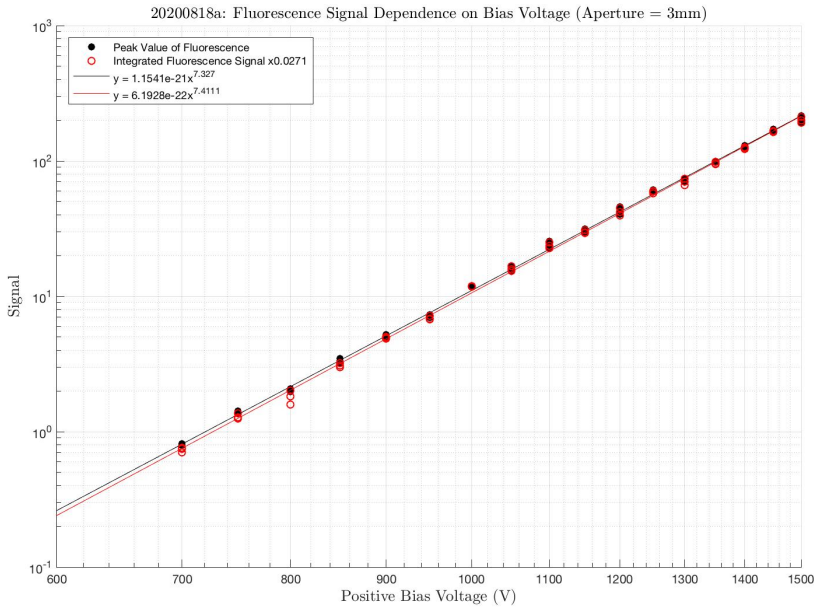

Figure C.2: Curve Fit relating R636 PMT Bias Voltage to Output Signal

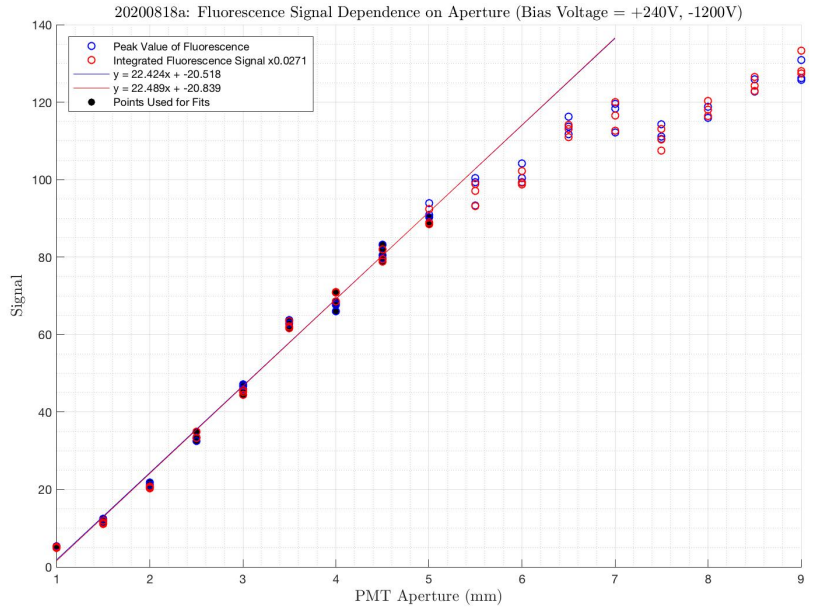

Figure C.3: Curve Fit relating R636 PMT Aperture to Output Signal

Appendix D

Numerical Study of Lifetime Fitting Techniques

D.1 Lifetime Fitting Techniques

Goal: Determine the scale of error from the various lifetime fitting techniques.
Method:

1. Take temporal measurements of the laser pulse $F(t)$ with the Bi-Planar Phototube (BPPT).

2. Create artificial fluorescence data by numerical convolution.
fluorescence(τ) = $F(t)^2 * e^{-t/\tau}$*(PMT Response)

3. For various values of τ fit the fluorescence, and show the trend in error for each fitting technique.

Results:
Figure D.1 shows the result of this study. GEC is short for Gaussian-exponential convolution. Above a set lifetime of around 15 ns, all fitting methods gave a less than 1% error in the output lifetime. The exponential and GEC fits are fairly stable, however, the GEC fit with PMT response seems to be able to fall into different stable modes (fit peak below data peak vs fit peak above data peak), but as long as the fit line looks like it is matching the data well, these results should hold as a first order approximation of the error. Note that the sharp spike in the error of the PMT response fit around 1 ns corresponds to when the lifetime is equal to the PMT response constant δ as described in section 4.2. Figure D.2 shows a comparison of the results from the numerical study to data collected in the ICP. The data seem to follow the same trend as the study, although the lifetime when the exponential fit is equivalent

to the GEC fit seems to be closer to 2 ns in contrast to the crossing at 2.5 ns in the study.

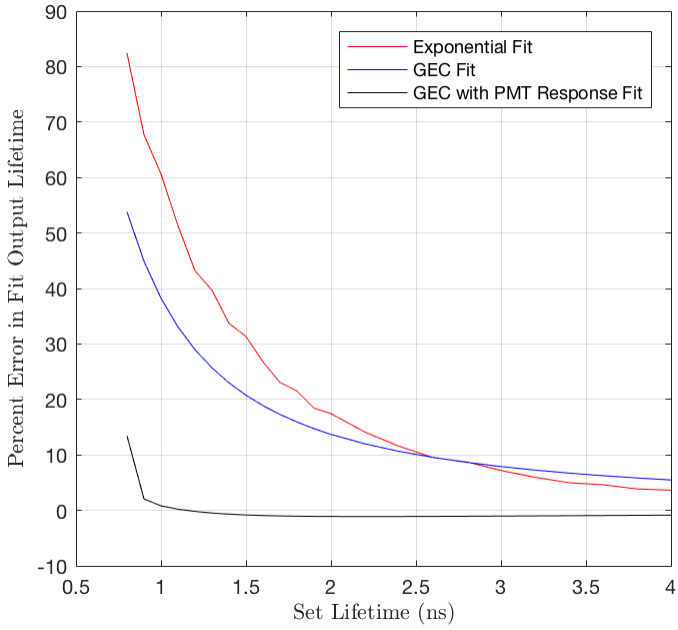

Figure D.1: Percent Error in output lifetime for various fitting methods.

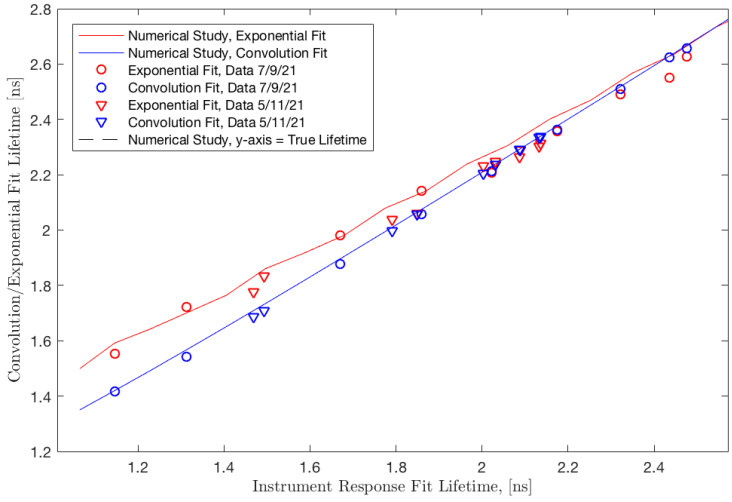

Figure D.2: Comparison of study results to data

D.2 Laser Pulse Jitter

Goal: Determine the scale of error from averaging fluorescence signals based on temporal jitter of the laser pulse.
Method:

1. Create a model of laser pulse jitter seen in our facility
2. Model TALIF signal as a numerical convolution of a squared Gaussian laser pulse with an exponential decay
3. Average a number of modeled TALIF signals with the jitter distribution determined in step 1
4. Fit these averaged signals and examine the effect on the resulting fit.

Results:

- A series of 2172 laser pulse measurements were recorded with a bi-planar phototube
- Sloping base line subtraction performed on BPPT data
- The "start time" of the laser pulse was determined by interpolating for the time when the laser pulse signal reached 0.5 of its maximum value (changing this between 0.25-0.75 of the max did not significantly affect the results)
- This value was compiled for all 2172 laser pulse traces, and a skewed normal distribution was used to model the jitter distribution. see Figure D.3

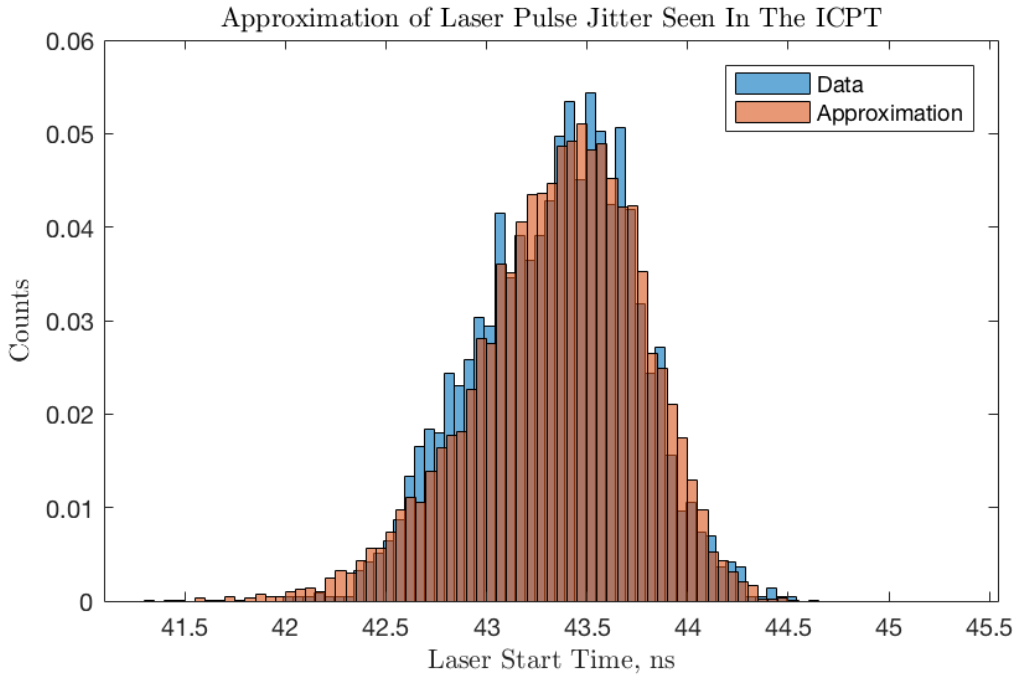

Figure D.3: Comparison of measured laser pulse jitter compared to the model used in this study

Below are a series of figures showing the effect of typical jitter on averaged lifetime measurements using both an exponential and Gaussian-exponential convolution (GEC) fit. The exponential fit is largely unaffected by jitter in the laser pulse. This is likely because the main effect of jitter is to widen the apparent laser pulse width. The GEC fit is a bit more complicated. When using the GEC fit, one can choose to let the fit determine the laser pulse width as a part of the least squares fitting process, or the value can be fixed as the "true" measured pulse width. In the FR this decision does not really matter as neither method has significant error.

Long lifetimes seen in the FR are easy to fit, and there seems to be no reason not to use a simple exponential fit. On the other hand, using an exponential fit on a 2 ns ICP lifetime (using our ns laser system, and excluding noise and jitter) will result in a measured lifetime of 2.22 ns (Figure D.7). This is an 11% error even in the ideal case! If possible we would like to avoid this. The GEC fit is able to discern these short lifetimes, however, when the pulsewidth is fixed in the GEC fit, it will see a 1-5% error when jitter is added to the laser pulse(Figure D.7). By letting the pulsewidth be a free fit parameter (Figure D.6) it seems the GEC fit is able to account the effect of jitter. But this may not be the case once the assumption of a Gaussian laser pulse is dropped, So we must tread carefully.

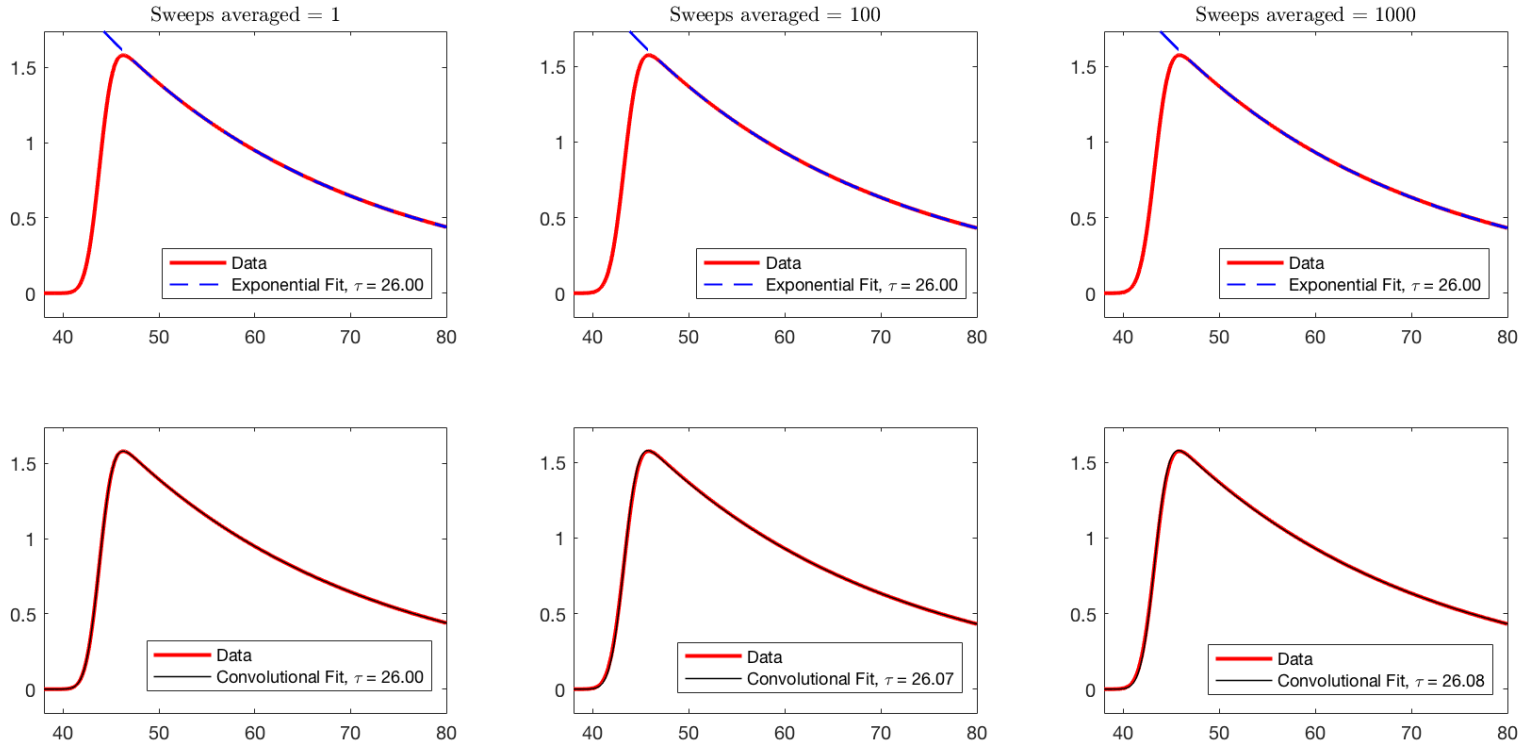

Figure D.4: True lifetime = 26 ns. typical FR lifetime for atomic Oxygen. In this case the laser pulse width parameter was fixed in the G-E convolution fit.

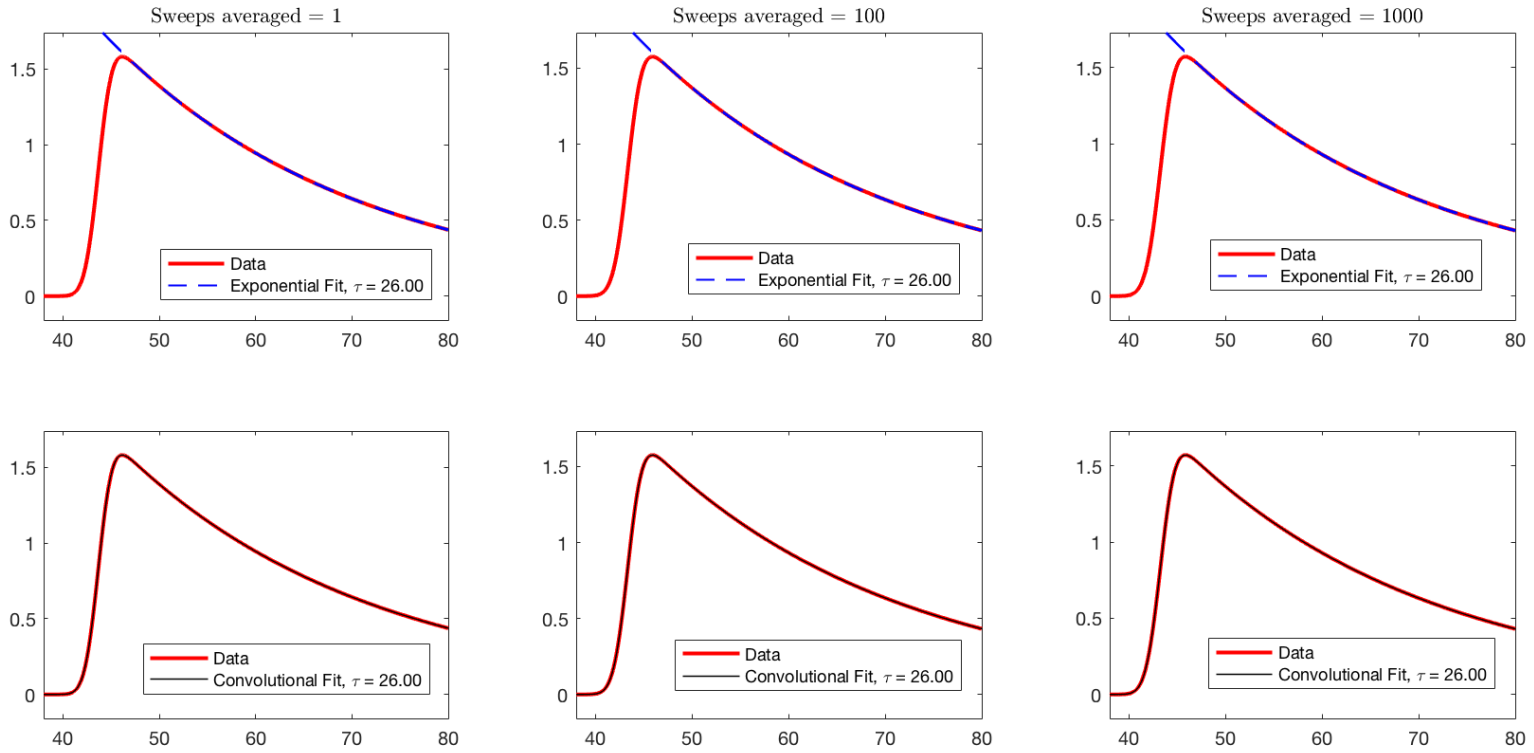

Figure D.5: True lifetime = 26 ns. typical FR lifetime for atomic Oxygen. In this case the laser pulse width was a free parameter in the G-E convolution fit.

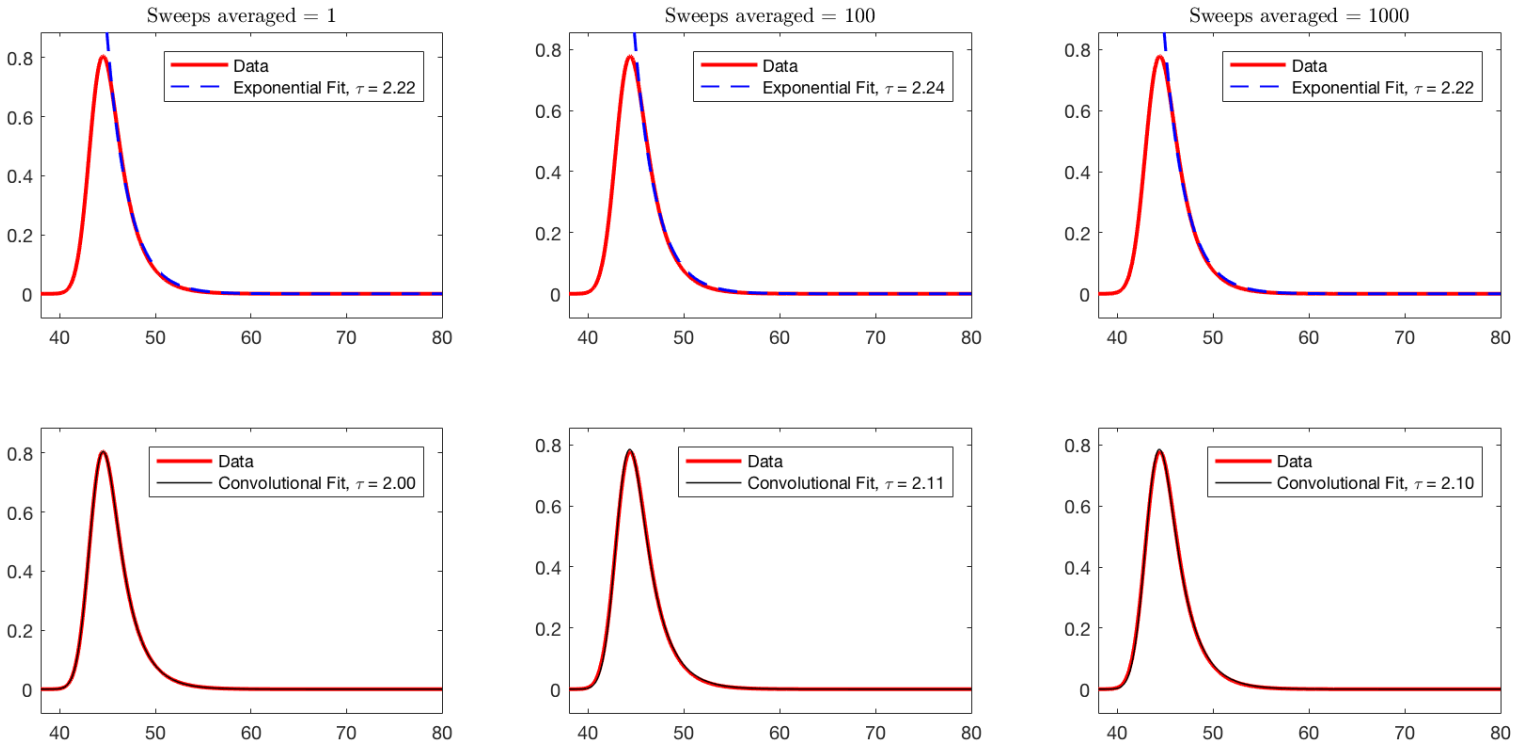

Figure D.6: True lifetime = 2 ns. typical ICP lifetime. In this case the laser pulse width was a free parameter in the G-E convolution fit.

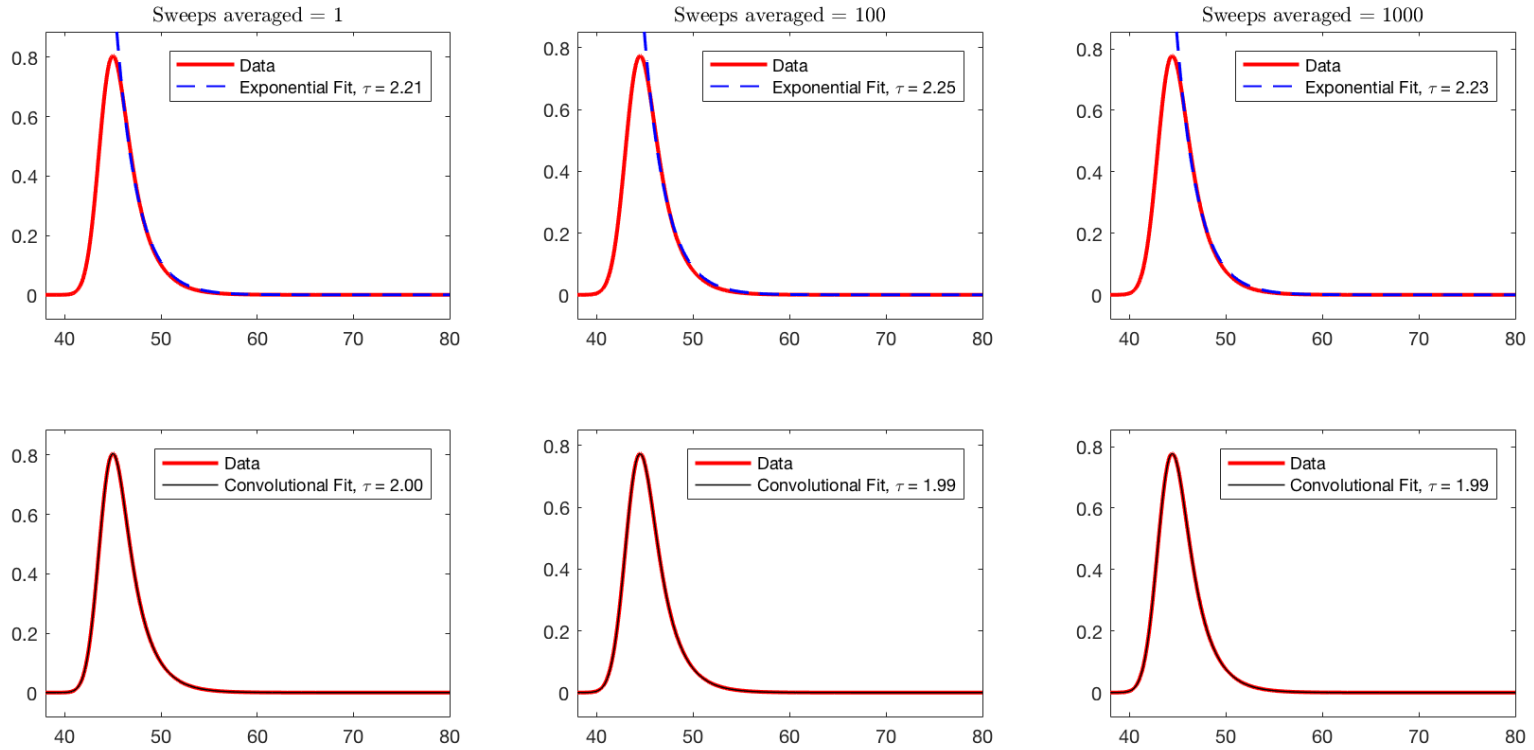

Figure D.7: True lifetime = 2 ns. typical ICP lifetime. In this case the laser pulse width was a free parameter in the G-E convolution fit.

Appendix E

Lifetime Variation with Excitation Wavelength

The observed lifetime of all LIF transitions used in this work appear to be lower in the wings of the signal compared to the center. Further work is needed to definitively say if this is a physical phenomenon or an artifact of the measurement technique. In this section I will layout what we have found so far.

The lifetime variation is seen in the ICP in TALIF of nitrogen atoms at both 211 nm, and 207 nm, oxygen atom at 226 nm, as well as LIF measurements in the NO(A-X) band. These results are shown in the figures below.

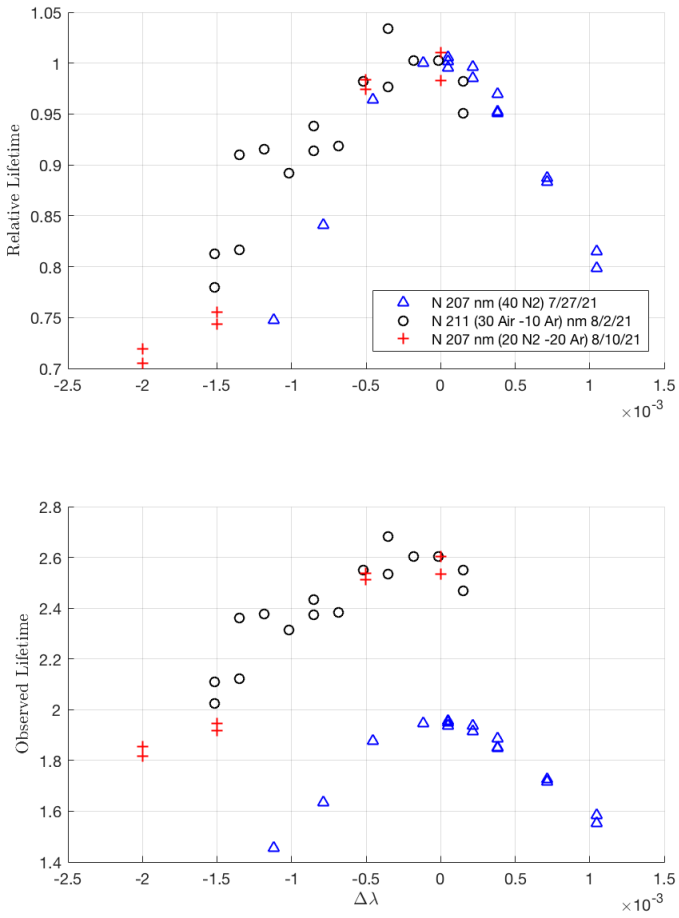

Figure E.1: Lifetime variation in atomic nitrogen (ICP, R9880).

Atomic species were all showing similar amounts of lifetime variation across the transition, So we performed the same test with nitric oxide in the ICP. This time using both the R9880 and R636 PMTs. Temperature scans with both PMTs returned the same temperature within the standard deviations of the measurements. The data in Figures E.3 and E.4 show the result of these tests.

The R9880 PMT showed a similar trend to the atomic species. The R636 gave a somewhat ambiguous result which may be seen either as a similar downward trend,

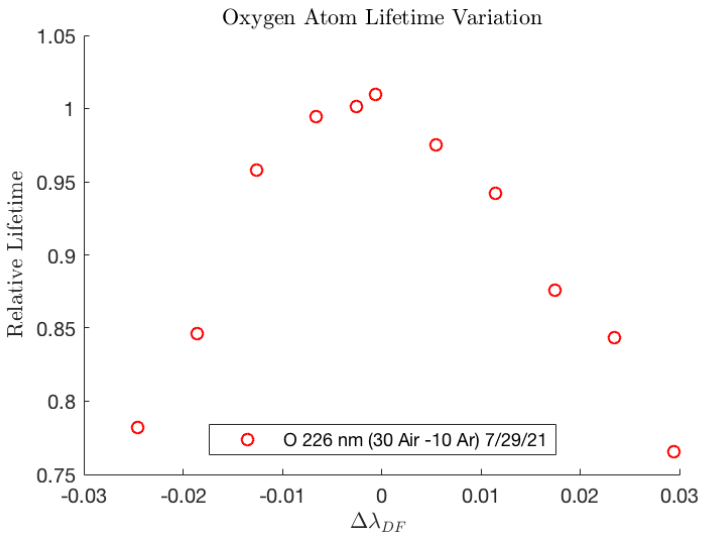

Figure E.2: Lifetime variation in atomic oxygen (ICP, R9880).

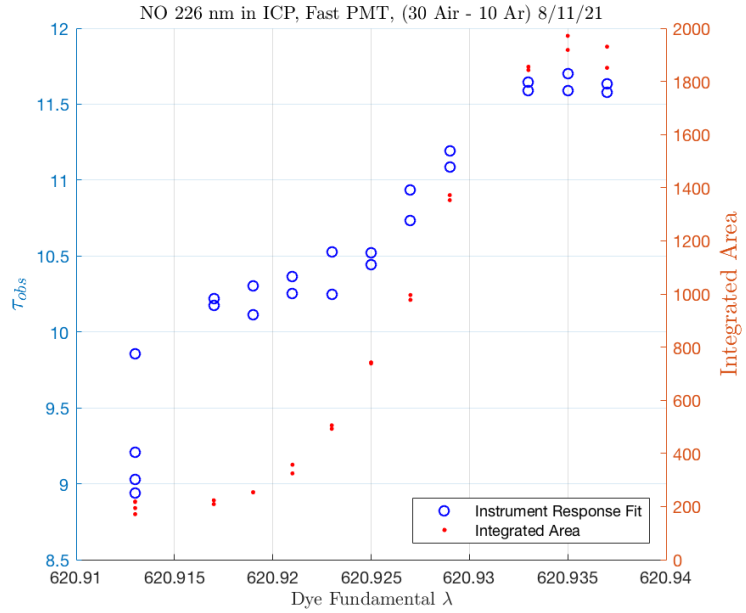

Figure E.3: Lifetime variation in NO (ICP, R9880).

or a very noisy constant value. Increasing the number of averages reduced the spread of lifetimes measured at each wavelength, however, it did not raise the mean value of

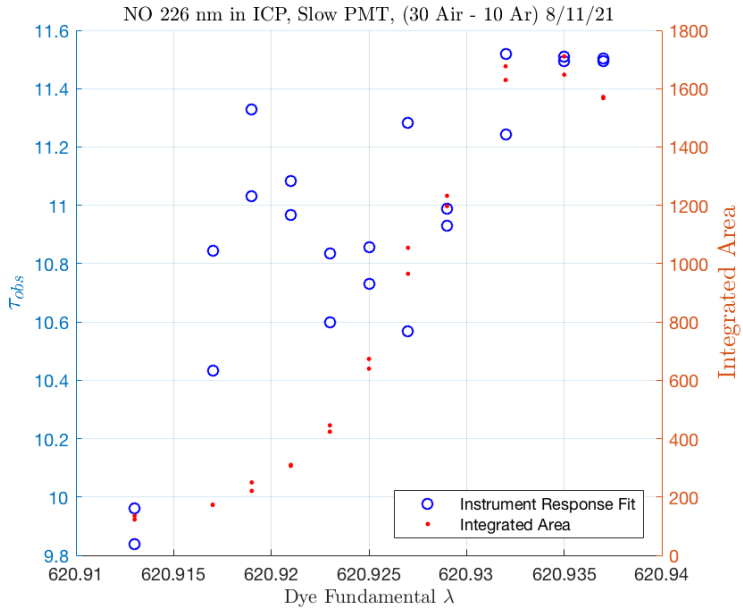

Figure E.4: Lifetime variation in atomic oxygen (ICP, R636).

the lifetime. So random noise does not seem to be causing this effect. However, it is possible either the PMTs dark current, or a continuous background emission from the plasma is causing this effect.

If we assume that the R636 did not see a downward trend of observed lifetime, that would suggest this is simply an artifact of the faster PMT. Perhaps since it is not gated, it is being affected by continuous background emission from the plasma which somehow has the effect of returning a lower lifetime when the LIF signal is lower.

If we assume that the R636 does agree with the R9880, that suggests that either there is a physical process which tends to shorten the observed lifetimes in the wings. Or both of these PMTs inherently will give a lower lifetime measurement when the signal level is lower.

Example fluorescence traces measured by the R9880 PMT are given in Figures E.5 and E.6, These correspond to the line-center of the transition, and halfway through the wing of the transition respectively.

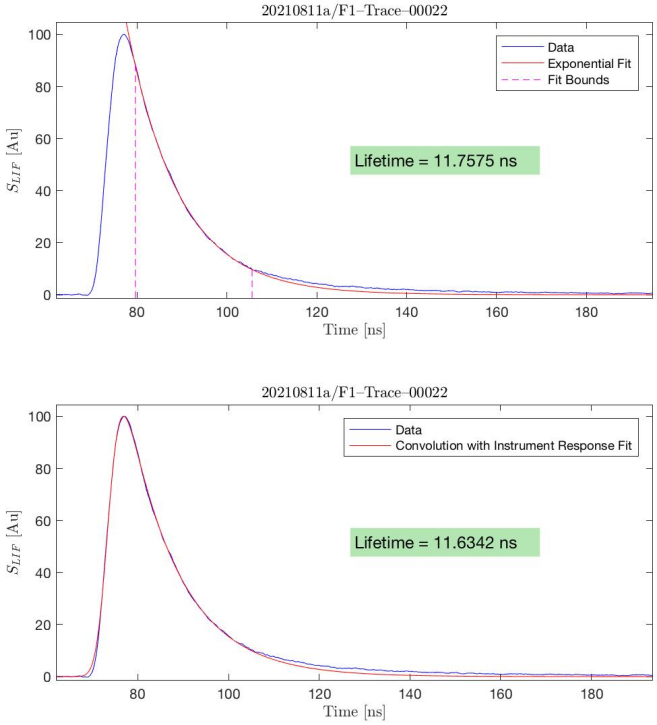

Figure E.5: NO lifetime trace from the transition line-center. $\lambda_D L = 620.937$ *nm*

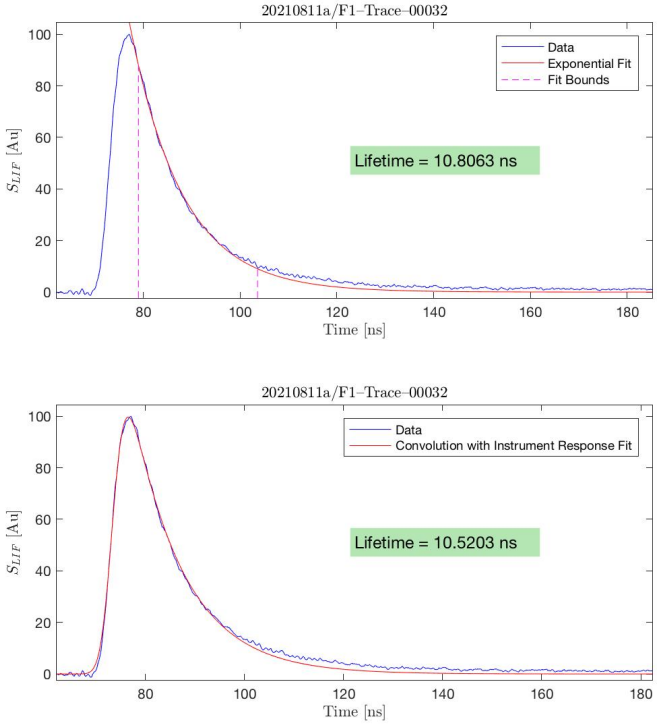

Figure E.6: NO lifetime trace from the wing of the transition. $\lambda_D L = 620.925$ *nm*

Summary:

- Lifetimes seem to decrease by $\approx 20\%$ in the wings of the signal for all probed species in the ICP when measured with the R9880 PMT.
- ICP measurements of NO with the R636 PMT were inconclusive
- NO lifetimes in the FR (19 torr) showed a 1.5% drop of lifetime values in the wings with the R9880, and no drop with the R636. This 1.5% drop was able to be recreated at the linecenter by decreasing the overall signal and increasing the bias voltage.
- The number of sweep averages does not significantly effect the output lifetime, so random noise is unlikely to be the cause.
- Unlike the R636, the R9880 is not gated, so perhaps the lifetime variation has something to do with a (time) continuous background signal.

Whether this variation of lifetime in the wings is caused by a physical phenomenon or is an artifact of the measurement technique, it represents a lack of understanding, and may be a cause of systematic error in LIF measurements of lifetime, temperature and number density.

Appendix F

Measurement Techniques

The techniques described below are both meant to serve as a guide for future people in the lab, and to provide a record of the techniques used such that any blunders of reasoning, if present, may be more easily identified.

F.1 Beam Area

We need to know the beam area in the LIF probe volume, but the laser energy is far too high to simply put the Spirocon sensor at the probe location and measure the width. To get around this, the Spirocon measures a reflection of the beam from a fused silica flat (only $\approx 4\%$ power is reflected, and the camera still requires neutral density filters!). However, the change in index of refraction at the ICP/FR window moves the focal point of the laser beam (Figure F.1), so putting the spirocon at the correct location requires some thinking.

To align the sensor, we chose to measure the distance from the focal point to the collection volume and set up the Spirocon the same distance away from the focal point of the reflected beam.

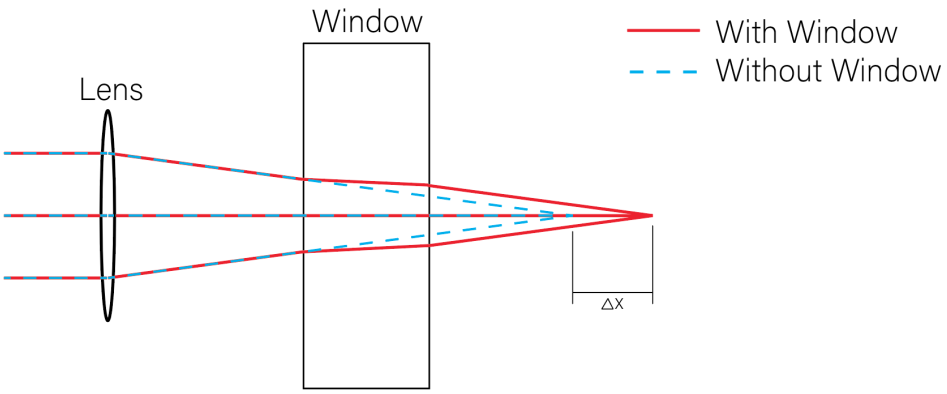

Figure F.1: Focal point moves due to change in index of refraction of the window.

Steps:

- Find the transition of interest in the FR to verify the laser wavelength
- Find the focal point of the laser by multiple of the following methods to gain confidence in the measurement:
  - At 2 known locations on either side of the focal point, measure the beam diameter. Use this to calculate where the focal point is.
  - Put an index card on a translation stage. Visually locate the focal point. Placing a neutral density filter UPSTREAM of the lens may make this easier.
  - Using a microphone, find the focal point by translating the card until the laser clicking is loudest.
- Measure the distance from the focal point to the PMT viewing location with calipers.
- Use a clean flat window to reflect the beam just downstream of the lens.
- Locate the focal point of the reflected beam.

- Place the sensor such that the distance from the CCD to the reflected focal point is equal to the previously measured distance from the PMT viewing location to the focal point. (This is easiest with a translation stage.)
- See Brandon Voll's notes on the BeamGage Software.

Things to watch out for:

- Using two ND filters on the camera itself will cause beam reflections in the image. If you need to use 2 filters, place one further upstream to avoid reflections.
- Recording single laser pulses will prevent errors that arise from averaging pulses of a time varying beam.
- There are pixels in the camera that have lost sensitivity and appear either fully on or off. avoid them when possible.

F.2 PMT Gain

- This test is quite simple, To start ensure that the FR and Laser/boxcars are warmed up, and locate a TALIF/LIF transition in the FR.
- Record a full scan of the transition at each bias voltage.
- As nothing is varying in this setup aside from the PMT gain, the PMT gain can be directly extracted from the integrated areas of the scans.
- Full sweeps are necessary to ensure there is no effect from dye laser drift.

To measure the PMT gain across a wide range of bias voltages, the PMT aperture will need to be adjusted. I suggest starting at the highest bias voltage/lowest aperture to ensure that the PMT is well aligned (vertically) with the laser beam. As you

decrease the bias voltage, the signal will get very small. At this point record a scan with the current aperture, then open the aperture until you see a sufficient signal, and record another scan at the same bias voltage. This will allow you to account for the difference in signal caused by the change in aperture.

Measurements of the PMT gain at various fluorescence wavelengths seem to give the same scaling, so the transition used should not matter.

F.3 Titration

- if the FR base pressure can't get to 0.015 torr, check for leaks. (Check where the glass connects to the plastic tubing for cracks)
- Make sure the Nitric Oxide line is evacuated to base pressure before opening the NO bottle or starting the FR. (Air/Nitrogen in the line will affect the titration)
- Let the FR warm up for at least 2 hrs before doing calibration scans and titrations.
- Avoid hysteresis caused by dye laser drift by taking a full scan of the transition at each titration level.

F.4 Lifetime Measurements

- Use the shortest possible cable. if using R9880U-20, only use the attached cord. adding an additional short cord will result in a signal reflection.
- Any time you add a connector to the path there will be a signal reflection off of the change in impedance.
- Use a sufficient number of averages so that the signal appears smooth.

F.5 Absolute Number Density

For each test, be sure to record the conditions:

- FR & ICP base pressure
- FR & ICP working pressure
- FR & ICP gas flow rates and their zero offsets
- Which PMTs are being used?
- What dye laser wavelength corresponds to the transition of interest?
- ICP current output (i.e. 2.5 A)
- FR microwave discharge power
- FR static temperature
- What is the distance from the focal point to the collection volume in the ICP? (for beam area)

In addition, it is important to monitor the laser energy:

- record the 532 nm energy
- record the dye laser energy
- note the Q-switch delay and dye wavelength.

For each number density scan write down:

- filename
- FR (aperture, bias voltage, gate width/sensitivity)
- ICP (aperture, bias voltage, gate width/sensitivity)
- Laser delivery aperture
- Was background subtraction used?

- Was a pre-amplifier used?
- If probing multiple transitions, which one are you using?

Things to keep in mind:

- Careful PMT alignment is crucial to a good number density measurement. Since the signal will likely be very small at the FR this can be tricky. I suggest using the pre-amplifier to increase the signal during alignment. Also, running and monitoring the SR272 program during alignment can be helpful as it will allow you to see the trend of the signal as you adjust the height.
- Verify that the PMT aperture is larger than the diameter of the laser beam. Otherwise, the measured beam area and laser energy will be incorrect.
- Gate Width. Become familiar with how to adjust the cursors on each oscilloscope. This will allow you to easily measure the gate width.
- PMT Aperture. If the experiment will allow, use the built in set screw to lock the aperture in place once you have good signal. That way you do not have to worry about whether you bumped it during your test. If necessary you should be able to adjust the signal level by adjusting only the bias voltage.
- While we are confident that the conditions in the FR are consistent day to day for the same temperature, pressure and microwave power. It is best to perform 1-2 titrations immediately after the number density test in order to confirm this
- If you are using background subtraction in the torch be sure to adjust the background gate to be the same length as the ICP gate. AND zero all the signals prior to running a scan.
- Remove vertical offset from the fit. The signal is already being zeroed to the shutter.

Appendix G
Beam Calculations

G.1 Centroid of a Clipped Gaussian Beam

Goal: Develop a series of equations which relate the centroid of a clipped Gaussian laser beam to the fractional laser energy which it holds.

Results:

These results rely on the assumption that the laser beam is well approximated as a Gaussian as is the case for small beam delivery apertures. An assumption is also made that the sample does not significantly reflect the laser light (graphite sample). In order to make use of data with a clipped beam the variation of the beam area must also be taken into account. As such the following calculations may or may not ever be useful.

A spatially Gaussian beam with amplitude G_0 and $1/e^2$ width equal to w is given by equation G.1.

$$G(x_1, x_2) = G_0 \exp\Big[- \frac{2}{w^2}(x_1^2 + x_2^2)\Big] \tag{G.1}$$

We define $\epsilon(a, \alpha)$ for later use.

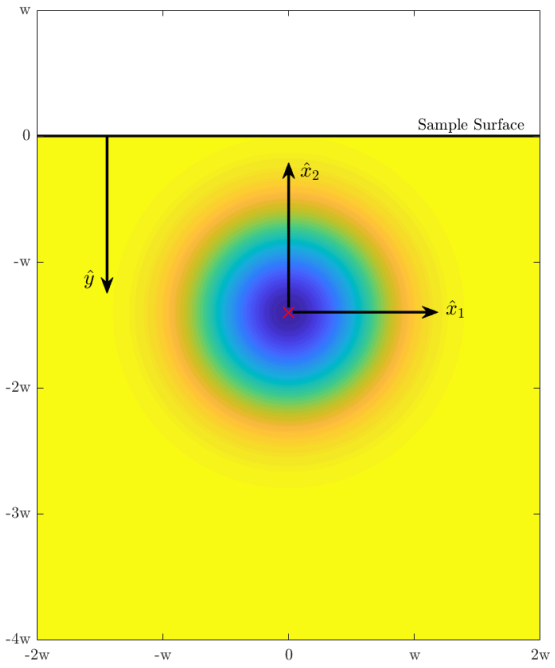

(a) Coordinate systems used in this calculation.

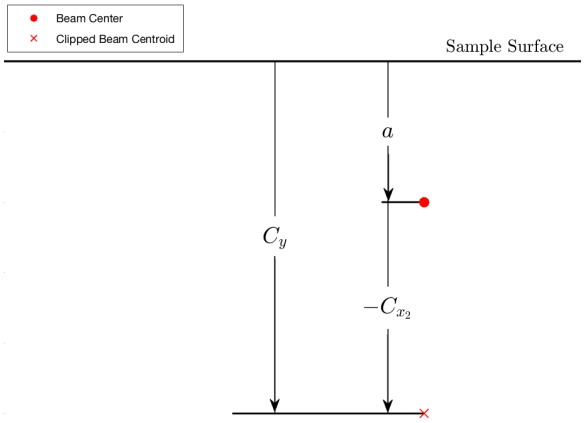

(b) a is the distance from the sample to the beam center. C_y is the distance from the sample to the centroid. C_{x_2} is the distance from the beam center to the centroid. a and C_y are given signs coore-sponding to the $\hat{y}$ coordinate system. Whereas C_{x_2} uses the $\hat{x}_2$ coordinate system.

$$\epsilon(a,\alpha) = \int_{-\infty}^{a}\int_{-\infty}^{\infty} G(x_1,x_2)^{\alpha} dx_1 dx_2 \tag{G.2}$$

$$\epsilon(a,\alpha) = \frac{G_0 w^2 \pi}{4\alpha}\left[erf\left(\frac{a\sqrt{2\alpha}}{w}\right)\right] \tag{G.3}$$

Where α is the exponent that the laser intensity is raised to. For example, in TALIF, the signal is proportional to the energy squared, ($\alpha = 2$) The un-clipped laser energy is given by $\epsilon(a,1)$, and The fractional laser power $F(a)$ of a clipped laser pulse is then given by:

$$\boxed{F(a) = \frac{\epsilon(a,1)}{\epsilon(\infty,1)} = \frac{1}{2}\left[1 + erf\left(\frac{a\sqrt{2}}{w}\right)\right]} \tag{G.4}$$

The distance between the center of the beam and the clipped beam centroid C_{x_2}

is given by:

$$C_{x_2}(a,\alpha) = \frac{\int_{-\infty}^{a}\int_{-\infty}^{\infty} x_2 G(x_1,x_2)^{\alpha} dx_1 dx_2}{\int_{-\infty}^{a}\int_{-\infty}^{\infty} G(x_1,x_2)^{\alpha} dx_1 dx_2} \tag{G.5}$$

$$C_{x_2}(a,\alpha) = \frac{\int_{-\infty}^{a}\int_{-\infty}^{\infty} x_2 G(x_1,x_2)^{\alpha} dx_1 dx_2}{\epsilon(a,\alpha)} \tag{G.6}$$

$$\boxed{C_{x_2}(a,\alpha) = -\frac{w}{\sqrt{2\pi\alpha}} \frac{\exp\left(\frac{-2\alpha a^2}{w^2}\right)}{1+erf\left(\frac{a\sqrt{2\alpha}}{w}\right)}} \tag{G.7}$$

The distance from the surface of the sample to the centroid of the clipped beam C_y is given by:

$$\boxed{C_y(a,\alpha) = a - C_{x_2} = a + \frac{w}{\sqrt{2\pi\alpha}} \frac{\exp\left(\frac{-2\alpha a^2}{w^2}\right)}{1+erf\left(\frac{a\sqrt{2\alpha}}{w}\right)}} \tag{G.8}$$

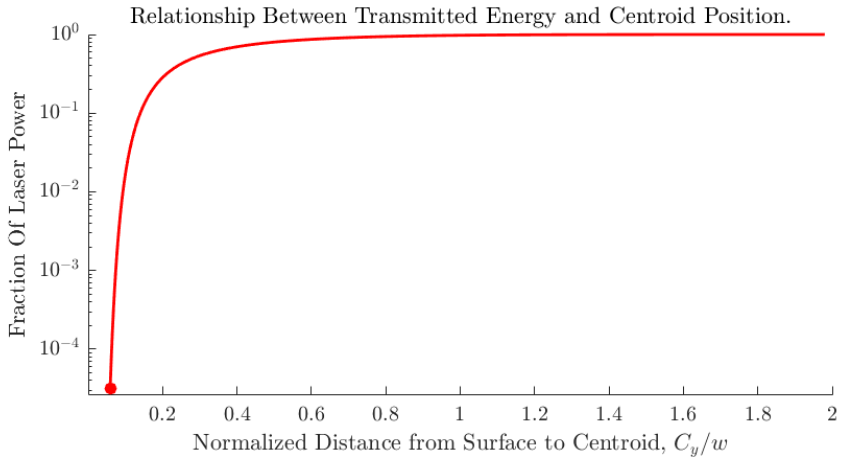

Figure G.2: $\alpha = 2$ (TALIF signal). The centroid of the laser pulse approaches the sample surface as the fractional power goes to zero.

Below I show how I solved for $\epsilon(a,\alpha)$ and $\int_{-\infty}^{a}\int_{-\infty}^{\infty} x_2 G(x_1,x_2)^{\alpha} dx_1 dx_2$.

Solving for: $\epsilon(a, \alpha)$

$$\epsilon(a,\alpha) = \int_{-\infty}^{a}\int_{-\infty}^{\infty} G(x_1,x_2)^{\alpha} dx_1 dx_2 \tag{G.9}$$

$$G(x_1,x_2)^{\alpha} = G_0 \exp\Big[-\frac{2\alpha}{w^2}(x_1^2+x_2^2)\Big] \tag{G.10}$$

$$\epsilon(a,\alpha) = G_0\int_{-\infty}^{a}\int_{-\infty}^{\infty} \exp\Big[-\frac{2\alpha}{w^2}(x_1^2+x_2^2)\Big] dx_1 dx_2 \tag{G.11}$$

Change of variable with the following substitution:

$$u = \frac{x_1\sqrt{2\alpha}}{w} \tag{G.12}$$

$$v = \frac{x_2\sqrt{2\alpha}}{w} \tag{G.13}$$

$$\epsilon(a,\alpha) = \frac{G_0 w^2}{2\alpha}\int_{-\infty}^{a}\sqrt{2\alpha}/w \int_{-\infty}^{\infty} e^{-u^2}e^{-v^2} du dv \tag{G.14}$$

Using the definition of the error function gives:

$$\epsilon(a,\alpha) = \frac{G_0 w^2\pi}{8\alpha}\Big[1+erf\Big(\frac{a\sqrt{2\alpha}}{w}\Big)\Big]\Big[1+erf\Big(\infty\Big)\Big] \tag{G.15}$$

$$\boxed{\epsilon(a,\alpha) = \frac{G_0 w^2\pi}{4\alpha}\Big[1+erf\Big(\frac{a\sqrt{2\alpha}}{w}\Big)\Big]} \tag{G.16}$$

Solving for: $\int_{-\infty}^{a}\int_{-\infty}^{\infty} x_2 G(x_1,x_2)^{\alpha} dx_1 dx_2$

$$\int_{-\infty}^{a}\int_{-\infty}^{\infty} x_2 G(x_1,x_2)^{\alpha} dx_1 dx_2 = \tag{G.17}$$

$$= G_0 \int_{-\infty}^{a}\int_{-\infty}^{\infty} x_2 \exp\left(\frac{-2\alpha x_1^2}{w^2}\right)\exp\left(\frac{-2\alpha x_2^2}{w^2}\right) dx_1 dx_2 \tag{G.18}$$

$$= G_0 \int_{-\infty}^{a} x_2 \exp\left(\frac{-2\alpha x_2^2}{w^2}\right) dx_2 \int_{-\infty}^{\infty} \exp\left(\frac{-2\alpha x_1^2}{w^2}\right) dx_1 \tag{G.19}$$

$$= G_0 \frac{w}{2}\sqrt{\frac{\pi}{2\alpha}} \int_{-\infty}^{a} x_2 \exp\left(\frac{-2\alpha x_2^2}{w^2}\right) dx_2 \left(\frac{2}{\sqrt{\pi}}\int_{-\infty}^{\infty} e^{-u^2} du\right) \tag{G.20}$$

$$= \frac{G_o w\sqrt{\pi}}{\sqrt{2\alpha}} \int_{-\infty}^{a} x_2 \exp\left(\frac{-2\alpha x_2^2}{w^2}\right) dx_2 \tag{G.21}$$

Using the following change of variable:

$$v = -2\alpha\frac{x_2^2}{w^2} \qquad dx_2 = iw\frac{dv}{2\sqrt{v2\alpha}} \tag{G.22}$$

$$v(-\infty) = -\infty \qquad v(a) = -2\alpha\frac{a^2}{w^2} \tag{G.23}$$

Equation G.21 becomes:

$$= \frac{-G_o w^3\sqrt{2\pi}}{8\sqrt{\alpha^3}} \int_{-\infty}^{(-2\alpha a^2/w^2)} e^v dv \tag{G.24}$$

Carrying out the integral gives a solution:

$$\boxed{\int_{-\infty}^{a}\int_{-\infty}^{\infty} x_2 G(x_1,x_2)^{\alpha} dx_1 dx_2 = \frac{-G_o w^3\sqrt{2\pi}}{8\sqrt{\alpha^3}} e^{(-2\alpha a^2/w^2)}} \tag{G.25}$$